AN ABSTRACT OF THE THESIS OF

Dale A. Hubbard for the degree of Master of Science in Oceanography presented on March 19, 1999.

TITLE: A Paleogeochemical Investigation of Ferromanganese Oxyhydroxides from the Mendocino Ridge Using Laser Ablation Inductively-Coupled Plasma Mass Spectrometry (LA ICP-MS)

Abstract Approved: Signature redacted for privacy.
Robert W. Collier

Solid phases that form under the influence of changing environmental conditions often record such changes in their chemical composition. Quantification of these compositional variations is invaluable in reconstructing paleoenvironmental changes. Laser ablation, employed as a solid sample introduction system, offers fine spatial resolution (50 - 250 μm) for spectroscopic analysis of solid samples. When used in conjunction with an inductively coupled plasma-mass spectrometer (ICP-MS), the analysis is capable of high sensitivity, low detection limits, and low background. Here we present protocols for using infrared LA ICP-MS for the analysis of ferromanganese oxyhydroxide crusts for the purpose of elucidating records of environmental changes contained within these matrices. The dependence of data quality on proper matrix-matching of standards and normalization of instrumental response is addressed, and examples of environmental inferences from our observations are presented.

LA ICP-MS analysis was applied to a study of ferromanganese crusts. Ferromanganese oxyhydroxide phases have been the subject of a number of paleoceanographic studies because they function as recorders of surrounding seawater conditions over periods of millions of years. Changes in interelemental relationships within the layered ferromanganese oxyhydroxide matrix can help elucidate changes in environmental conditions such as the degree of oxia, relative water depth, and hydrothermal or diagenetic influence. Submersible cruises have recovered a large number of ferromanganese crusts and nodules from the Mendocino Ridge. The Mendocino Ridge has a complex geological history. This major topographic feature, extending 3000 km westward from the California coast, was once at sea level, but has been subsiding for the past 5.5 to 8 million years. This work presents background information about the Mendocino Ridge, reviews paleoceanographic literature related to manganese nodules and crusts, presents hypotheses about geochemical records present in Mendocino Ridge manganese nodules and crusts, examines a number of geochemical proxies and their relevance to Mendocino Ridge manganese deposits, and discusses the results of these investigations.

A Paleogeochemical Investigation of Ferromanganese Oxyhydroxides from the Mendocino Ridge using Laser Ablation Inductively-Coupled Plasma Mass Spectrometry (LA ICP-MS)

by

Dale A. Hubbard

A THESIS

Submitted to

Oregon State University

In partial fulfillment of the

Requirements for the degree of

Master of Science

Completed March 19, 1999

Commencement June 2000

Master of Science thesis of Dale A. Hubbard presented on March 19, 1999.

APPROVED:

Signature redacted for privacy.

Major Professor, representing Oceanography

Signature redacted for privacy.

Dean of the College of Oceanographic and Atmospheric Sciences

Signature redacted for privacy.

Dean of Graduate School

I understand that my thesis will become part of the permanent collection of Oregon State University libraries. My signature below authorizes release of my thesis to any reader upon request.

Signature redacted for privacy.

Dale A. Hubbard, Author

ACKNOWLEDGEMENTS

First, I wish to thank Bob Collier for his guidance, support (financial and intellectual), and friendship during my graduate career. The many extracurricular opportunities that he offered, including Crater Lake work and a memorable Southern East Pacific Rise cruise, were highlights of my graduate school experience.

Marta Torres also offered her support, co-authored the second chapter of this work, provided interesting work that kept me funded, and provided generous guidance. Chih-An Huh was an enormous help with this project—he performed ^{230}Th excess dating on all of my samples and offered many suggestions and much advice related to other aspects of my project.

Chi Meredith and Bobbi Conard deserve kudos for their mastery of all aspects of lab work, and for always being willing to help me with developing a wide variety of methods and acquiring lab supplies and materials. Andy Ungerer runs a tight ship—his advice, assistance, and broad knowledge of all things analytical was an enormous boon in almost every facet of my work.

Roger Nielsen provided guidance with EPMA analyses and SEM photography.

Martin Fisk provided me with Mendocino Ridge manganese nodule and crust samples, and contributed greatly to my understanding of the Mendocino Fracture Zone.

Pankaj Sharma, of Purdue University, performed AMS analysis of ^{10}Be and ^{26}Al on my samples, and offered much advice on their preparation.

Chris Guay and Daniel Oros, two fellow chemical oceanography graduate students, provided friendship, advice, and often very lofty philosophical conversation during lunch (and happy) hour.

I appreciate the support & love that my family has provided through this and all other parts of my life. I treasure their positive influence, their interest, and their desire to share in my life experiences.

Last, but certainly not least, I wish to thank all of my surf buds, biking cohorts, climbing partners (especially Nathalie Williams, my favorite partner of all), fellow snow-play enthusiasts, and the geological and climatic forces that sculpted the Pacific Northwest for helping me stay in touch with what is truly important in life—never-ending amazement at the natural world around us.

CONTRIBUTION OF AUTHORS

Chapter II of this work benefited greatly from the contribution of Dr. Marta Torres, who authored the material related to clam analyses and offered many ideas pertaining to the rest of the text. Dr. Chih-An Huh contributed text in chapter III pertaining to ^{230}Th excess dating and provided invaluable guidance interpreting dating data.

TABLE OF CONTENTS

TABLE OF CONTENTS (CONTINUED)

TABLE OF CONTENTS (CONTINUED)

LIST OF FIGURES

LIST OF FIGURES (CONTINUED)

LIST OF FIGURES (CONTINUED)

LIST OF TABLES

LIST OF APPENDICES

Solution chemistry

- AES
  - 980211 MRF6-12R plotfile
  - MRF2-3R AES
  - MRF6-12R AES
- ICP-MS
  - MRF2-3R Be and Ce
  - MRF6-12R Be and Ce

LIST OF APPENDIX TABLES

A Paleogeochemical Investigation of Ferromanganese Oxyhydroxides from the Mendocino Ridge using Laser Ablation Inductively-Coupled Plasma Mass Spectrometry (LA ICP-MS)

I. INTRODUCTION

The advent of the laser as a sampling device for analytical chemistry has allowed the potential for studying geochemical records preserved in solid samples on very fine spatial scales. Analyses that were formerly only possible to accomplish with hours of tedious hand sampling, such as scraping successive layers off of manganese nodules for dissolution and analysis, can be performed *in situ* using laser ablation. This eliminates the need to convert the sample from its solid state before analysis, reducing the amount of time required and the potential for contamination. When employed in conjunction with an inductively-coupled plasma mass spectrometer (ICP-MS), an instrument known for its ability to perform rapid determinations of large numbers of elements simultaneously, laser ablation becomes a very powerful tool for the geochemist.

The chemical record enclosed within the layers of manganese nodules and crusts is particularly well suited for LA ICP-MS analysis. Manganese nodules and crusts have long been regarded as "paleorecorders" of ambient seawater conditions (Hein, 1992; de Carlo, 1991) because they form by precipitation of metals directly from seawater, from hydrothermal vent effluents, and from diagenetic fluxes. Nodules and crusts offer a promising means of examining the relative influences of these metal sources in an area

over a period of time on the order of millions of years. The ability to sample these phases with a spatial resolution on the order of tens of microns enables the geochemist to piece together a detailed portrait of the history of the water mass in which a nodule or crust formed.

The Mendocino Ridge, a major topographic feature extending 3000 km westward from California into the Pacific Ocean, has had a complex geological history. The Mendocino Ridge was once at sea level, and has been subsiding for the past 5.5 to 8 million years (Fisk et al., 1992). A large number of ferromanganese nodules and crusts have been recovered from the Mendocino ridge. Characterized by slow growth rates on the order of millimeters per million years, nodules and crusts from the Mendocino ridge must have been progressively accumulating during the course of its subsidence, and are likely to contain a chemical record of the different water column characteristics which they have passed through.

Seawater's chemical characteristics change appreciably with depth. Changes in the amount of dissolved oxygen mediate changes in the availability of dissolved metals that precipitate onto growing manganese nodules and crusts. This may result in changes in composition and growth rate in nodules or crusts which have undergone changes in depth.

Rare earth element (REE) concentrations are known to vary systematically with depth in the water column (de Baar et al, 1985; Elderfield, 1988; Piepgras and Jacobsen,

1992). Since REEs are concentrated in manganese oxyhydroxides compared to seawater (De Carlo, 1991), a record likely exists of the relative concentrations (i.e. ratios) of REEs in the water column which a Mendocino ferromanganese deposit has passed through during the subsidence of the ridge. Additionally, Ce, a redox-sensitive REE, may provide a record of the redox conditions of the water column which Mendocino ferromanganese deposits have encountered. REEs distributions may hold a record of the subsidence history of these manganese oxides.

Since the Mendocino Fracture Zone is a tectonically active region (although it is not presently hydrothermally active) and is adjacent to the Gorda Ridge, an area of intense hydrothermal activity, it stands to reason that there should be a record of episodes of hydrothermal influence in ferromanganese oxyhydroxides recovered from the Mendocino Ridge. Characteristics such as the ratios of major elements, growth rate, and presence of trace elements which are concentrated in vent fluids all are promising hydrothermal proxies.

This work contains two chapters, one providing a detailed description of LA ICP-MS methods for two marine geochemical phases (ferromanganese oxyhydroxides and carbonates) and instructions for LA ICP-MS experimental design and proper data processing, the other focused on examining the geochemical record contained in a suite of manganese nodules and crusts from the Mendocino Ridge.

II. LASER ABLATION ICP-MS ANALYSIS OF MARINE GEOCHEMICAL PHASES: A POWERFUL TOOL FOR UNRAVELLING ENVIRONMENTAL CHANGES

A manuscript by Dale Hubbard and Marta Torres to be submitted to the Journal of Analytical Atomic Spectroscopy.

ABSTRACT

Solid phases which form under the influence of changing environmental conditions often record such changes in their chemical composition. Quantification of these compositional variations is invaluable in reconstructing paleoenvironmental changes. Laser ablation employed as a solid sample introduction system offers fine spatial resolution (50 - 250 μm), and in conjunction with an inductively coupled plasma-mass spectrometer's (ICP-MS) high sensitivity, low detection limits, and low background, provides a means of resolving fine scale changes in solid samples. Here we present protocols for using infrared LA ICP-MS for the analysis of ferromanganese oxyhydroxide crusts and carbonates (bivalve shells) for the purpose of elucidating records of environmental changes contained within these matrices. The dependence of data quality on proper matrix-matching of standards and normalization of instrumental response is addressed, and examples of environmental inferences from our observations are presented. The approach presented here is directly applicable to newer UV laser systems as well, as the analytical problems described herein primarily concern the ICP-MS system.

1. Introduction

The environmental conditions in which solid phases form are reflected in some predictable way in their chemical composition. There is a large body of literature with examples of how paleoenvironmental systems have been reconstructed on the basis of geochemical records preserved in solid phases (e.g. Hein et al., 1992; Christensen et al., 1997; Hart and Blusztajn, 1998), including authigenic precipitates and biological remains such as coral, shells, teeth, and trees. These investigations would invariably benefit from an analytical tool which can provide resolution at intervals of tens of microns. Laser ablation employed as a technique to introduce solid samples into an inductively coupled plasma-mass spectrometer (ICP-MS) can provide an attractive method for the geochemical analysis of minerals and skeletal materials which are formed progressively in changing environmental settings.

Inductively coupled plasma-mass spectrometry is widely applied for the analysis of geochemical samples because of its many advantages over traditional atomic analytical techniques. ICP-MS is characterized by relatively simple spectra, high sensitivity, low background and very low detection limits (see Falkner et al., 1995 for review). Laser ablation, in association with ICP-MS, has been developed to take advantage of the great potential of the ICP-MS instrumentation applied directly to solid samples. A beam of laser radiation is focused upon the surface of a solid, its absorption causes heating, melting, vaporization, physical excavation, and excitation in a phenomenon collectively referred to as ablation. When ablation products are introduced into a secondary ion source such as an argon plasma, all ablated material becomes ionized, and mass spectrometric analysis is made possible. First demonstrated in 1985 by Gray, laser ablation inductively coupled plasma mass spectrometry (LA ICP-MS) evolved from the use of lasers as sampling devices for other less sensitive analytical techniques including atomic absorbance, emission, and fluorescence methods. Thorough reviews of the rise of the laser as a sampling tool, detailed descriptions of types of lasers used, sampling processes,

standardization techniques and capabilities of the method have been compiled by Moenke-Blankenburg (1989) and Denoyer et al. (1991). Application of LA-ICP-MS to geological samples was evaluated by Williams and Jarvis (1993), Jarvis and Williams (1993) and Perkins et al. (1991). Lasers can typically ablate craters on the order of tens to hundreds of μm in diameter, which is generally significantly finer than the resolution afforded by common manual sampling methods. The ability to directly analyze solids provides several advantages over dissolution methods, including: 1) increased spatial resolution, 2) minimal contamination during sampling (by reducing sample handling and eliminating the need for dissolution) and 3) reduction of isobaric interferences by eliminating the presence of molecular ions. These polyatomic ions form in the plasma by reactions of the carrier gas (Ar) with oxides, chlorides, and/or nitrites present in the aqueous medium carrying the dissolved sample. For example, Ba -oxide complexes create major molecular interferences for REE determinations when using solution ICP-MS methods (Garbe-Schonberg and McMurtry ,1994), which are greatly reduced or eliminated in the anhydrous laser environment.

Here we describe analyses of ferromanganese deposits and bivalve shells which we believe contain records of their environment of formation. The ferromanganese nodules and crusts include specimens recovered from the Mendocino Ridge off of the central California coast, an area with complex geological history (Duncan et al., 1994; Fisk et al., 1993). The clam samples were recovered live from cold seeps in the Monterey Bay Canyon (Barry et al., 1997). The potential that ferromanganese nodules and crusts, as well as bivalve shells hold records of local environmental conditions has been widely discussed (Christensen et al., 1997; Hein et al., 1992; Garbe-Schonberg and McMurtry, 1994; Carriker et al., 1982; Stecher et al., 1986). A limited number of investigators have used LA ICP-MS for the analysis of carbonate phases (e.g. Feng 1994; Stecher et al., 1996; Hart and Blusztajn, 1998) and ferromanganese nodules and crusts (e.g. Christensen et al., 1997; Garbe-Schonberg and McMurtry, 1994). Here, we present a large data set

evaluating the benefits and difficulties of using LA ICP-MS on ferromanganese crusts and carbonates to unravel their paleo-geochemical record. While there are examples in recent literature dedicated to analyses employing newer UV and excimer laser systems (Christensen et al., 1997 and Davies et al., 1998), the concept presented here of normalization to matrix-matched standards is important in overcoming limitations inherent in the ICP-MS system, and therefore applies to a broad range of LA ICP-MS analyses.

2. Analytical methods

The system employed for this study was a Fisons VG PlasmaQuad PQ 2+ Inductively Coupled Plasma Mass Spectrometer (ICP-MS) coupled with a 500 mJ Spectron Laser Systems Nd:YAG laser, operating in the infrared (1064 nm). Operating conditions are presented in table II.1. Samples are housed within a quartz ablation cell, and Ar is employed as a carrier gas. Instrumental stability, tuning, and mass calibration were checked initially using a solution nebulization setup. After switching the sample-introduction system to the laser module, tuning was performed on NIST Standard Reference Material (SRM) 612, a fused glass standard. All analyses were performed in pulse counting mode, which offers highest sensitivity and a wide dynamic range (Gray, 1985). Typical counts at mass 139 (La), the mass used for optimizing sensitivity, range from 3 X 10^5 to 1 X 10^6 counts sec^{-1} (cps) in low magnification and from 1 X 10^5 to 3 X 10^5 cps in high magnification. Replicate analyses were performed on SRM 612 in both high and low magnification modes to determine instrumental stability. Analyses performed for 12 elements ranging in mass from 11 to 238 amu typically yield an instrumental response with a standard deviation less than 7% in low magnification and 10% in high magnification.

ICP-MS operating conditions			
Instrument	VG Elemental PlasmaQuad PQ 2+		
Forward power	1500 W		
Reflected power	<5 W		
Ar flow rates	*coolant*	13 l/min	
	nebulizer	1.1 l/min	
	auxiliary	0.7 l/min	
Laser operating conditions			
Laser type	Nd:YAG, Spectron Laser Systems		
Wavelength	1064 nm		
	Matrix		
	SRM 612	**nodules and crusts**	**carbonates**
Laser mode	Q-switched	Q-switched	Q-switched
Laser energy	540 V	540 V	540 V
Repetition rate (Hz)	10	4	4
holes per site	1	6	1

Table II.1 ICP-MS and laser operating conditions.

2.1 *Calibration*

The major limitation in quantitative analysis using LA ICP-MS is calibration. The net instrumental response is affected by variables at each stage of analysis. These include: 1) the ablation process, 2) transport of material to the plasma, 3) efficiency of ionization and sample introduction to the vacuum system, and 4) mass response of the quadrupole and detectors. By far, the biggest variable in this chain of events is the quantification of the sample yield at the ablation step (Redmond et al., 1990; Darke and Tyson, 1993). Although the exact mechanism by which material is remobilized from a solid is complex and poorly known, it is clear that the ablation process is particularly sensitive to sample matrix. The chemistry and mineralogy of the individual samples have been shown to influence the ablation behavior (Jarvis and Williams, 1993) --similar elemental responses have been obtained from samples with similar mineralogical composition.

An approach that can be used to quantify the laser yield is to measure a naturally occurring major element in the samples of interest by conventional analytical techniques. This particular element can then be used as an internal standard to generate high-resolution profiles of minor and trace elements across a given sample which does not show large mineralogical variations. In practice, this technique is restricted to matrices in which a major element with a low natural-abundance isotope is present in constant levels--the choice of a higher-abundance isotope may overwhelm the detector. In the case of carbonate samples, the variation of the signal intensity can be normalized using ^{43}Ca (natural abundance = 0.135%) as internal standard, assuming that the calcium carbonate content is constant throughout the sample (Imai, 1992). Feng (1994) successfully conducted quantitative analyses of Sr, Y, Ba, and REE in bulk calcite and dolomite powders using the NIST 612 silicate glass as a non-matrix matched calibration standard, and ^{43}Ca as the internal standard.

In contrast, manganese is a monoisotopic element, and thus cannot be used as a monitor when running ferromanganese crust samples because it is present in such high

concentrations that it overwhelms the ICP-MS detector. Fe, the other major elemental constituent of ferromanganese crusts, has several isotopes, which allows the selection of a low abundance isotope (e.g. ^{57}Fe, abundance = 2.25%) for analysis. The heterogeneous nature of ferromanganese oxide phases precludes the selection of any other element as an internal standard--no element with an appropriately low natural abundance isotope is present in constant enough concentration to serve as internal standard.

Fully quantitative analysis of elemental concentrations also requires normalization for variations in the mass response of the quadrupole and detectors. Since the mass response might vary across the mass range, the utilization of a single internal standard does not completely compensate for these changes. Another source of uncertainty derives from variations in the efficiency of ablation for individual elements as a function of the chemistry of the element (e.g. its volatility) and the chemistry of the bulk sample. In an effort to monitor spectral response changes during analyses and to compensate for the inability to use a strict internal standard in these samples, we have prepared pressed-powder pellets of ferromanganese and carbonate materials, following the methods of Perkins et al. (1991) and Jarvis and Williams (1993). The pellet monitor is analyzed frequently during the course of a run, and variations in instrument response with respect to the monitor are applied to sample concentration calculations. For ferromanganese nodule and crust analyses we used USGS manganese nodule standard Nod A-1 (composition given in table II.2); for carbonate samples we obtained reference material by milling a *Calyptogena* shell from Galapagos hydrothermal fields (Gal-1; table II.2) with a 0.5 mm dental burr and homogenizing the sample in an agate mortar. In both cases, pellets were made by mixing 100 µl 1% w/v polyvinyl alcohol solution with 1 g of reference material, homogenizing thoroughly with a spatula, and applying 3 tons pressure for one minute using a hydraulic press. Pressed pellets were dried in an oven at 60° C and stored in a dessicator. Standard pellets were imbedded into epoxy along with the samples or affixed adjacent to the sample inside the quartz ablation cell. Data acquisition on the standard pellets was interspaced with

Table II.2.A. Average counts, relative standard deviation, and detection limits for LA ICP-MS standards in low magnification mode.

	phase	conc.* (ppm)	isotope analyzed	average counts** (cps)	relative std. dev.*** (%)	limit of detection**** (ppm)
Li	612	*3.99E+01*	7	1.50E+05	11	
	Gal-1			2.04E+02	14	
Mg	612	*1.20E+02*	26	1.37E+05	10	
	Gal-1			1.76E+04	16	
Ca	612	*8.15E+04*	43	2.19E+06	8	
	Gal-1	4.00E+05		1.46E+06	12	1.0E+03
	Nod A-1	1.10E+01	46	6.62E+04	22	2.4E-10
Mn	612	*3.96E+01*	55	6.26E+05	13	
	Gal-1	5.54E-00		1.06E+04	11	2.8E-01
Co	612	*3.55E+01*	59	9.79E+05	6	8.9E-03
	Nod A-1	3.11E+03		1.52E+06	19	1.0E-01
Cu	612	*3.77E+01*	65	6.57E+04	7	
	Gal-1	5.14E-00		5.72E+04	12	2.0E-00
Sr	612	7.84E+01	86	1.49E+05	8	
	Gal-1	1.27E+03		3.11E+05	7	1.3E-00
Cd	612	*2.84E+01*	114	7.15E+04	8	
	Gal-1	4.60E-02		4.22E+01	18	2.6E-02
Ba	612	*3.89E+01*	138	7.27E+05	8	
	Gal-1	9.18E-00		2.35E+04	7	1.8E-02
La	612	*3.57E+01*	139	9.63E+04	7	5.4E-03
	Nod A-1	1.23E+02		2.69E+05	12	1.2E-02
	Gal-1	6.53E-02		1.98E+02	18	7.5E-03
Ce	612	*3.79E+01*	140	1.06E+06	6	3.1E-03
	Nod A-1	7.22E+02		3.10E+06	14	4.6E-03
Pr	612	*3.74E+01*	141	3.44E+04	5	1.4E-03
	Nod A-1	2.24E+01		9.82E+04	10	4.2E-03
Nd	612	*3.46E+01*	146	2.32E+04	5	9.4E-03
	Nod A-1	9.46E+01		7.11E+04	11	5.7E-04
Sm	612	*3.68E+01*	147		6	2.0E-02
	Nod A-1	2.18E+01		1.25E+04	11	6.1E-04
Eu	612	*3.44E+01*	151	4.26E+03	5	4.0E-03
	Nod A-1	5.30E-00	151	1.25E+04	11	1.9E-03
Gd	612	*3.54E+01*	157		5	1.4E-02
	Nod A-1	2.66E+01	157	1.25E+04	10	1.5E-03
Tb	612	*3.69E+01*	159		4	1.9E-03
	Nod A-1	4.00E-00	159	1.51E+04	10	5.0E-03
Dy	612	**3.50E+01**	162		5	2.6E-03
	Nod A-1	2.34E+01	162	2.48E+04	11	7.8E-04
Ho	612	*3.73E+01*	165		7	1.5E-03
	Nod A-1	5.03E-00	165	1.92E+04	12	3.5E-03

Table II.2.A continued. Average counts, relative standard deviation, and detection limits for LA ICP-MS standards in low magnification mode.

	phase	conc.* (ppm)	isotope analyzed	average counts** (cps)	relative std. dev.*** (%)	limit of detection**** (ppm)
Er	612	*3.79E+01*	166		7	6.2E-03
	Nod A-1	1.50E+01	166	1.96E+04	12	2.4E-03
Tm	612	*3.73E+01*	169		5	1.2E-03
	Nod A-1	2.19E-00	169	9.37E+03	12	5.6E-03
Yb	612	*3.81E+01*	174	6.92E+03	6	7.2E-03
	Nod A-1	1.43E+01	174	2.07E+04	11	1.6E-03
Lu	612	*3.72E+01*	175	3.23E+03	5	2.2E-03
	Nod A-1	2.10E-00	175	9.73E+03	13	5.7E-03
Pb	612	3.86E+01	206		7	1.4E-02
	612	3.86E+01	208	4.10E+05	8	
	Gal-1	8.27E-02		4.16E+02	27	7.3E-03
Th	612	3.78E+01	232	3.84E+04	5	1.7E-03
	Nod A-1	2.70E+01		9.57E+04	16	5.2E-03
U	612	3.74E+01	238	6.62E+05	9	3.7E-03
	Nod A-1	6.00E-00		5.62E+04	12	1.9E-03
	Gal-1	9.79E-02		2.38E+02	15	8.3E-03

* 612 concentration data from NIST certified values, except italicized values from Federowitch, and bold values from Feng, 1994. Nod A-1 values from Flanagan and Gottfried, 1980, except REE values from Bau et al., 1996.

** blank-corrected values.

*** % deviation calculated on repeated analyses of standard within a run. For 612 n=10, for Nod A-1 n=153, and for GAL-1 n=22.

**** missing values indicate blank was not measured—element used for tuning ICP-MS with SRM 612 or GAL-1 only.

Table II.2.B. Average counts, relative standard deviation, and detection limits for LA ICP-MS standards in high magnification mode.

	phase	conc.* (ppm)	isotope analyzed	abundance	average counts** cps	rel. std. dev.*** (%)	limit of detection**** (ppm)
B	612	3.20E+01	11	0.801	3.82E+02	24	
P	Nod A-1	6.00E+03	31	1.000	1.51E+04	52	3.0E+02
Ti	Nod A-1	3.20E+03	48	0.735	1.41E+05	29	1.3E-00
V	Nod A-1	7.70E+02	51	0.998	4.60E+04	31	1.0E-00
Fe	Nod A-1	1.09E+05	57	0.023	2.33E+05	35	2.3E+02
Co	612	*3.55E+01*	59	1.000	5.35E+03	6.2	
	Nod A-1	3.11E+03		1.000	2.40E+05	31	1.0E-00
Ni	Nod A-1	6.36E+03	60	0.262	9.37E+04	32	2.0E+01
Cu	Nod A-1	1.10E+03	63	0.691	3.98E+04	35	1.1E+01
	Nod A-1	1.10E+03	65	0.308	1.94E+04	35	6.9E-00
Zn	Nod A-1	5.87E+02	64	0.486	2.16E+04	33	1.9E-00
	Nod A-1	5.87E+02	66	0.278	1.12E+04	33	3.0E-00
Sr	612	7.84E+01	88	0.826	2.50E+04	6.5	
Mo	Nod A-1	4.48E+02	95	0.148	1.22E+04	31	1.5E-00
Ag	612	2.20E+01	107	0.518	2.64E+03	6	
La	612	*3.57E+01*	139	0.999	2.07E+04	7	
	Nod A-1	1.33E+02		0.999	2.54E+04	34	1.4E-01
Ce	Nod A-1	6.68E+02	140	0.885	2.79E+05	33	6.0E-02
Pr	Nod A-1	2.34E+01	141	1.000	8.03E+03	35	7.3E-02
Nd	Nod A-1	9.53E+01	144	0.238	7.42E+03	34	2.8E-01
Sm	612	*3.68E+01*	147	0.150	4.57E+03	8	
Eu	612	*3.44E+01*	151	0.478	1.58E+04	9	
Lu	Nod A-1	2.22E-00	175	0.974	7.30E+02	37	1.5E-01
Au	612	5.00E-00	197	0.524	1.29E+03	17	
Pb	Nod A-1	8.46E+02	206	0.252	1.34E+05	32	2.9E-01
	Nod A-1	8.46E+02	208	0.524	2.75E+05	32	1.4E-01
Th	612	3.78E+01	232	1.000	2.65E+04	8	
	Nod A-1	2.70E+01		1.000	6.32E+03	37	1.1E-01
U	612	3.74E+01	238	0.993	3.27E+04	4	
	Nod A-1	6.00E-00		0.993	3.15E+03	35	4.4E-02

* 612 concentration data from NIST certified values, except italicized values from Federowitch. Nod A-1 values from Flanagan and Gottfried, 1980, except REE values from Bau et al., 1996.

** blank-corrected values.

Table II.2.B continued. Average counts, relative standard deviation, and detection limits for LA ICP-MS standards in high magnification mode.

*** % deviation calculated on repeated analyses of standard within a run. For 612 n=9, for Nod A-1 n=53.

**** missing values indicate blank was not measured—element used for tuning ICP-MS with SRM 612 only.

sample acquisition to allow for verification of the mass response curve during the analysis run.

To evaluate the analytical accuracy of this approach, two comparison studies were undertaken. First, USGS manganese nodule standard Nod A-1 was used as a monitor in a short LA ICP-MS run to calculate concentrations in a second pressed powder pellet of USGS manganese nodule standard Nod P-1. Second, samples were obtained by milling sequential increments of manganese crusts and clam shells using a 0.5 mm dental burr under a flow-through clean hood. Material was scraped from areas which were previously analyzed by laser, weighed, and brought into solution. The ferromanganese crusts were digested using concentrated HF/HNO_3, and the dissolved material was analyzed using ICP-AES (and ICP-MS for Ce). The carbonate samples were dissolved using 0.45 N HNO_3. The dissolved material was then analyzed by ICP-MS.

2.2 *Sample preparation and analysis*

Ferromanganese nodules and crust samples for analyses by laser-ablation ICP-MS were prepared in the same manner as for electron microprobe analysis--crusts were cut in cross section, immersed in epoxy, potted in a plug mold, vacuum impregnated, and subsequently polished on a lapping wheel to present a smooth ablation surface and to reveal internal structure such as growth bands. Analyses of ferromanganese nodules and crusts were performed using both high (~20 μm spot size) and low magnification (~100 μm spot size) modes. Larger spot size results in a larger mass of ablated material, allowing analysis of trace constituents such as rare earth elements (REEs). Smaller spot sizes ablate sufficient material for analysis of transition elements, which are present in concentrations on the order of several hundred ppm, as well as for trace elements for which the mass spectrometer shows elevated sensitivity. Both high and low magnification sample data were acquired along transects perpendicular to the surface, along the axis of growth. Low

magnification transects were comprised of single craters at 350 μm intervals. High magnification transects were comprised of a rastered line, 6 craters (approximately 450 μm) wide, spaced every 50 μm along the axis of growth (Figure II.1).

Cross sections (10 mm thick) of the bivalve shells were cut near the axis of maximum growth using a water-cooled band saw equipped with a diamond-impregnated copper blade. To clearly identify the shell structure, the shell cross section was polished with silicon carbide sand paper. The polished samples were sectioned into pieces smaller than 20 mm in length to fit into the ablation chamber, and washed with deionized water, as described by Stecher et al. (1996). Bivalve shells were analyzed exclusively in low magnification, with samples collected by ablating the shell along the axis of maximum growth at 350 μm intervals. Parallel transects were obtained for the outer (non-prismatic) layer and middle (prismatic) layer of the shell (Figure II.2).

Laser parameters for high and low magnification acquisitions are given in table II.1. Argon blanks for both high and low magnification analyses were acquired by firing the laser with the shutter closed at the beginning and end of each run, which consisted of up to 50 sample acquisitions along a transect, and intermittently during longer runs. These blank values are interpolated over the course of the run and later subtracted from data acquired on standards and samples. The mass response curve was monitored by replicate analyses of the pressed standard pellets (Nod A-1, and Gal-1) every 10 sample spots. Typical counts for Nod A-1 and Gal-1 are given in table II.2.

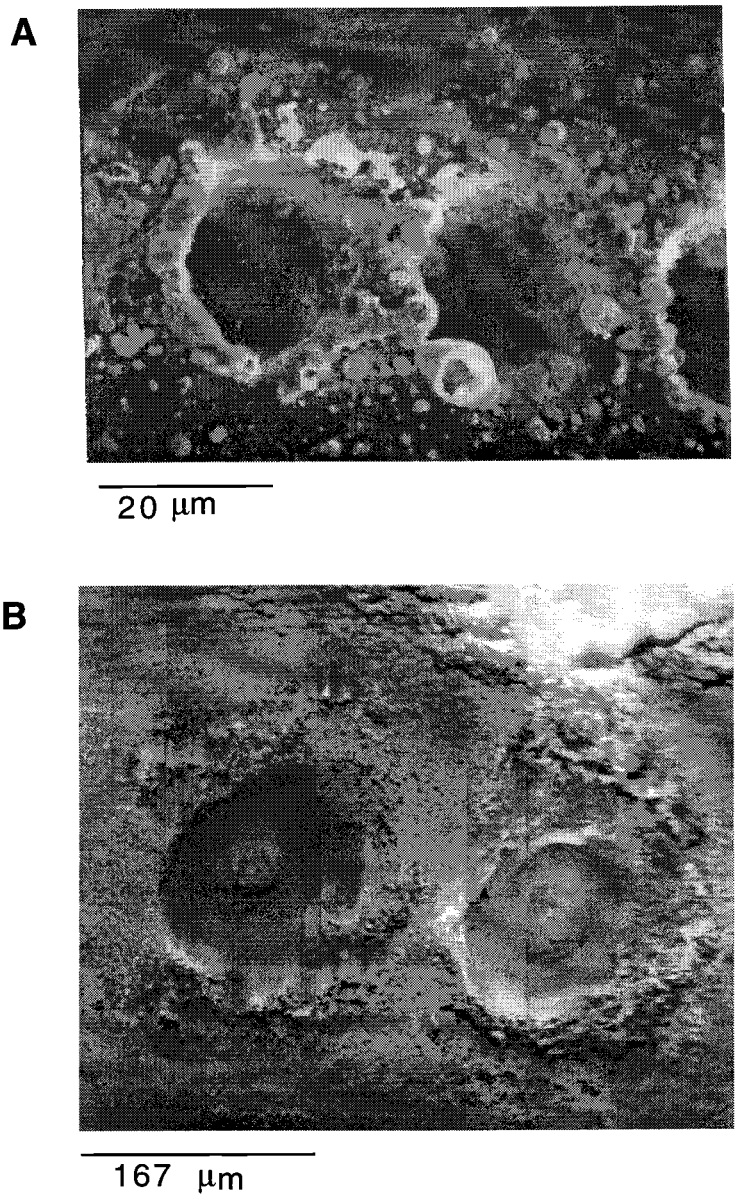

Figure II.1. SEM pictures of holes ablated by laser. A) Ablation of manganese nodule crust at high magnification. B) Ablation of a carbonate shell at low magnification.

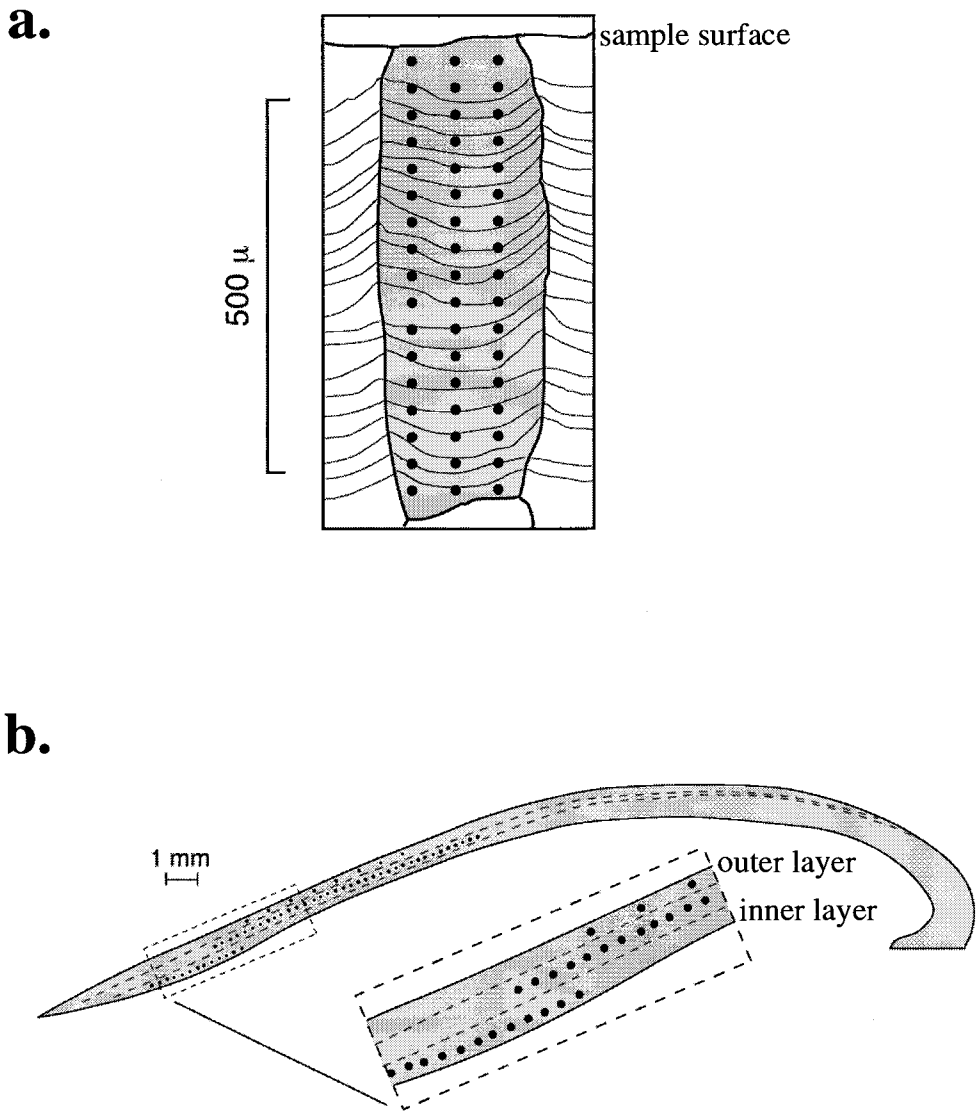

Figure II.2. Schematic representation of LA-ICPMS profiles. a) Diagram of a manganese crust showing growth zonation relative to an ablation transect. b) Diagram of a carbonate shell illustrating the position of the outer, middle and inner layer and the ablation transects.

3. Analysis of reference materials

3.1 *Reproducibility and instrument stability*

Replicate analyses (n=10) of NIST 612, and pressed powder pellets nod A-1 and Gal-1 were conducted at the beginning of each experiment to determine reproducibility of the analysis. For NIST 612, the relative standard deviation of instrumental response was less than 10% for most elements in both high and low magnification modes. For Nod A-1 and Gal-1, the relative standard deviation of instrumental response was less than 20% in low magnification mode. Nod A-1 replicate analyses performed in high magnification mode yielded relative standard deviations in instrumental response ranging from 20 - 50%.

To monitor changes in instrumental response over the course of a run, we have acquired data obtained from replicate analyses of pressed pellet monitors over sample runs as long as 15 hours in duration. During such long runs, mass response variations over the mass range may not be fully compensated for by the use of a single internal standard. The internal standard is likely to exhibit different behavior during ablation than other elements of interest (since Ca has different atomization energies than those of the various analyte elements) (Hager, 1989). Figure II.3.A illustrates data obtained for acquisitions on a carbonate pressed pellet standard, data from three runs performed on different days. Mn/Ca, of similar mass, exhibit little change in relative sensitivity over the course of a run. Ba/Ca and Sr/Ca, show substantial changes in relative sensitivity over the course of any given. Moreover, the relative sensitivity of the two element pairs does not change in a coherent manner; for example, during one run Ba/Ca increases by a factor of 2 while Sr/Ca decreases by a factor of 2.

In the case of ferromanganese crusts and nodules, instrument response also varies over the course of a run, as well as from day to day. As it is not possible to choose an internal standard within the ferromanganese oxyhydroxide matrix, we have chosen to quantify the mass response by frequently analyzing the homogenous pressed pellet

Figure II.3. Variations in ICP-MS relative response over the course of analytical runs and from day to day. Lines (solid, dotted, and dashed) in each figure represent analytical runs performed on different dates. A) Low magnification LA ICP-MS analysis of carbonate pressed pellet standard GAL-1. B) Low magnification LA ICP-MS analyses of USGS standard Nod A-1. C) High magnification LA ICP-MS analyses of USGS standard Nod A-1. Note changes in relative sensitivity over the course of individual runs, different trends in sensitivity and different relative responses on different days.

Figure II.3 A.

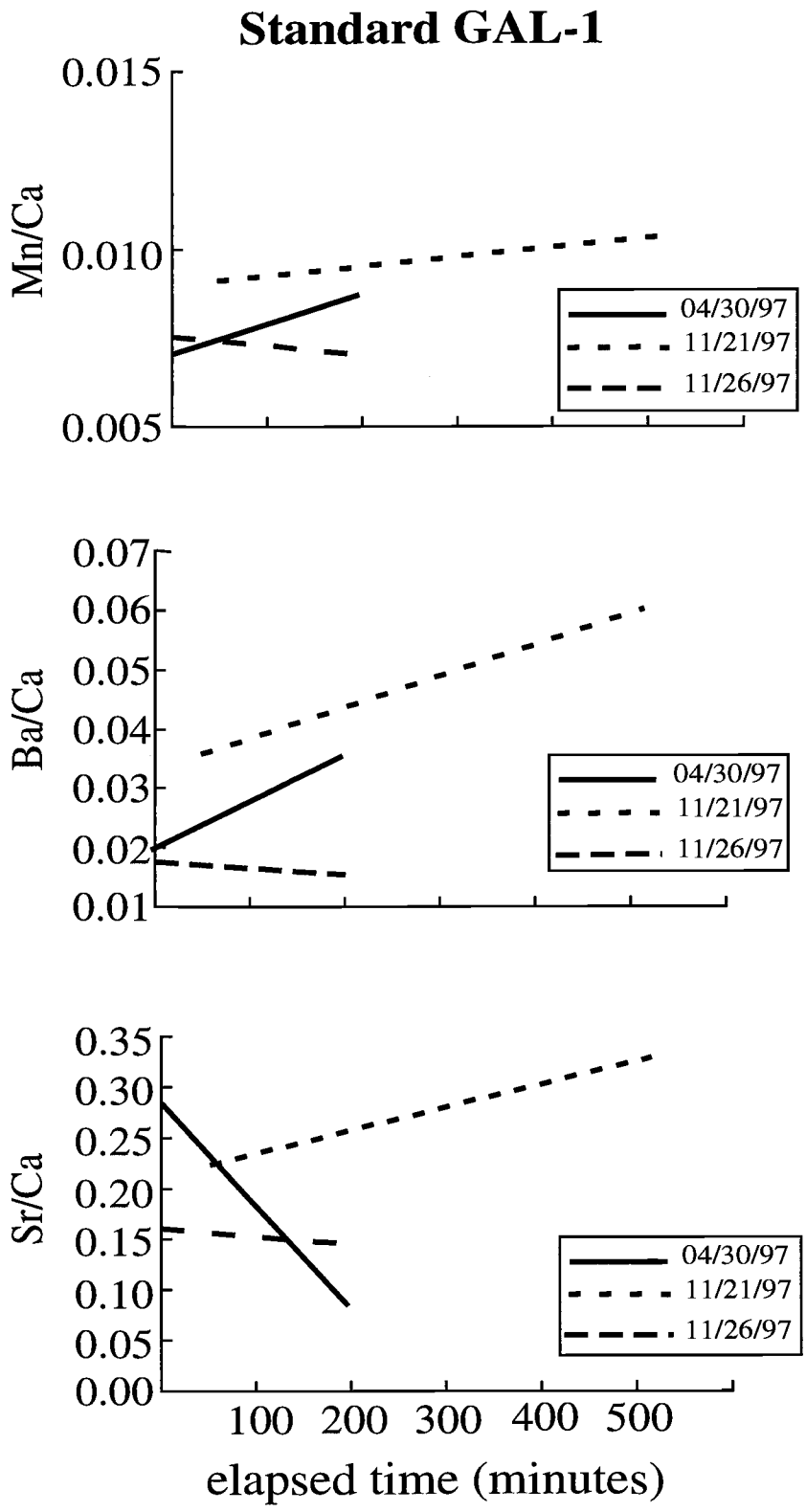
Standard GAL-1
Mn/Ca
0.015
0.010
0.005
Ba/Ca
0.07
0.06
0.05
0.04
0.03
0.02
0.01
Sr/Ca
0.35
0.30
0.25
0.20
0.15
0.10
0.05
0.00
04/30/97
11/21/97
11/26/97
100 200 300 400 500
elapsed time (minutes)

Standard Nod A-1, low magnification

Figure II.3 B.

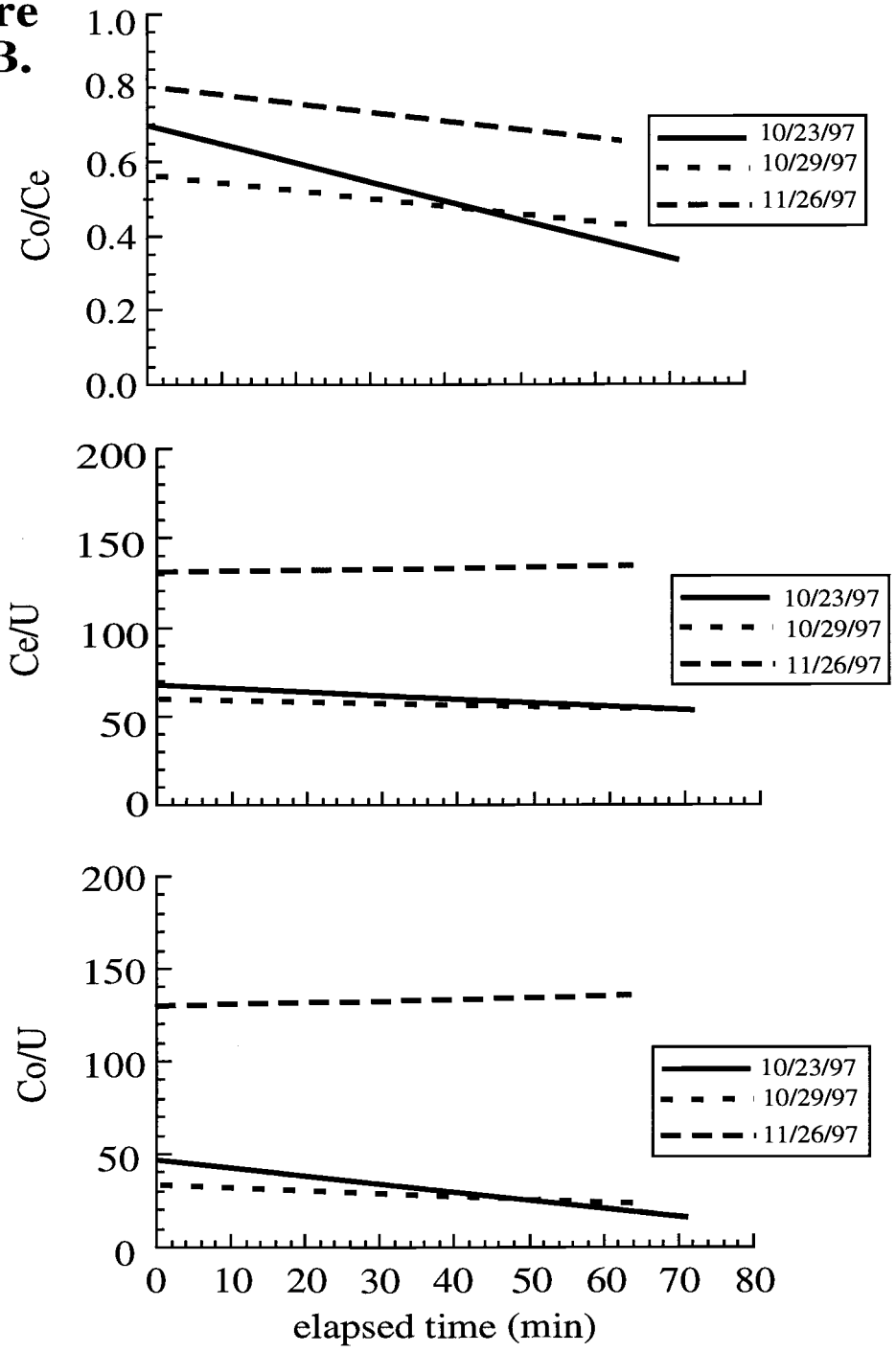

Figure II.3 c.

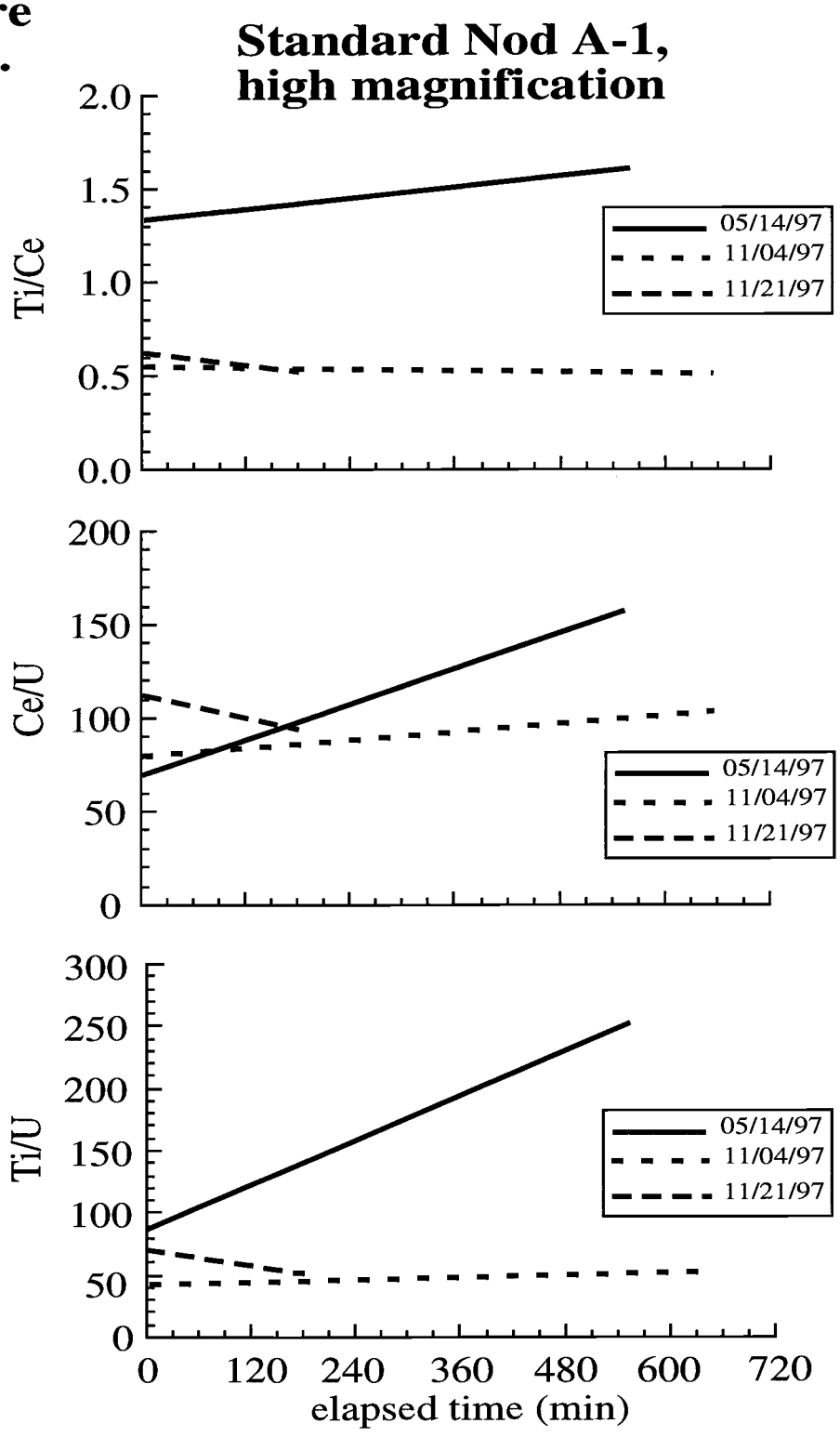
Standard Nod A-1,
high magnification
Ti/Ce
2.0
1.5
1.0
0.5
0.0
05/14/97
11/04/97
11/21/97
Ce/U
200
150
100
50
0
05/14/97
11/04/97
11/21/97
Ti/U
300
250
200
150
100
50
0
05/14/97
11/04/97
11/21/97
0
120
240
360
480
600
720
elapsed time (min)

standard. As in carbonate matrices, ferromanganese oxyhydroxide data obtained over long periods of time show mass-dependent changes in sensitivity and day-to-day variations in relative mass response. Figures 3 B and 3 C detail changes in relative sensitivity over the course of several runs in low and high magnification modes. The relative responses of low to middle masses, middle to high masses, and low to high masses can be seen to change during the course of a day's run and to vary from day to day.

For both calcium carbonate and ferromanganese oxyhydroxide matrices, changes in response over the course of a run and day-to-day variations in relative mass response underscore the need for acquiring data on a reference material interspersed with sample acquisitions, so that variations in instrument response with respect to the monitor can be applied to sample concentration calculations. This is particularly important for long analytical runs where the elements of interest span a wide mass range.

3.2 *Limit of detection*

The limit of detection for each element was calculated as three times the standard deviation of gas blank counts at each mass using the corresponding response factor. The instrumental limit of detection for this technique is a function of the mass ablated, the sensitivity of the detector for a given mass, and the integration counting time.

3.3 *Accuracy*

Comparisons were drawn between data acquired using LA ICP-MS directly on the solid carbonate pellet and data obtained using solution chemistry methods. Concentrations obtained from laser analyses of the pressed pellet were calculated as ratios to ^{43}Ca, using SRM 612 as reference. Drilled samples from the carbonate reference material were dissolved in nitric acid and analyzed by conventional ICP-MS techniques, and the data were normalized to ^{43}Ca. The results from this comparison are summarized in table II.3.

Table II.3.A. Comparison between LA ICP-MS data and analyses of drilled samples from Gal-1 clam shell.

Element	Laser conc. relative to ^{43}Ca (µmol/mol)	Drilled conc. relative to ^{43}Ca (µmol/mol)	Error (%)
Li	6.2		
Mg	288	267	8
Mn	10.43	12.6	17
Sr	1460	1440	1
Cd	0.059	0.038	55
Ba	6.54	5.83	12
La	0.052	0.044	18
U	0.036	0.028	29

Table II.3.B. Comparison between LA ICP-MS data and certified values for USGS Nod P-1 reference material.

Element	LA ICP-MS conc. (calculated ppm)	Nod P-1 certified values *	Error (%)
Co	1907	2240	-15
La	113	105	8
Ce	270	318	-15
Pr	30	28	7
Nd	128	114	12
Sm	33	27	21
Eu	8.0	7.4	7
Gd	34	34	1
Tb	5.3	4.5	18
Dy	28	26	6
Ho	5.3	4.7	12
Er	14	13	8
Tm	2.1	1.7	21
Yb	13	13	2
Lu	1.8	1.8	5
Pb	602	555	9
Th	17	18	-4
U	3.2	3.5	-8

Table II.3. Comparison between LA ICP-MS and other data: (A) clam standard GAL-1 solution ICP-MS, (B) USGS nodule standard Nod P-1 certified values

For Mg, Mn, Sr, Ba, and La the difference between the data obtained by solution chemistry and those acquired using LA ICP-MS is less than 20%. These data are comparable with the results presented by Feng (1994), for the case where large numbers of carbonate grains were analyzed to minimize inter-grain heterogeneity. Our LA ICP-MS results represent average concentration values collected over 6 analytical runs, each having 30-70 data acquisitions. The data for Cd differ by >50% (table II.3); this large difference reflects the low concentration of this element in carbonate shells, which results in large counting statistic errors.

To further constrain the accuracy of this method without the use of an internal standard, a pressed powder pellet of USGS manganese nodule standard Nod P-1 was run in low magnification mode, bracketed between analyses of a USGS Nod A-1 pellet. The response factors generated on Nod A-1 were then used to calculate concentrations of elements in Nod P-1. These concentrations are compared to certified values in table II.3. All elements except Sm and Tm were within $\pm$20% of their certified values, with most elements within $\pm$10%. Elements which are present in concentrations that are near or exceed the linear response range of the detector (e.g. Co, Ce, and Pb--all > $5X10^6$ cps) generally exhibit much poorer agreement with certified values than elements present in trace amounts do.

4. Analysis of geochemical phases

Based on the counts acquired while analyzing pressed powder pellet standards during the course of a LA ICP-MS run, instrumental response factors (cps/ppm) were calculated for ferromanganese nodules, and response factors relative to calcium were obtained for carbonate samples. For both carbonates and ferromanganese crusts, response factors were interpolated over periods when sample data were being acquired and then applied to sample data (cps or cps relative to ^{43}Ca) to calculate elemental concentrations or ratios.

To monitor data accuracy for the samples analyzed, scrapings of sample material were analyzed by solution chemistry. For clam shells, small sections of a sample which was previously analyzed by LA ICP-MS were obtained with a dental micro-drill and dissolved for chemical analyses. The results of this procedure for shell T-63 (Monterey Bay) area are illustrated in Figure II.4.

To monitor data quality for ferromanganese nodule and crust runs, two alternate approaches were employed--electron probe microanalysis (EPMA) and solution chemistry. Microprobe data were collected for major elements. LA ICP-MS and EPMA data generally show good agreement (Figure II.5 A & B). However, when one compares these data with ICP-AES and ICP-MS data generated from dissolved scrapings, there is a large difference (as great as 2X for Ce) in the calculated concentrations (Figure II.5 B & C). This may be due in part to contamination from the dental burr used for scraping (an unlikely source for Ce), to structural water in the ferromanganese oxyhydroxide matrix affecting sample weights, or to matrix effects due to dissolved solids upon the calibration curves generated for ICP-AES (although a standard addition experiment showed this effect to be negligible). In addition, Nod A-1 digests performed as experimental controls yield concentrations which agree with certified values within 5%. Ce, an element for which ICP-AES is not particularly sensitive, was further analyzed using solution ICP-MS. Data from both solution methods agree well (Figure II.5 C), discounting analytical problems with ICP-AES for Ce, yet neither method agrees well with LA ICP-MS.

Another possible explanation for the disagreement between scrapings and LA ICP-MS is that, given the highly heterogeneous nature of many ferromanganese crusts and nodules, the "broad brush" approach of scraping, which samples an area on the order of 1 cm^2 and 0.25 mm deep, is not appropriate for comparison with the ~500 _m wide rastered transect sampled by the laser. Laser (and EPMA) data therefore obviously reflect much more fine scale variability than manual scraping methods, and even taking averages of these data over intervals equivalent to scraping depths may not yield accurate comparisons.

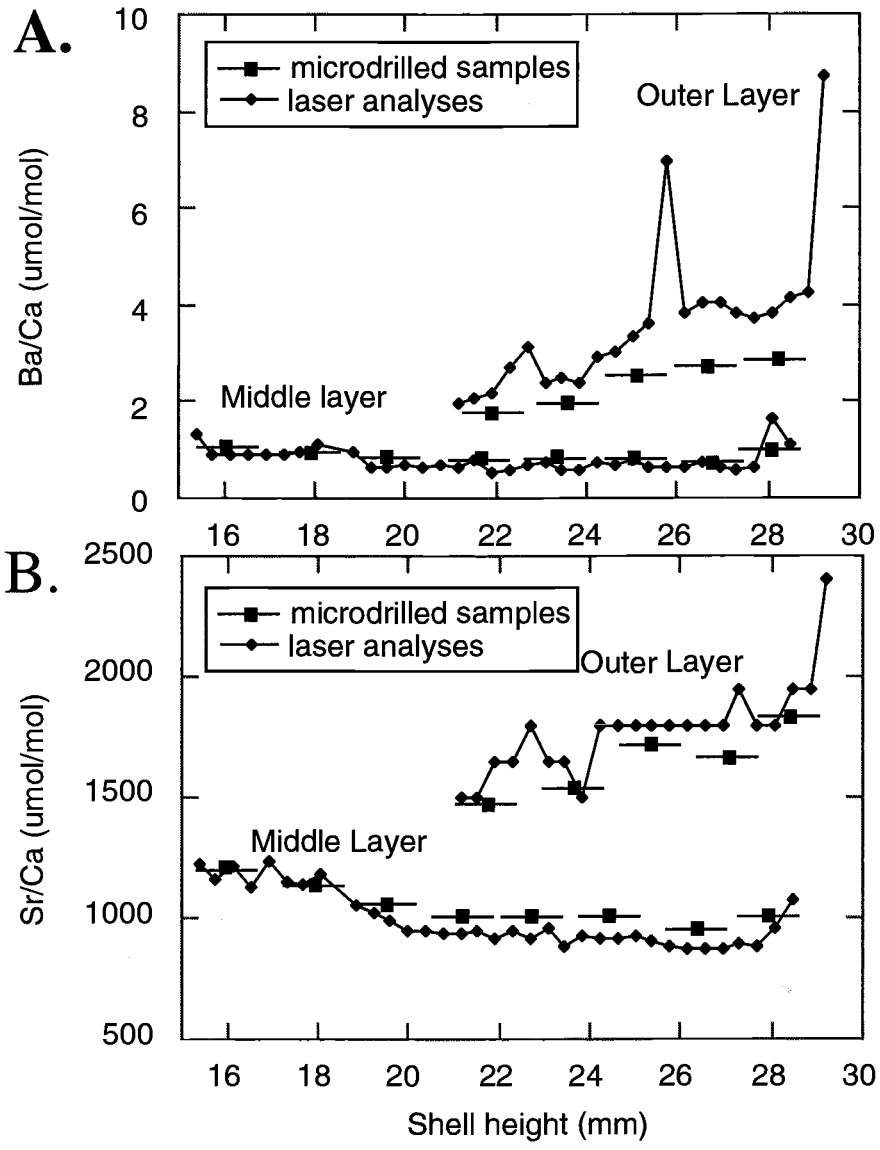

Figure II.4. Laser analyses compared to microdrilled samples. A) Comparison of Ba/Ca and B) Sr/Ca ratios versus shell height (distance from umbo to sample location) in clam shells obtained by low-magnification LA ICP-MS with ICP-MS analysis of discrete microdrilled samples (squares).

Figure II.5. Comparison of LA ICP-MS data of ferromanganese crust MRF2-3R with analyses by alternate techniques. A) High magnification LA ICP-MS analysis of Ti compared with EPMA. B) High magnification LA ICP-MS analysis of Fe compared with EPMA and ICP-AES. C) High magnification LA ICP-MS analysis of Ce compared with solution ICP-MS and ICP-AES.

Figure II. 5.

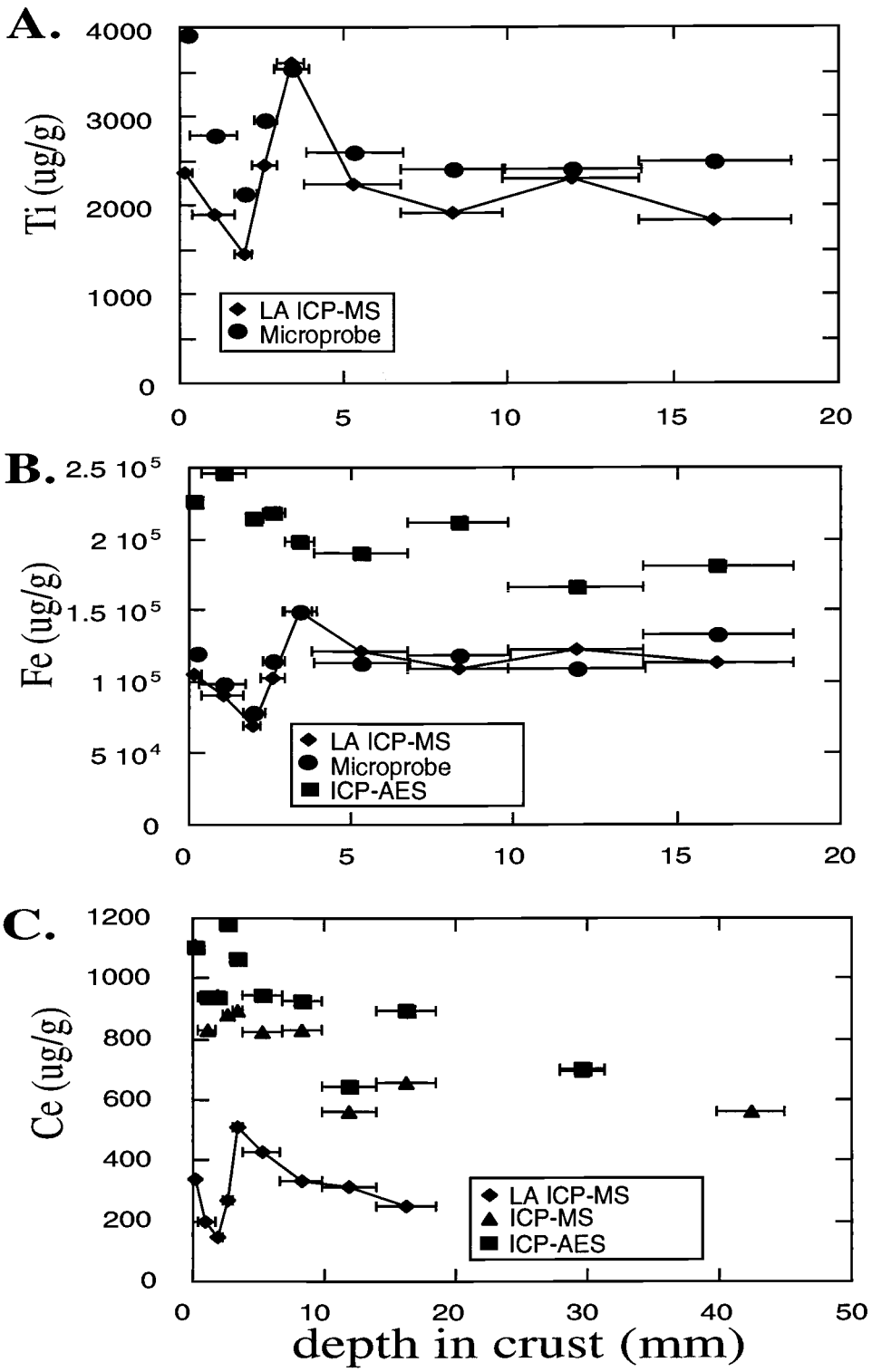
A.
Ti (ug/g)
4000
3000
2000
1000
0
LA ICP-MS
Microprobe
0
5
10
15
20
B.
Fe (ug/g)
2.5 10^5
2 10^5
1.5 10^5
1 10^5
5 10^4
0
LA ICP-MS
Microprobe
ICP-AES
0
5
10
15
20
C.
Ce (ug/g)
1200
1000
800
600
400
200
0
LA ICP-MS
ICP-MS
ICP-AES
0
10
20
30
40
50
depth in crust (mm)

Another approach for evaluating data quality in manganese nodule samples is to monitor the relative abundance between ^{206}Pb and ^{208}Pb versus the natural abundance ratio between the two isotopes. The good agreement between measured and known isotopic ratios shown in Figure II.6, is further evidence of a good detector performance for this analysis.

5. Results and discussion

We have compiled a large data seta to document the usefulness and limitations of laser ablation coupled with ICP-MS analyses of ferromanganese and carbonate samples. To determine the usefulness of the LA ICP-MS in the analysis of geochemical phases we selected a ferromanganese nodule and a bivalve shell sample from areas of active fluid discharge to the seafloor. Results from analyses of these samples are summarized in Figure II.7.

The analysis of carbonate samples by LA-ICP-MS was reviewed by Denoyer et al., 1991. Perkins et al. (1991) measured Mg, Sr, and Pb in *Artica islandica* shells, Imai (1992) reported La and Ba analyses in fossil *Mya oonogai*, and Feng (1994) analyzed Sr, Y, Ba and REE in dolomite and calcite grains. The results from our investigations complement these studies as they provide a more thorough analyses of the behavior of the quadrupole and detectors over long analytical runs (up to 10 hrs) and enlarge the set of elements which is possible to analyze with this technique (table II.3). The data illustrate the need for constant analyses of a pressed-pellet monitor to compensate for changes in the mass response of the instrument over long periods of time. Feng (1994) noted that the relative instrument response factor might drift over time, and to compensate for this drift, he recommends repeated analysis of NIST 612 as an unknown. The disadvantage we noted with this approach when analyzing clam shells is the need to change instrument parameters within an experimental run. The laser couples best with NIST 612 glass at different frequency and voltage conditions than carbonates (table II.1); thus, a better

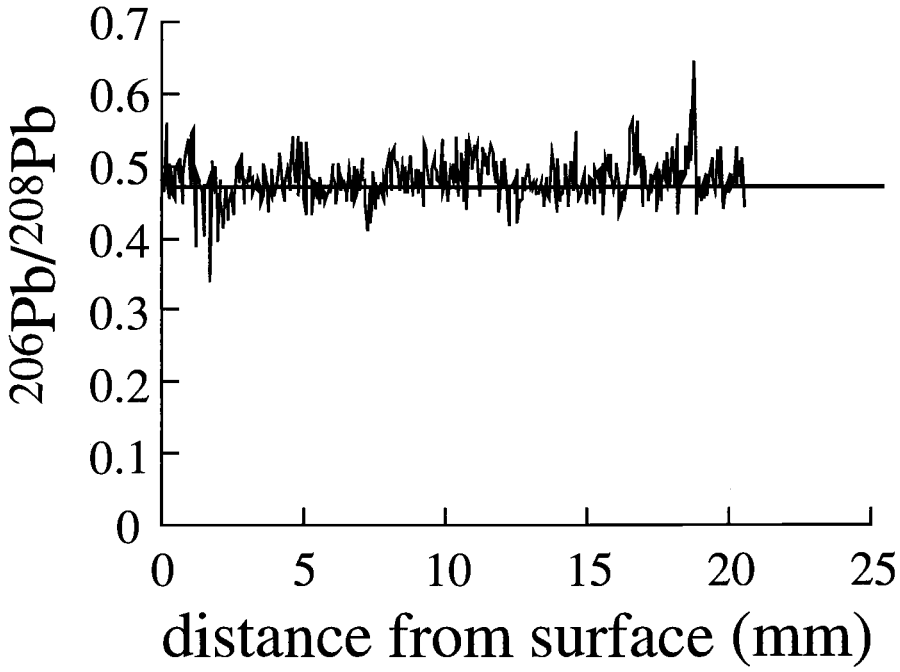

Figure II.6. $^{206}Pb/^{208}Pb$ determined by LA ICP-MS in ferromanganese crust MRF2-3R. Natural abundances (Christensen et al, 1997) in Central Pacific seamount ferromanganese crusts range from 0.4814 - 0.4878, approximately the width of the solid line

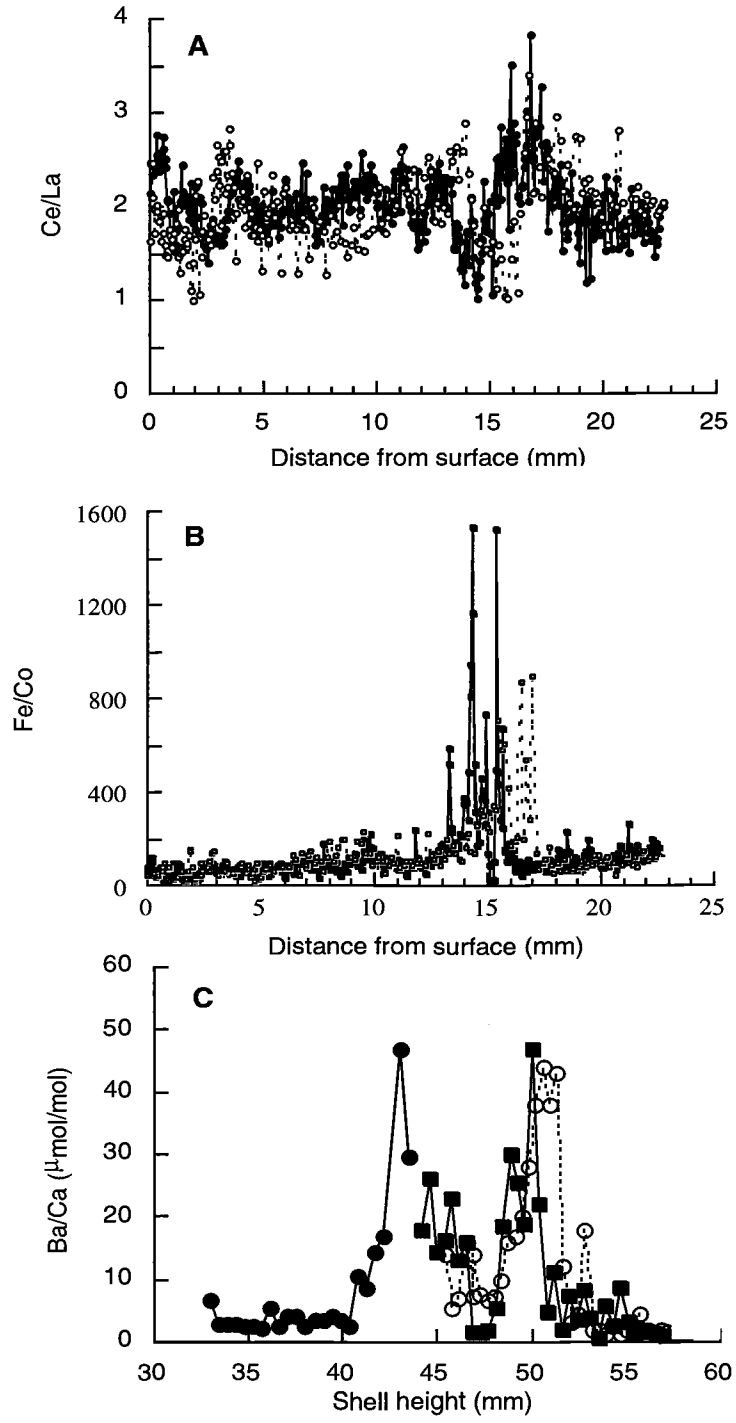

Figure II.7. Paleoenvironmental indicators in marine mineral phases. A) Ce/La ratios and B)Fe/Co ratios obtained by high-magnification LA-ICPMS analyses of manganese crust MRF2-3R from the Mendocino Ridge. C) Ba/Ca ratios obtained by low magnification LA-ICPMS analysis of bivalve shell B-30 from the Monterey Canyon. The solid and dashed lines represent data from two transects obtained during two different analytical runs. Shell height is equal to distance between umbo and sample location.

approach is to select a reference material whose ablation characteristics more closely match those of the sample.

The utility of LA ICP-MS for analyzing ferromanganese oxide formations has been documented by a number of researchers (Garbe-Schonberg and McMurtry, 1994; Christensen et al., 1997). Garbe-Schonberg and McMurtry (1994) first recognized the need for closely matrix-matching samples and standards in these phases. This work echoes the need for close matrix matching and examines large data sets obtained over long runs to demonstrate how to optimize the LA ICP-MS technique. Concentrations can be determined in a pressed-pellet standard based on response factors generated from a different standard, and the concentrations thus calculated may be compared with certified values for quality control. Elemental ratios can be monitored for further quality control by comparing measured isotope ratios in a sample with the known natural isotopic abundances. The good correlation obtained for $^{206}Pb/^{208}Pb$ is further evidence of the suitability of this technique for analyzing ferromanganese oxyhydroxide phases.

6. Geochemical significance

LA ICP-MS provides a high-resolution record of the geochemical composition of solid phases. This information is very useful for identifying changes in the environment of formation of mineral phases associated with fluid discharge episodes on the ocean floor such as hydrothermal systems and cold seeps. The episodic nature of these systems requires the use of such a proxy to reconstruct the history of fluid discharge on a vent or seep.

6.1 *Ferromanganese crusts*

Crust MRF2-3R, among the thickest ferromanganese deposits recovered from the Mendocino Ridge, shows an example of a record of such episodic fluid discharge activity. Figure II.7 A examines the Ce/La ratio, which serves as a record of relative redox intensity

(Murphy and Dymond, 1984). Figure II.7 B examines the Fe/Co ratio, which serves as a proxy for hydrothermal input in hydrogenetic ferromanganese precipitates (Halbach et al., 1983). Between the depths of approximately 13-16 mm from the botryoidal surface, concurrent maxima and minima in Fe/Co and Ce/La indicate a drastic change in the seawater from which this crust formed. The peak in Fe/Co results from both an increase in Fe concentration (likely due to a hydrothermal episode) and a drop in Co concentration (likely due to dilution be Fe phases), while the drop in Ce/La at the same horizon indicates lower dissolved oxygen levels in seawater. The idea that this may be the result of a hydrothermal episode is corroborated by higher growth rates calculated for this horizon within the crust--11.0 mm/MA vs. an average growth rate of 3.90 mm/MA for the outer 10 mm of crust (growth rates determined using the Co-based algorithm of Manheim and Lane-Bostwick, 1988). Given that this event spans only 2-3 mm within the crust, it could easily be discounted as a few bad data points (e.g. a contamination problem) had it been detected using a scraping/dissolution method with less spatial resolution.

6.2 *Carbonate samples*

Stecher al (1996) document Sr and Ba fluctuations in regular annual patterns in shells of *Mercenaria mercenaria* and *Spisula solidissima*, which demonstrate the power of this technique for extracting a time series record of seasonal geochemical cycles. Here we have expanded these investigations by analyzing specimens of bivalve shells from cold seep sites in Monterey Bay. The data for sample B-30 shown in Figure II.7 C clearly documents the usefulness of this technique for elucidating changes in the environment of growth of shells in periods of weeks to months.

7. Summary

LA ICP-MS can provide high resolution data on the geochemical composition of solid samples, as long as calibration is performed carefully and the response curve is

monitored throughout the run. While fully quantitative analysis is problematic, the technique is very useful for obtaining data when normalization either to a major element (e.g. Ca) or among elements with similar behavior (Pb isotopes, REE) is possible. These data can be extremely useful for detecting changes in the environment of formation of geochemical phases, particularly when these changes reflect events or episodes recorded in very small (few mm) areas of the solid sample. LA ICP-MS applied to such mineral phases allows for the reconstruction of the geochemical changes in past environmental conditions at a spatial and temporal resolution impossible to achieve with conventional dissolution methods.

III. A PALEOGEOCHEMICAL INVESTIGATION OF MENDOCINO RIDGE FERROMANGANESE OXYHYDROXIDES.

ABSTRACT

The Mendocino Ridge has a complex geological history. This major topographic feature, extending 3000 km westward from the California coast, was once at sea level, but has been subsiding for the past 5.5 to 8 million years. Submersible cruises have recovered a large number of ferromanganese crusts and nodules from the Mendocino Ridge. Ferromanganese oxyhydroxide phases have been the subject of a number of paleoceanographic studies because they function as recorders of surrounding seawater conditions over periods of millions of years. Changes in inter-elemental relationships within the layered ferromanganese oxyhydroxide matrix can help elucidate changes in environmental conditions such as the degree of oxia, relative water depth, and hydrothermal or diagenetic influence. This work (1) presents background information about the Mendocino Ridge, (2) reviews paleoceanographic literature related to manganese nodules and crusts, (3) presents hypotheses about geochemical records present in Mendocino Ridge manganese nodules and crusts, (4) examines a number of geochemical proxies and their relevance to Mendocino Ridge manganese deposits, and (5) discusses the results of these investigations.

1. Site description

The Mendocino Fracture Zone (MFZ) is a 3000 km long transform fault which extends westward from the San Andreas Fault at Cape Mendocino, California (Figure III.1). The crest of this fracture zone, known as the Mendocino Ridge, reaches within 1100 m of the surface. Rounded basalt pebbles and cobbles dated at 11 Ma have been recovered from locations along the Mendocino Ridge, suggesting that the crest of this ridge was at sea level in the past. Sea level exposure of this major topographic feature would most certainly have affected the local oceanic circulation, likely reducing the intensity and changing the course of the California Current. The Mendocino Ridge has been subsiding at an estimated 0.15 - 0.22 mm/yr for the past 5.5 to 8.0 My (Fisk et al., 1992).

The California Current, the major eastern boundary current of the north Pacific Ocean, passes directly over the MFZ. The majority of the transport within this current occurs within 600 km from the coast of Oregon and California, and is confined to the upper 300 m of the water column (Domack, 1986). Although deeper than the zone of influence of the California Current, strong currents to 0.5 knots occur seasonally in the study area, with a net southwestward transport (Pillsbury et al., 1982). Observations from manned and unmanned submersibles along the MFZ have revealed the area to be quite bare of sediment, likely swept away by swift bottom currents.

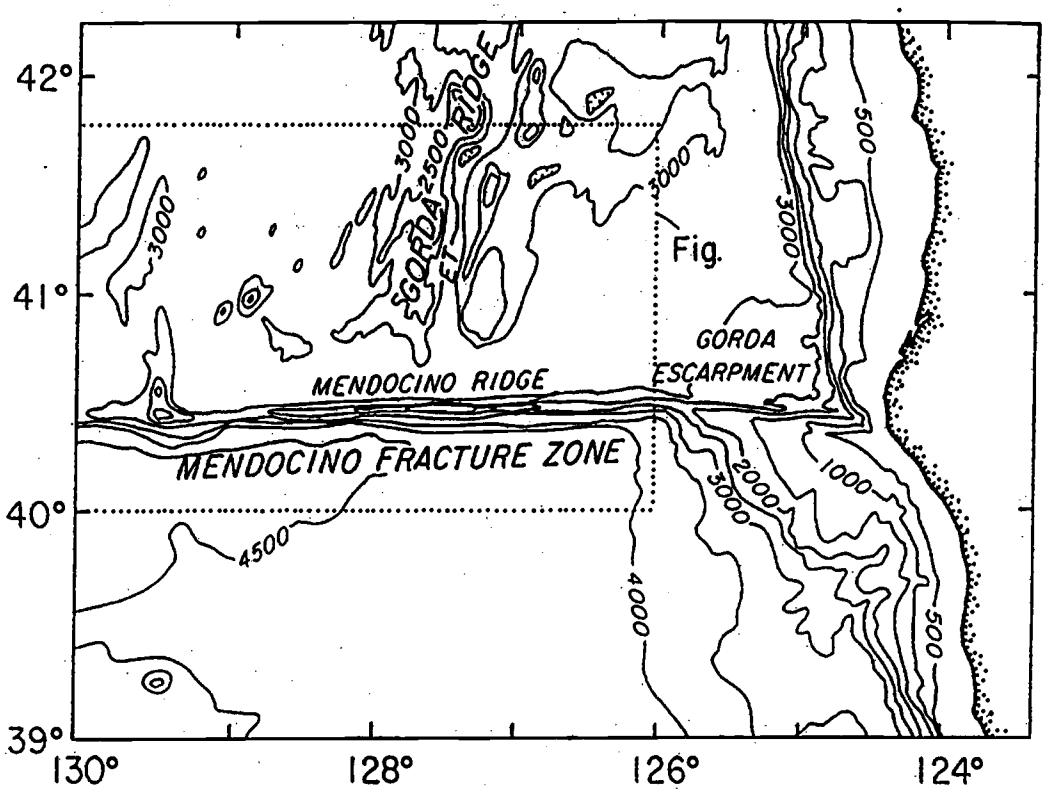

Figure III.1. Mendocino Fracture Zone bathymetry. Area enclosed by dotted lines is expanded in figure III.2. "ET," to the east of the Gorda Ridge, denotes the Escanaba Trough. Contour interval = 500 m. Adapted from Fisk et al., 1992.

Elevated productivity in the northeast Pacific results in a well-developed oxygen minimum zone (OMZ). Hydrographic data collected during the VERTEX program revealed an O_2 minimum at approximately 900 m depth at approximately 35° N, with concentrations as low as 17 μmol O_2 (Martin et al., 1985). The O_2 minimum is also the depth at which dissolved Mn concentrations are greatest (as high as 2.5 nM), due to the reduction of Mn(IV) oxides to soluble Mn^{2+} (Johnson et al., 1995).

Water column sampling along the Gorda Ridge has revealed the presence of active, high-temperature hydrothermal venting (Baker et al., 1987; Rona et al., 1998). The Escanaba Trough, the portion of the Gorda Ridge closest to the MFZ, located to the south of known high-temperature vents, contains several inactive hydrothermal deposits, and hydrothermal activity has been observed during submersible dives here (Fisk and Howard, 1990). Water column sampling has revealed elevated (4 nmol/L) dissolved Mn concentrations in the Escanaba Trough, indicating possible advection of hydrothermal fluids south toward the Mendocino Ridge (Baker et al., 1987).

1.1 Tectonic setting

The Mendocino Ridge is located in a tectonically active region. At its eastern terminus, the Mendocino Fracture Zone intersects with the San Andreas Fault and the Cascadia Subduction Zone, forming the Mendocino Triple Junction. The Mendocino Ridge drops 2100 m to the north to the Gorda Plate; to the south the Mendocino Ridge

drops 3300 m to the Pacific Ocean floor. The shallower Gorda crust to the north has been dated at approximately 7 Ma, whereas the deeper Pacific crust to the south has been dated at 27 to 32 Ma. The southern portion of the Gorda Ridge adjacent to the MFZ, the Escanaba Trough, is thickly covered with turbidites and is spreading at a slower rate (22 mm/yr) than the northern Gorda Ridge (55 mm/yr; Fisk et al., 1992). The Gorda plate, has a complex geological history. The Pacific plate, to the south, originated from a spreading center which was subducted beneath North America approximately 27 million years ago. Although the Pacific Plate is presently being subducted eastward, its motion relative to the more rapidly moving Gorda plate is westward.

1.2 Samples

More than 30 years ago, researchers dredged manganese nodules and crusts from the Mendocino ridge (Krause et al., 1964; Menard, 1964). Naydu (1965) found spherical nodules with nuclei consisting of palagonite, as well as pebbles and cobbles welded together by ferromanganese crusts. Submersible cruises in 1994 and 1995 recovered more than 140 samples of ferromanganese encrustations from the Mendocino Ridge. These samples range from thin patinas on cobbles to crusts in excess of 60 mm thick. Many of the samples consist of pebbles or cobbles cemented together with ferromanganese oxyhydroxides. Three individual samples were selected based on the following criteria: sufficient thickness for cross-sectioning and LA ICP-MS analysis,

intact botryoidal surface, and laminar internal structure. The locations from which they were recovered are noted on Figure III.2.

The fact that the Mendocino Ridge manganese deposits were collected using submersibles offers a unique opportunity: it provides firsthand knowledge of exactly where crusts and nodules were recovered. The vast majority of samples described in the literature were recovered from deep water using dredges, box cores, and similar remote sampling methods. None of these remote sampling methods allow firsthand knowledge of important environmental information such as whether a manganese oxide was growing on bare rock, lying on sediment, or buried in sediment. Such knowledge is invaluable in interpreting and assessing the results of geochemical analyses.

Sample MRF1-20R, named "cannonball nodule" because of its roughly spherical shape, measures approximately 6 cm in diameter. The sample was recovered from a shallow pocket in an exposed piece of basalt crust, and appeared to have come to rest at this location after having rolled downslope. The nodule shows no obvious signs of orientation (i.e. no distinct top or bottom). Its nucleus is composed of broken fragments of altered basalt, likely palagonite (Dymond, pers. comm. 1997). Although the palagonite has not been dated, basalts recovered in this vicinity have been determined to be 7.2 to 8.4 million years old. This nodule was recovered from a depth of 1760 m, at 40.3555° N, 129.4238° W.

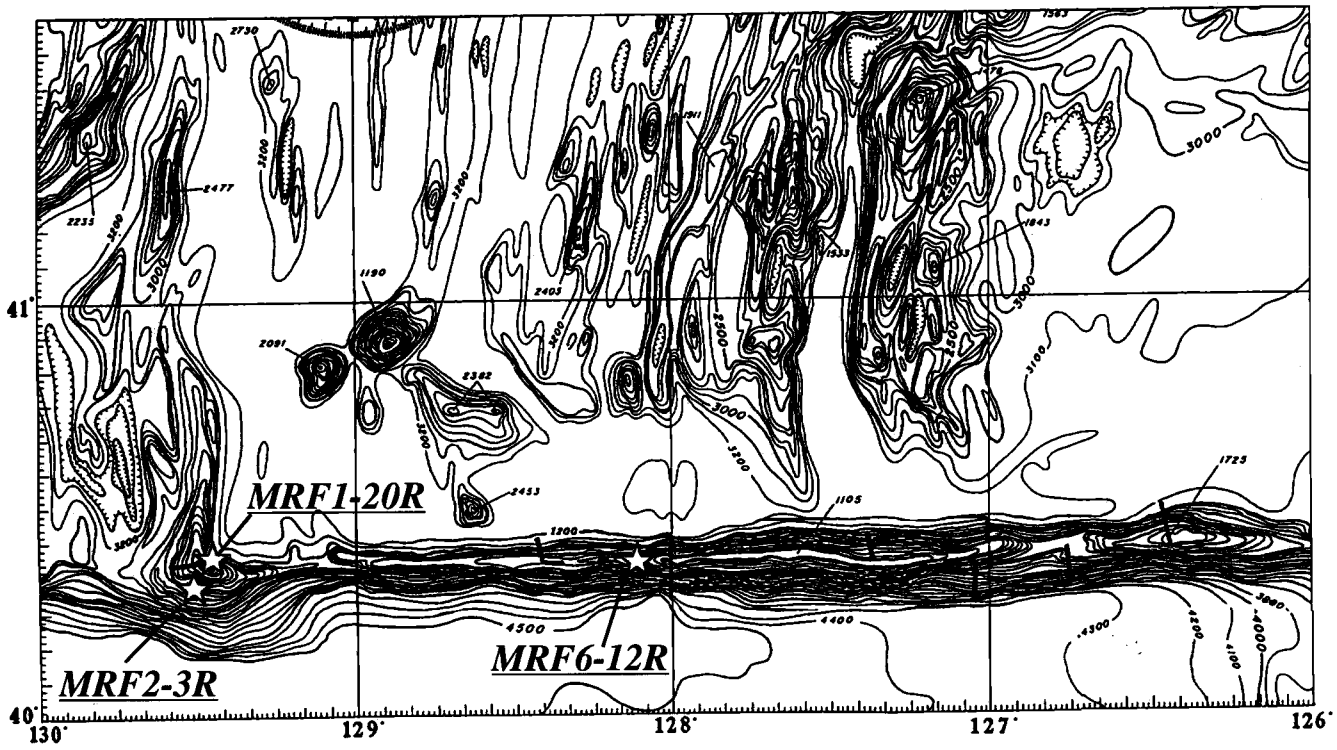

Figure III.2. Detail of Mendocino Ridge outlined in Figure III.1, showing sample locations. Contour interval = 100 m. Adapted from Fisk et al., 1992.

Sample MRF2-3R is a massive ferromanganese crust, 7.5 cm thick. Its substrate is a basalt slab with glass inclusions, dated at 11.2 ± 3.0Ma. The sample was recovered on the inside wall near the crest of a submerged caldera, at a depth of 2195 m, 40.3288° N, 129.5365° W.

Sample MRF6-12R is a ferromanganese encrustation with a basalt cobblestone substrate dated at 19.6 ± 0.4 Ma. The crust does not completely surround the cobble, and it measures 20 mm at its thickest point. This crust was recovered from a depth of 2053 m, at 40.3727° N, 128.1375° W.

1.3 Paleoceanographic background

Histories that might be recorded within the suite of Mendocino samples encompass late Miocene (approximately 5.5 Ma) through present—an interval which includes a number of events which had profound effects on world climate and oceanic circulation, culminating in a period of intense Northern Hemisphere glaciation.

In general, the late Miocene was a time of cooler conditions than had previously occurred (Keigwin, 1987). Widespread cooling is reported from 6.5 – 5.0 Ma, with very cool water masses expanding over New Zealand and California, along with colder terrestrial climates (Kennett, 1982). This cooling was accompanied by an expansion of the Antarctic ice sheets due to an increase in glaciation, intensification of oceanic circulation, steeper temperature gradients between high and low latitudes, increased

winds, increased upwelling, and a major sea level regression of approximately 40 m (Kennett, 1982; Woodruff, 1985). Increases in upwelling and associated surface productivity led to intensification of the oxygen minimum around the Pacific rim (Woodruff, 1985). Radiolarian indicators suggest that the California Current was wider at 5 Ma than at present, forcing Central Pacific Gyre waters offshore (Domack, 1986). During the interval between 6.6 – 3.5 Ma, there was a marked global increase in biogenic sedimentation rates, as much as five times greater than during the Pleistocene (Pisias et al., 1995). The latest Miocene was marked by increased glaciation in the Southern Hemisphere, the isolation and desiccation of the Mediterranean Sea, and two glacial events at 5.2 and 4.8 Ma (Keigwin, 1987). The Miocene/Pliocene boundary has been determined to be at 4.8 Ma (Ibid.).

The early Pliocene saw further intensification of oceanic circulation, but the magnitude was still lower than during the quaternary (Kennett, 1982). At 4.2 Ma there was a decrease in Antarctic ice volume. The late Pliocene marks a time of profound change—at 3 Ma there was further reduction in the Antarctic ice sheet and a global increase in sea level of 20 – 30 m (Crowley, 1996). In addition, 3 Ma marks the onset of northern hemisphere glaciation, possibly related to the final closure of the Central American seaway at 3.1 – 3.5 Ma and resulting changes in oceanic circulation patterns (Kennett, 1982; Romine,1985). Glacial deposits in the Sierra Nevada in California dated

at 2.7 – 3.1 Ma (Kennett, 1982) demonstrate the proximity of glacial influences to the Mendocino Fracture Zone study area .

During the Quaternary Period, from about 1.6 Ma to present, as many as 30 glacial episodes have occurred in the northern hemisphere, resulting in large scale changes in oceanic circulation and changes in sea level of up to 100 m (Kennett, 1982). Substantial changes in productivity and biogenic sedimentation are observed, as well as increased deposition of terrigenous sediments (Ibid.). The glacial period from 22,000 – 14,000 years b.p., which encompasses the last glacial maximum (LGM) at 18,000 years b.p., is marked by increased terrigenous sedimentation, especially via fluvial transport and increased erosion and transport of coastal sediments (Sancetta et al., 1992). This interval also exhibited lower biological productivity and weaker coastal upwelling in the Northeast Pacific (Ibid.), which would have reduced the extent and intensity of the oxygen minimum zone. Ortiz et al. (1997) determined that the waters of the California Current cooled substantially during the LGM, and that the current continued to flow in a southerly direction.

2. Methods

A number of analyses were performed on the suite of Mendocino manganese oxides to examine the chemical records that they contain. Because of the analytical difficulties associated with laser ablation inductively-coupled plasma mass spectrometry

(LA ICP-MS) discussed in chapter II, a host of complimentary analytical techniques were used for comparison. Major and trace elements in solid phases were analyzed in situ using both LA ICP-MS and electron probe microanalysis (EPMA), each technique providing high-resolution chemical profiles. Solution chemistry methods were employed for the determination of major (ICP-AES) and trace elements (ICP-AES and ICP-MS) in dissolved sample fractions. Radiometric dating techniques were used for determining growth history. The surficial layers of each sample were dated using ^{230}Th, while ^{10}Be and ^{26}Al were used to date deeper sample horizons. Minimum growth rate estimates based on substrate age and sample thickness and an empirical algorithm relating growth rate to Co, Fe, and Mn content provided non-radiometric means for dating samples.

2.1 LA ICP-MS

Laser Ablation Inductively-Coupled Plasma Mass Spectrometry (LA ICP-MS) was applied to Mendocino manganese oxides in order to determine trace element contents on a fine spatial scale, with the goal of generating high-resolution chemical profiles for sample cross sections. LA ICP-MS allows *in situ* acquisition of such data, eliminating the potential for contamination that comes with subsampling by hand and dissolving sample splits. LA ICP-MS was employed to determine a suite of more than 30 elements—high magnification mode was used for most trace metal determinations, while low magnification mode was employed for REEs, whose low concentrations require the

introduction of more sample to the ICP-MS. For a thorough review of LA ICP-MS techniques employed, refer to chapter 2. EPMA analysis of crust MRF2-3R was performed as a complimentary solid sampling technique for comparison with LA ICP-MS. ICP-AES and ICP-MS determinations were performed on dissolved sample splits to further compliment LA ICP-MS work.

2.2 EPMA

Electron Probe Microanalysis (EPMA) was employed as a means of resolving major elemental concentrations on a spatial scale similar to that of LA ICP-MS. It is possible to adjust the electron beam in order to sample an area similar in size to an ablation crater formed by LA ICP-MS. The EPMA detector's sensitivity is such that the high concentrations of Mn in ferromanganese deposits can still be analyzed although these concentrations are too high for LA ICP-MS. The EPMA technique seems to be more sensitive to changes in sample density and porosity than LA ICP-MS, which limited its utility on these samples.

Another important function of EPMA is that is was used for collecting scanning electron microscope (SEM) and backscatter electron (BSE) images of samples. BSE images reveal structural characteristics (i.e. degree of inhomogeneity, laminar versus columnar deposition, etc.) on the scale of a few μm, while SEM images allow the analyst to examine the shape and size of ablation craters and their relationship to sample

structure. Both SEM and BSE images were collected using a beam current of 20 nA. The instrument employed for this study was a Cameca SX50.

2.3 Sampling for wet chemistry and dating

Ferromanganese crusts were cut into cross sections with a rock saw and then subsampled with a dental drill (model: Brasseler UP 500) outfitted with a carbide bit. For ^{230}Th analyses, scrapings were collected over depth intervals of approximately 0.2 mm, covering a total depth range from 0.0mm - to approximately 2.0 mm. In this case, scraping depths were calculated using the weight of material collected, the area scraped (measured with a micrometer), and an assumed density of 2 g/cm^3. The layers scraped were too thin to accurately measure by hand. Average sample mass for ^{230}Th analysis was 0.002 grams, dry weight. For ^{10}Be and ^{26}Al analyses, scrapings were collected over much greater depth intervals, with layers ranging from approximately 0.1 mm thick in the outer portions of the crust to more than 7 mm thick in the inner regions of the crust. Layer depths were measured using a micrometer. Scrapings were collected onto weighing paper within a laminar flow hood to minimize contamination, weighed, dried overnight in a 100°C oven, reweighed, and then transferred into 30 ml PTFE centrifuge vials for dissolution.

2.4 Digestions

Dissolution was initiated by adding 6 N HCl to the powdered ferromanganese oxyhydroxide material (table III.1), followed by the addition of Ultrex H_2O_2, which facilitates breakdown of dissolution-resistant manganese oxides. Samples were placed into a heating block overnight until almost dry, followed by addition of equal volumes of teflon subboiling distilled HF and 16 N HNO_3 (both double quartz-distilled). Samples were capped and placed into an ultrasonic bath for one hour and then placed in a heating block at 65°C overnight. Subsequently the samples were placed into an ultrasonic bath for another hour, and the acid mixture was evaporated using a heating block at 95°C. When the samples were nearly dry, two separate aliquots of 6 N HCl were added to drive off HF, with a 95°C dry-down step following each addition. An aliquot of 16 N HNO_3 was added, followed by a dry-down step at 95°C. When samples were nearly dry, two separate aliquots of 8 N HNO_3 were added, with a 95°C dry-down step following each addition. When nearly dry, samples for Th analysis were diluted into 5 ml of 0.2 N HNO_3, and allowed to stabilize overnight before being shipped to the Institute of Earth Sciences, Academia Sinica, for alpha mass spectrometry analysis. Samples for other chemical analyses were diluted into 25 ml of 0.2 N HNO_3 and allowed to stabilize overnight before further manipulation. From each 25 ml dissolved sample, a 5 ml aliquot was withdrawn for ICP-AES and ICP-MS analysis of major and trace elements; the remainder was used for Be and Al elutions.

		^{230}Th	^{10}Be
	Sample Mass (g)=	0.002	0.25
Step 1	HCl (6N)	1 ml	20 ml
	H_2O_2 (30%)	0.1 ml	0.1 ml
Step 2	HNO_3 (16N)	500 ml	2 ml
	HF (conc.)	500 ml	2 ml
Step 3	HCl (6N)	2 X 0.5 ml	2 X 2 ml
Step 4	HNO_3 (16N)	1 ml	2 ml
Step 5	HNO_3 (8N)	2 X 0.5 ml	2 X 1 ml
Step 6	HNO_3 (0.2N)	5 ml	25 ml

Table III.1. Nodule dissolution procedure.

2.5 Chromatographic separation

The separation of Be and Al from other metals in the ferromanganese oxyhydroxide matrix and the purification of their oxide forms is necessary for radiometric dating. For this purpose hydroxide coprecipitation and ion chromatography techniques (using a simple gravity-flow column) were employed. 1 mg of Be carrier, (1.0 ml of 1000 µg/ml Be ICP-MS standard) was added to each 20 ml aliquot of dissolved sample remaining after digestion. Concentrated NH_4OH was added until hydroxides of Fe, Be, and Al precipitated from the mixture. The precipitates were then centrifuged and rinsed with deionized water three times. The rinsed precipitate was dissolved in 1.1M HCl (volume equal to the respective column volume) plus 1-2 drops of Ultrex H_2O_2, and the resulting solution was loaded into a gravity-flow chromatography column made of Teflon PFA with Teflon NPT fittings, packed with BioRad AG50W-X8 cation exchange resin (200-400 mesh). Column volumes were calibrated (three replicates), and the resin was cleaned before each elution by flushing with 6 N HCl, deionized H_2O, and 1.1 N HCl.

Elution with 1.1 N HCl causes Be to pass through in column volumes 9-12 (Figure III.3). Column volumes containing Be were collected and nearly dried. As boron constitutes a mass interference for ^{10}Be, samples were fumed five times with 100 ml $HClO_4$ to drive off boron. When nearly dry, two 0.5 ml aliquots of 6 N HCl were added and subsequently evaporated to decompose the $HClO_4$, and the nearly dry sample was

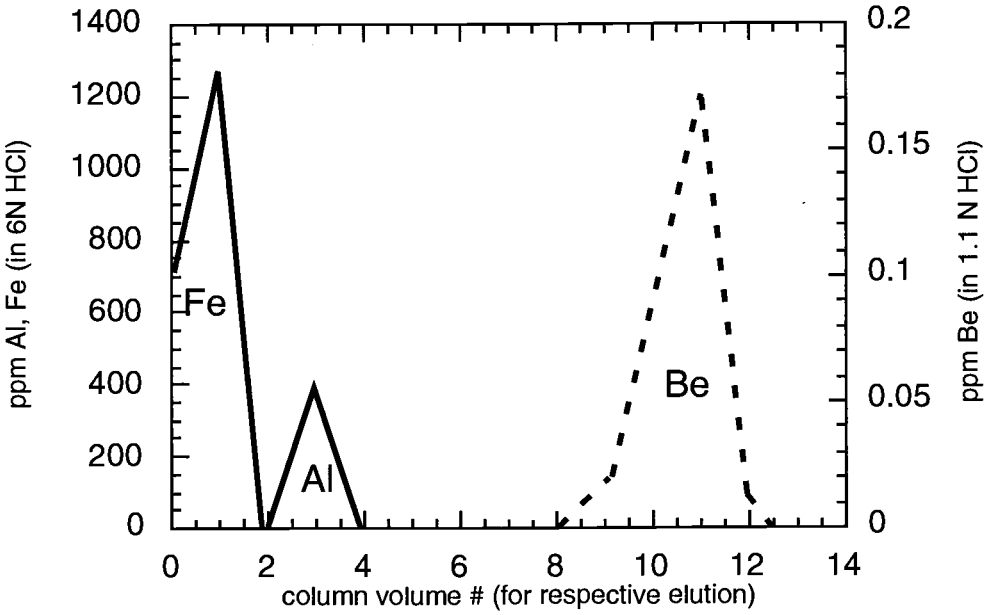

Figure III.3. Elution behavior of Be (in 1.1N HCL), Fe, and Al (in 6N HCl) from cation exchange column used for separating and purifying analytes from dissolved manganese nodule and crust scrapings. Column volume numbers refer to volumes for respective reagents (i.e. Be comes off in column volumes 9-12 when eluting with 1.1 N HCL, then Fe and Al come off in column volumes 1-4 when eluting with 6N HCl).

dissolved into 2 ml H_2O. NH_4OH was added (~200 µl) to the resulting solution until $Be(OH)_2$ visibly precipitated.

Elution with 6 N HCl causes the release of Al and Fe from the cation exchange resin. Both elements are eluted in the first three column volumes. The aliquot containing Fe and Al was nearly dried, and then redissolved in 9 N HCl (volume equal to the column volume of the anion exchange column). The 9 N solution was loaded into an acid-cleaned glass column loaded with BioRad AG1-X8 anion-exchange resin (100-200 mesh). As the solution passes through the anion-exchange column, Fe is retained and Al is eluted. The eluent was evaporated to a small volume, and then taken up in 5 ml of deionized H_2O. NH_4OH (~100 µl) was added to precipitate $Al(OH)_3$.

Precipitates of $Be(OH)_2$ and $Al(OH)_3$ were centrifuged and rinsed three times with deionized H_2O, transferred into weighed, acid-cleaned quartz beakers, and heated for several hours in a muffle furnace at 950°C to convert them to their respective oxide forms.

2.6 ICP-AES

Inductively-Coupled Plasma Atomic Emission Spectrophotometric (ICP-AES) analyses were performed for the determination of major elements in dissolved nodule and crust samples using a Varian Liberty 150 ICP-AES. Elements of interest and wavelengths analyzed included Fe (261.19 nm), Mn (293.93 nm), Al (396.15 nm), Co

(228.62 nm), Ni (231.60 nm), Cu (324.75 nm), Zn (213.86 nm), and Ce (413.38 nm). Four point standard curves bracketing expected concentrations for each element were run, followed by samples, liberally interspersed with blanks and replicate standards for data quality assurance. Replicates of dissolved USGS manganese nodule standard Nod A-1 were also run. Calculated concentrations for Nod A-1 were within 5% of certified values, except for Ce, for which many samples yielded intensities less than that of the blank.

To investigate matrix effects upon samples bearing varying amounts of dissolved solids, a standard addition experiment was performed. The results yield calibration curves with slopes approximately parallel to those from simple standard curves, demonstrating that matrix effects are negligible.

2.7 ICP-MS

Traditional solution-based Inductively-Coupled Plasma Mass Spectrometry (ICP-MS) was utilized for the determination of ^{9}Be and Ce in dissolved splits from crust samples MRF2-3R and MRF6-12R. Determination of ^{9}Be is necessary for ^{10}Be growth rate calculations, and both ^{9}Be and Ce (in many samples) are below detection limits for ICP-AES. A Fisons VG PlasmaQuad PQ 2+ Inductively Coupled Plasma Mass Spectrometer was employed, along with an autosampler. Four point standard curves were run, with concentrations of the standards bracketing those expected in the samples.

3. Growth rate determinations

A variety of techniques were used to determine growth rates for Mendocino Ridge ferromanganese oxides: 1) radionuclide methods, including ^{10}Be, ^{26}Al, and ^{230}Th; 2) the "cobalt chronometer," an empirical algorithm relating Co concentration to Fe + Mn content; and 3) an estimate of minimum growth rate derived from nucleus/substrate age and oxide thickness. Due to different limitations inherent in the techniques (e.g. different half lives for different radionuclides), each yields dates or growth rates with a different resolution.

3.1 ^{10}Be and ^{26}Al

Beryllium and aluminum both have naturally occurring cosmogenic isotopes (Table III.2) which have been widely used to date marine sediments and rocks (Sharma et al., 1987; Sharma et al., 1989). There are seven isotopes of Be, two of which, ^{7}Be and ^{10}Be, are cosmogenic, produced by cosmic ray spallation reactions with oxygen and nitrogen in the atmosphere. ^{10}Be is useful for long time scales, with a half-life of 1.5 Ma, and a decay by beta emission to ^{10}B. Estimates of average global production of ^{10}Be yield 2×10^{-2} atoms/cm^2/second (Faure, 1986). Aluminum has 9 isotopes; ^{26}Al and ^{27}Al are naturally-occurring. ^{27}Al is stable, while ^{26}Al is radioactive, produced by cosmic ray protons and Ar in a spallation reaction. Faure (1986) estimated production of ^{26}Al to be

	^{10}Be	^{26}Al
source	cosmogenic	cosmogenic
decay mechanism	β emission to ^{10}B	positron emission & electron capture to ^{26}Mg
est. global production (Faure, 1986)	2×10^{-2} at/cm^2/sec	1.4×10^{-4} at/cm^2/sec
half-life	1.5 Ma	0.716 Ma

Table III.2. 10Be and 26Al systematics.

1.4×10^{-4} atoms/cm^2/second. ^{26}Al has a half-life of 0.716 Ma and decays via positron emission and electron capture to stable ^{26}Mg.

While some of the ^{26}Al and ^{10}Be reaching the Earth's surface are associated with cosmic dust, only a very small fraction of these elements recorded in the geologic record is attributed to this source. The vast majority of ^{10}Be and ^{26}Al that reaches the Earth is produced in the atmosphere and then falls to the Earth's surface in rain and snow, where it partitions strongly onto soils and sediment (Tera, 1986). Cosmogenic Be and Al enter the oceans in ionic form, where they mix with their respective stable isotopes. These ions are rapidly hydrolyzed and quickly removed from surface waters by scavenging onto particulate matter. Faure (1986) reports residence times of 15.6 years in the surface ocean and 630 years in the deep ocean for Be. The residence time of 15.6 y in the surface ocean is comparable to its horizontal mixing time, which tends to smooth out short term variations in ^{10}Be input due to regional precipitation patterns, latitudinally- and seasonally-dependent variations in production rates, etc. Likewise, the residence time of Be in surface seawater is sufficiently long to reduce latitudinal variations in the deposition rate of ^{10}Be. Therefore, the deep sea sediment record is fairly uniform, independent of latitude, with some exceptions in polar regions likely due to ice cover. Recent research into Be geochemistry has demonstrated that edge effects are important in ^{10}Be distribution, as enhanced scavenging along continental margins removes more Be

from surface waters and reduces its residence time (Anderson et al., 1990; von Blanckenburg et al., 1996a).

Given its particle reactive nature, ^{10}Be is readily scavenged by manganese oxides. Once incorporated into a nodule or crust, there is evidence of very little post-depositional diffusion or diagenetic alteration (Huh and Ku, 1990). This, coupled with its long half-life, makes ^{10}Be an ideal radionuclide for dating purposes.

As ^{10}Be is present in very low concentrations in nature, analysis of this isotope requires the use of highly sensitive techniques. Von Blanckenburg et al. (1996a) report ^{10}Be concentrations of 1×10^{10} atoms/g for young marine sediments and 7×10^{5} atoms/l in surface seawater. Accelerator Mass Spectrometry (AMS) is routinely employed for measuring ^{10}Be. Using this method, samples are spiked with a ^{9}Be carrier, and then a precipitate of Be $(OH)_2$ is formed. The Be $(OH)_2$ is converted to BeO, and its $^{10}Be/^{9}Be$ ratio is measured. The initial ^{9}Be present before the spike is added is negligible. $^{10}Be/^{9}Be$ ratios of 1×10^{-15} are routinely resolved using AMS. Von Blanckenburg et al. (1996a) report precision $\pm$ 5%, with a detection limit of 0.5×10^{5} atoms (total) for AMS. The background concentration of the ^{9}Be in the samples is determined by a separate technique, such as GFAAS or ICP-MS. To eliminate matrix effects and to preconcentrate the analyte, Be is commonly extracted from samples using hydroxide coprecipitation, chromatography, solvent extraction and complexation, or a combination of the aforementioned methods.

AMS analysis of Mendocino manganese oxides was performed at Purdue University's P.R.I.M.E. lab, which offers a facility based upon an 8MV tandem electrostatic accelerator, with resolution of up to 1 ion/1 x 10^{15} stable atoms.

3.2 ^{230}Th excess

In this study, ^{230}Th excess dating was performed on all three samples using alpha spectrometry as described by Huh et al., 1989. Due to the relatively short half-life of ^{230}Th, 75 Ka, its use as a geochronometer is limited to only the outermost few millimeters of a typical nodule or crust. For this reason, it is necessary to subsample crusts and nodules at a finer resolution (sample intervals on the order of 0.1 mm) for ^{230}Th dating than for ^{10}Be or ^{26}Al dating (sample intervals on the order of 1 mm). Despite the depth limitations of ^{230}Th growth profiles, the use of this technique is firmly established for dating ferromanganese oxides (Huh and Ku, 1990; Huh et al., 1989; Eisenhauer et al., 1992; McMurtry et al., 1994).

For ^{230}Th excess dating, scraped samples were spiked with ^{236}U and ^{229}Th, and dissolved in 8N HCl with a few drops of H_2O_2 added. The samples were then centrifuged to separate the insoluble residues (aluminosilicates) from the leachate. The leachate from each sample was passed through anion exchange column (BioRad AG1x8, 100-200 mesh) pre-conditioned with 8N HCl to separate isotopes of uranium (retained on column)

from thorium (in the eluent). Following the passage of sample solution, which was collected in a beaker, two more column volumes (c.v.) of 8N HCl were used to elute Th off of the column more completely. Uranium was then washed down with 3 c.v. of 0.1N HCl and collected in a beaker.

The Th fraction (in 8N HCl) was evaporated to dryness, converted to 8N HNO_3 and passed through another anion exchange column pre-conditioned with 8N HNO_3. After the sample solution had all passed, the column was washed with 3 c.v. of 8N HNO_3 to remove aluminum completely. Thorium isotopes retained on the column were then eluted down with 3 c.v. of 8N HCl and collected in a beaker. The eluent containing Th was evaporated to dryness. If copious amounts of residue developed upon dryness of the sample solution, the residue was redissolved in 8N HNO_3 and the column operation described above was repeated. "Al-free" Th, as indicated by a nearly "clean" beaker, was then taken up with ca. 1 ml of 0.1 N HNO_3 and transferred to a centrifuge tube. Th was extracted from the aqueous phase into ca 1 ml of 0.25M TTA-benzene. The extraction was repeated and the organic phase combined and mounted onto a stainless steel disc for alpha-spectrometry.

The steps for U purification were similar to those for Th purification, except that: 1) U was eluted with 0.1N HCl, and 2) The purified U fraction was picked up with 0.1N HNO_3, and adjusted to pH = 3 by 1M NaOH. U isotopes were extracted from the

aqueous phase into TTA-benzene. The extraction and mounting (i.e. source preparation) procedures are the same as with Th.

Alpha spectrometry was employed to obtain activities of ^{238}U, ^{234}U, ^{232}Th, ^{230}Th and ^{228}Th. Excess ^{230}Th was calculated from the relationship: $^{230}Th_{excess} = {}^{230}Th - {}^{234}U$. Alpha spectrometric analyses were performed by Chih-An Huh, of Taiwan's Institute of Earth Sciences, Academia Sinica.

3.3 Co chronometer

Manheim and Lane-Bostwick (1988) developed a growth rate model for ferromanganese oxides based on the inverse relationship between cobalt content and growth rate, which they named the 'cobalt chronometer.' The authors normalized weight percent cobalt to iron + manganese by:

$$w^n_{Co} = w_{Co} * 50/(w_{Fe+Mn})$$

where w_{Co} = weight percent Co and w_{Fe+Mn} = percent by weight Fe + Mn. Accumulation rate was found to be an inverse logarithmic function of cobalt content described by:

$$R = 6.8 \times 10^{-1}/(w^n_{Co})^{1.67}$$

where R = accumulation rate (mm/Ma). Unlike other empirical growth rates proposed in the literature (e.g. Puteanus & Halbach, 1988, which only applies to hydrogenetic crusts with Co concentrations greater than 0.24%) the authors report that this function applies

consistently to crusts and other manganese oxide deposits (e.g. hydrothermal oxides). Furthermore, the authors use the Co chronometer to calculate accumulation rates ranging from <1 mm/Ma in hydrogenetic crusts from the Central Pacific to >1000mm/Ma in hydrothermal deposits. Frank et al. (1999) confirmed the Co chronometer's validity as a dating technique by comparison with ^{10}Be profiles in a number of crusts from the Atlantic, Pacific, and Indian Oceans. An important limitation of this dating technique is that it is not sensitive to hiatuses in formation nor does it account for portions of crust stratigraphy that may be missing (i.e. broken off).

3.4 Minimum growth rate calculations

Minimum growth rates were calculated for the purpose of constraining other dating techniques. Crust substrate basalts were dated using the K-Ar technique (for a review see Dalrymple and Lanphere, 1969). The thickness of each ferromanganese oxide was divided by its substrate age to calculate a minimum growth rate. In the case of nodule MRF1-20R, whose nucleus is composed of palagonite (an altered basalt unsuitable for the K-Ar dating technique) fragments, the substrate was assumed to be the same age as nearby basalts. A limitation implicit in this technique is that it assumes continuous growth at a constant rate, something that other dating techniques reveal to be

an inaccurate assumption. Therefore this technique only provides a minimum estimate of growth rate for comparison purposes.

3.5 Results from this study

Growth rates were calculated for all Mendocino Ridge samples using ^{230}Th and the cobalt chronometer, and minimum growth rates were calculated for each sample based on substrate age and thickness. Additionally, ^{10}Be and ^{26}Al growth rates were determined for samples MRF2-3R and MRF6-12R (Table III.3).

The ^{230}Th growth rate determinations for MRF1-20R, the "cannonball" nodule, yielded accretion rates of 3.6 mm/Ma for the outer 1.23 mm of the nodule and 22 mm/Ma from 1.23 – 3.18 mm in the nodule, a dramatic shift in growth history (Figure III.4). A minimum growth rate of 2.7 – 3.2 mm/Ma was calculated based on a substrate age of 7.2 - 8.4 Ma and an oxide thickness of 23 mm. This value agrees with the ^{230}Th growth rate determination on the outer crust. The growth rate calculated by the Co chronometer for the outer 3.25 mm of the nodule averages 2.3 mm/Ma, slightly less than the minimum growth rate estimate (Figure III.5). Deeper strata within the nodule yield higher Co chronometer growth rates, increasing between 4-8 mm depth to a maximum value of 53 mm/Ma at 5.86 mm depth, after which the growth rate levels off to an average of 4.9 mm/Ma between 8 – 9 mm. No growth rate calculations were made beyond 9.13 mm

	minimum growth rate (mm/Ma)	^{230}Th (mm/Ma)	Co chronometer (mm/Ma)	^{10} Be (mm/Ma)	^{26}Al (mm/Ma)
MRF1-20R	2.7 to 3.2	3.57 (0 - 1.23 mm)	1.9 (0 - 1.23 mm)	N/A	N/A
		22.2 (1.23 - 3.18 mm)	2.3 (1.23 - 3.18 mm)		
MRF6-12R	1.36	6.26 (0 - 1.60 mm)	4.2 (0 - 1.60 mm)	4.62 (0 - 5.83 mm)	8.87 (0 - 12.65 mm)
				18.93 (5.83 - 26.70 mm)	
MRF2-3R	6.7	2.31 (0 - 1.24 mm)	3.21 (0 - 1.72 mm)	1.22 (0-2.24 mm)	
				6.85 (0 - 16.25 mm)	8.18 (0 - 16.25 mm)
				14.3 (16.25 - 45.00 mm)	

Table III.3. Summary of growth rate determinations. Values in parentheses are depths over which growth rates were calculated.

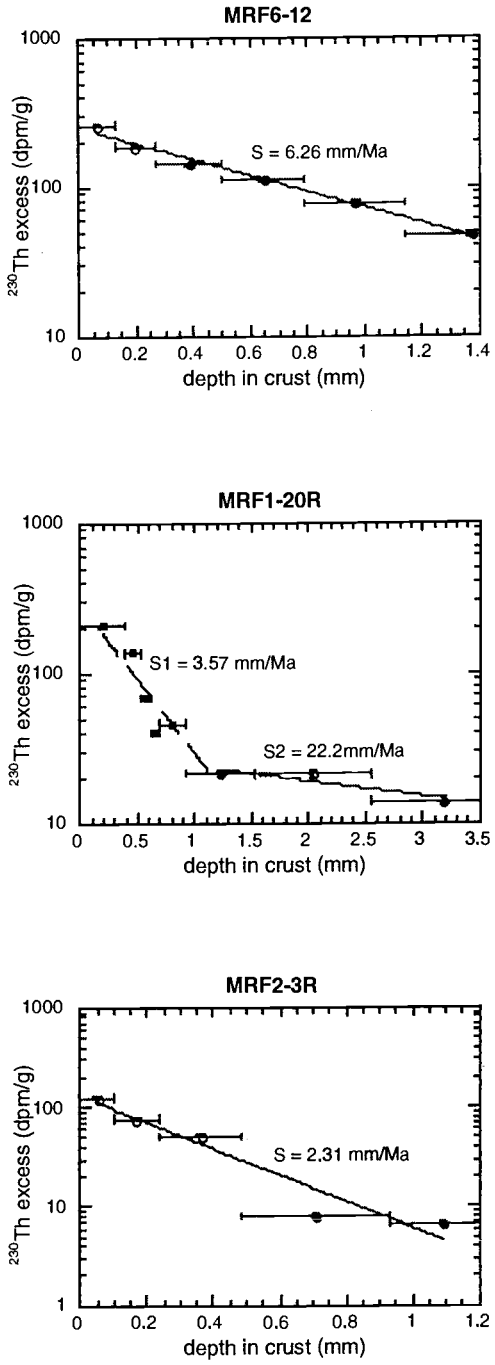

Figure III.4. ^{230}Th excess growth rate curves for Mendocino Ridge manganese deposits. Data courtesy of C.-A. Huh.

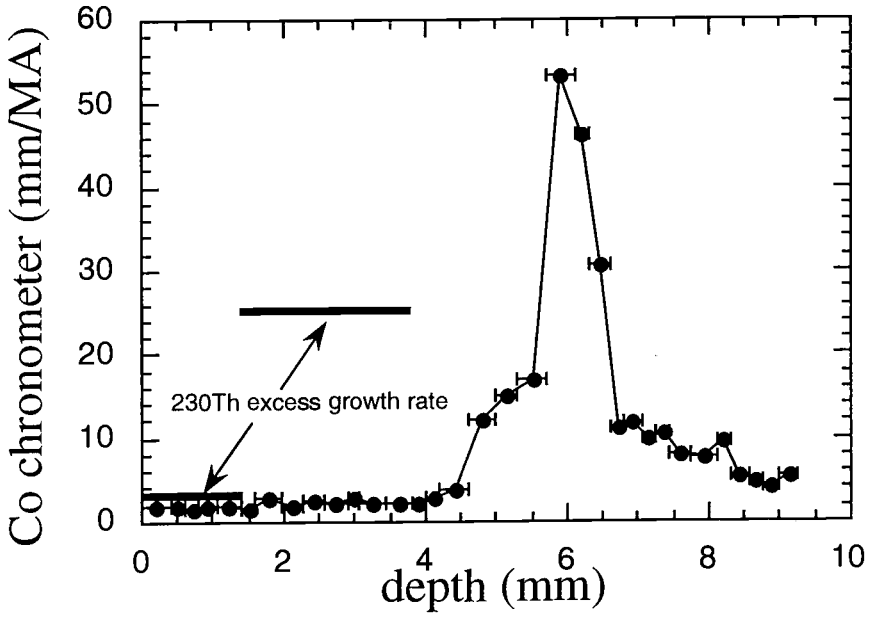

Figure III.5. Growth rates calculated using Co chronometer for nodule MRF1-20R scrapings. ^{230}Th excess growth rates are shown for comparison

depth because of difficulties with sample breakage. Ages for individual layers were calculated from the Co chronometer growth rates, but the ages calculated for the deepest layers of the nodule using this model were significantly older than the age of the nucleus. Extrapolating the growth rate of 4.9 mm/Ma determined for the 8 – 9 mm section of the nodule into the deeper portions of the nodule yields a calculated age for the onset of oxide precipitation of 5.3 Ma, which is well within the 7.2 to 8.4 Ma age constraints set by the nodule's nucleus. This extrapolation using a constant growth rate is not particularly likely to be valid, given the complex growth history exhibited in the outer portion of the nodule. No ^{10}Be or ^{26}Al determinations were made for this nodule.

^{230}Th growth rate determinations for MRF2-3R yield 2.3 mm/Ma for the outer 1.24 mm of crust (Figure III.4). The Co chronometer yields a growth rate of 3.2 mm/ma for the outer 1.72 mm of crust (Figure III.6). ^{10}Be determinations yield growth rates consistent with ^{230}Th over the outer 2 mm, but growth rates increase to 6.9 mm/Ma over the interval 0.00 – 16.25 mm, and 14 mm/Ma for the interval from 16.25 – 45.0 mm (Figure III.6). ^{26}Al counting statistics were poor, but yield a growth rate of 8 mm/Ma over the interval from 0.00 – 18.55 mm (Figure III.6). Co chronometry yields growth rates ranging from approximately 2 mm/Ma at the surface to a maximum of 11.0 mm/Ma at 16.25 mm depth. A minimum growth rate calculation based on an oxide thickness of 75 mm and a substrate age of 11.2 Ma yields 6.7 mm/Ma. Age profile calculations based

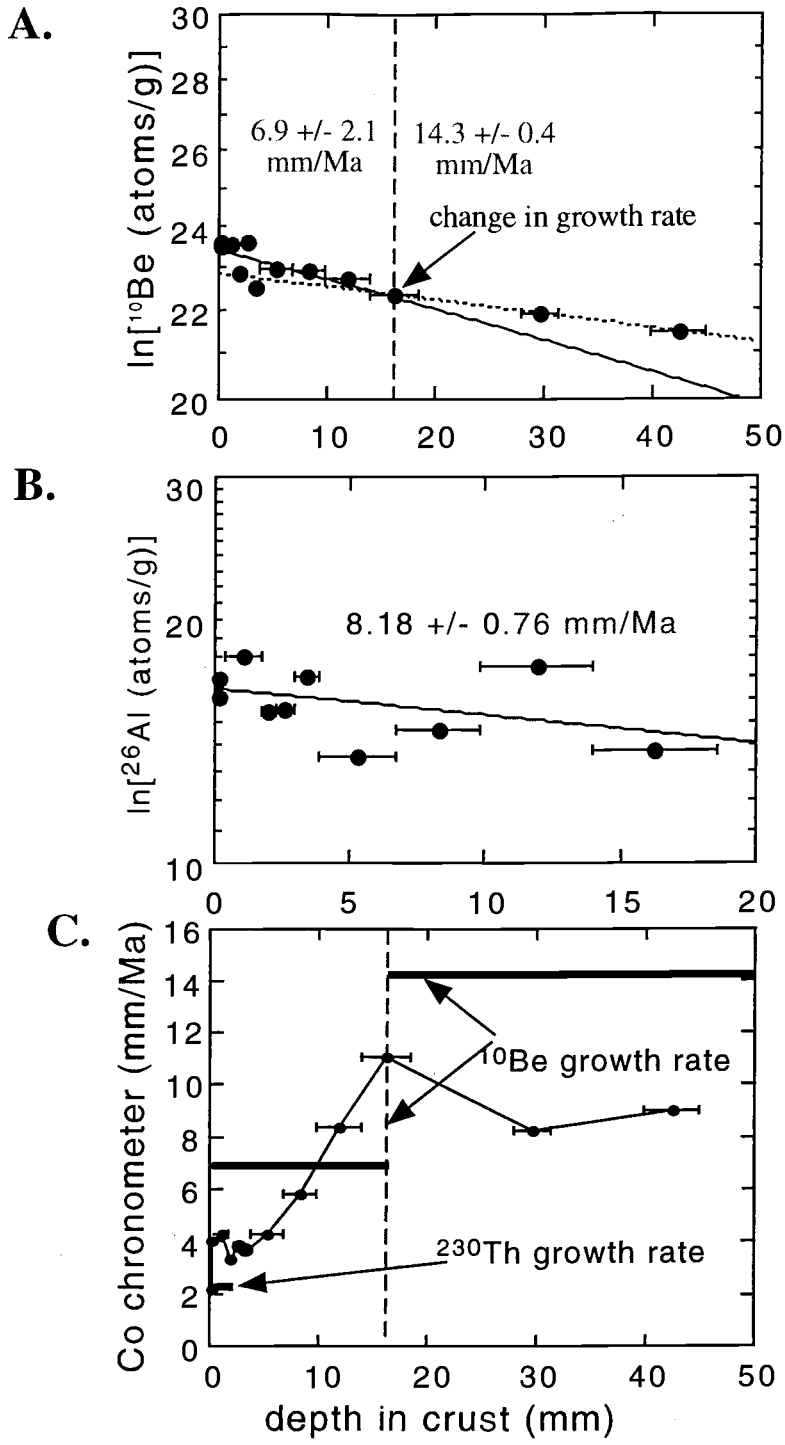

Figure III.6. Growth rate determinations for crust MRF2-3R using (A) ^{10}Be, (B) ^{26}Al, (C) ^{230}Th excess, and (C) Co chronometer methods. Error bars indicate depths of scraped layers. Width of bar indicating ^{230}Th excess growth rate in C is equal to depth over which calculations were made.

on the ^{10}Be and Co chronometer growth curves agree well, yielding ages of 5.5 and 6.3 Ma respectively for the onset of oxide formation.

^{230}Th determinations for MRF6-12R yield a growth rate of 6.3 mm/Ma for the outer 1.60 mm of crust (Figure III.4). The Co chronometer averaged over the first 1.60 mm yields a growth rate of 4.2 mm/Ma. ^{10}Be data for the outer 2.00 mm of crust do not compare well with either the Co chronometer or ^{230}Th values. Deeper in the crust, Co chronometer growth rates reach a plateau at 4.6 mm/Ma, followed by an increase to a maximum of 6.1 mm/Ma at 5.83 mm depth, beyond which point growth slows to approximately 5 mm/Ma (Figure III.7). ^{10}Be yields a growth rate of 4.6 mm/Ma for the outer 5.83 mm of crust, increasing to 19 mm/Ma over 5.83 – 26.70 mm (Figure III.7). ^{26}Al counting statistics were poor, but yielded a growth rate of 9 mm/Ma for the outer 12.65 mm of crust. A minimum growth rate calculation based on a thickness of 26.7 mm and a substrate age of 19.6 Ma yields 1.4 mm/Ma; however, given the complex tectonic history of this older substrate (formation on the seafloor, uplift, erosion into a cobblestone, and subsidence all occurred before Mn oxide precipitation initiated), this growth rate must be a severe underestimate. Age profiles calculated from ^{10}Be and Co chronometer growth curves yield very different results: the ^{10}Be profile yields an age of 2.4 Ma for the deepest part of the crust, while the Co chronometer yields an age of 5.5

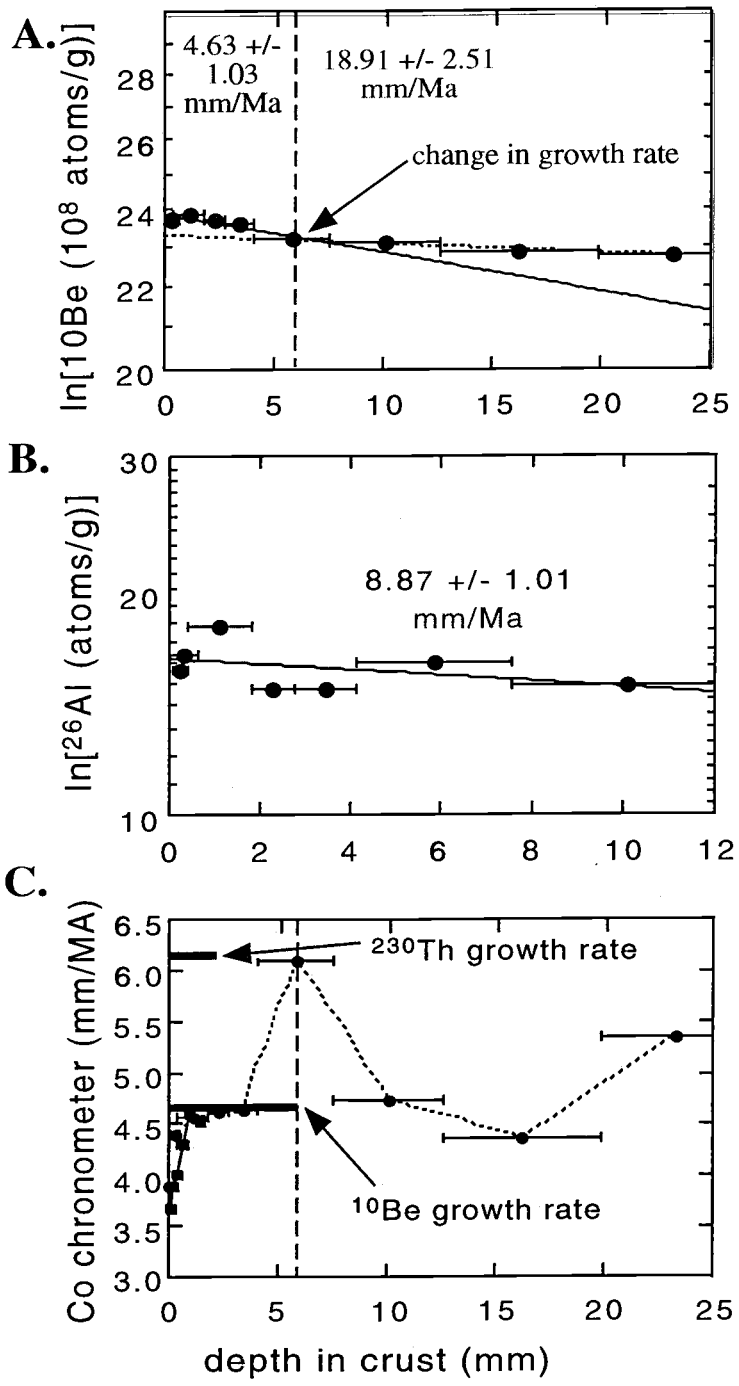

Figure III.7. Growth rate determinations for crust MRF6-12R using (A) ^{10}Be, (B) ^{26}Al, (C) ^{230}Th excess, and (C) Co chronometer methods. Error bars indicate depths of sraped layers. Width of bar indicating ^{230}Th excess growth rate in C is equal to depth over which calculations were made.

Ma for the onset of oxide precipitation. There is no obvious reason to doubt the ^{10}Be data, however, for which counting statistics yield an error of 5.5% or less.

The fact that all of the manganese oxides studied show evidence of periods of sustained faster growth in the past suggest that there were periods during which Fe and or Mn were being supplied much more rapidly than at present. Such changes may have resulted from hydrothermal episodes, substantial changes in the local redox conditions due to changes in oceanic circulation, or changes in productivity affecting sedimentary and/or water column redox processes. However, the fact that the major changes in growth rates are not synchronous across the suite of samples suggests that the environmental factors responsible for changes in growth rates are not large scale phenomena, but are likely more regional events (i.e. localized hydrothermalism). Interrelationships between major and trace elements can further elucidate contributions from individual sources of metals.

3.6 ^{232}Th profiles and terrigenous influence

The distribution and dynamics of thorium in the marine environment have long been a topic of interest. Huh and Ku (1990) describe trends in ^{232}Th distributions in ferromanganese nodules and crusts. Upon examining a number of crusts (both hydrogenous and hydrothermal) and nodules (top sides only, to eliminate sources of Th

other than hydrogenetic) from a variety of locations in the Pacific, the authors noticed a pattern which was repeated in the ^{232}Th profiles of many samples—there exists a peak in concentration slightly beneath the surface of the deposit, beneath which concentrations drop off and hover around a lower value. The authors attribute this distribution to enhanced supply of Th from aeolian sources, and provide corroborative evidence from sediment cores. The authors conclude that the aeolian flux of Th changed little over the 10 Ma preceding 3 Ma, increased dramatically during the interval from 1-3 Ma, and reached a maximum at approximately 0.1 – 0.3 Ma. The increase in Th flux is attributed to a drastic increase in aeolian flux due to the onset of Pleistocene glaciation.

The suite of Mendocino samples was examined for evidence of such a horizon that might serve as a chronometric layer. Of the suite of Mendocino samples, crust MRF2-3R exhibits such a trend in ^{232}Th distribution. The records from crust MRF6-12R and nodule MRF1-20R are inconclusive. ^{10}Be dating reveals that crust MRF6-12R is only 2.4 Ma old, which is younger than the onset of elevated Th flux. Nodule MRF1-20R likely rolled around often before coming to rest in the location from which it was recovered. The results of low magnification LA ICP-MS analysis of MRF2-3R show a clearly-defined ^{232}Th maximum of approximately 70 ppm at 0.2 Ma (^{10}Be dating), followed by gradually reduced concentrations, but with another smaller peak (44 ppm) at 2.7 Ma (Figure III.8 A). High magnification data for MRF2-3R show a general trend of

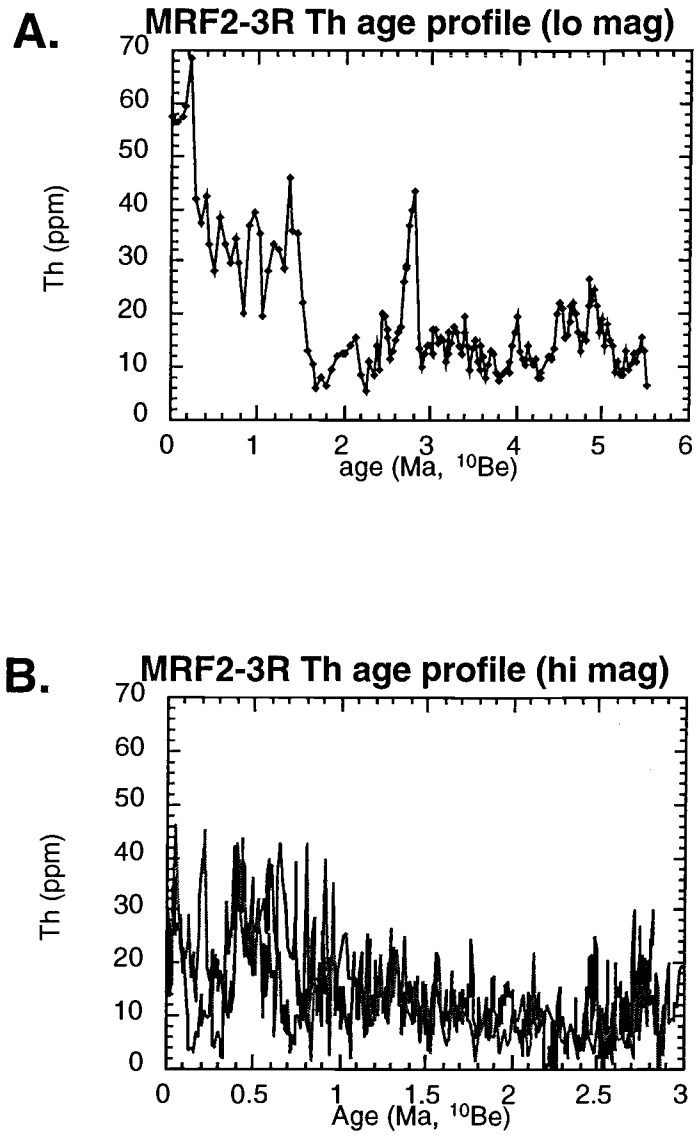

Figure III.8. ^{230}Th profiles vs. age in Mendocino crust MRF2-3R. A) Low magnification LA ICP-MS data. B) High magnification LA ICP-MS data, 2 different runs.

higher concentrations near the surface, with decreasing concentrations inside the crust, but the data exhibit a large degree of scatter and suffer from poor counts (Figure III.8 B). The presence in MRF2-3R of a pronounced ^{232}Th maximum at 0.2 MA, within the 0.1-0.3 Ma interval cited for the aeolian maximum, argues in favor of the radiometric dating performed on this crust.

4. Discussion

4.1 Genesis of oxyhydroxides

The composition of a ferromanganese oxyhydroxide is ultimately determined by the relative amounts of metals available in the environment in which it forms. There are three distinct sources from which metals may be incorporated into ferromanganese nodules and crusts: hydrogenetic, diagenetic, and hydrothermal. These sources are not mutually exclusive, but often act in concert to supply metals to the ferromanganese oxyhydroxides.

Hydrogenetic accumulation involves the direct precipitation of metal oxides derived from the water column onto a ferromanganese crust or nodule. Hydrogenetic precipitation is the most common formation mechanism for ferromanganese crusts from open oceans, in areas with low sedimentation rates and little hydrothermal activity (e.g. central Pacific seamounts). Hydrogenetic ferromanganese oxides include crusts growing

on exposed rock on the flanks of seamounts and on inactive midocean ridges, and nodules which form on the tops of seamounts. Often only the top portion of such nodules, which is not in contact with sediment, bears a hydrogenetic signature. Hydrogenetic ferromanganese crusts are generally the preferred ferromanganese oxide phase for use in studies of the paleochemistry of seawater.

Hydrothermal sources yield ferromanganese oxyhydroxides which are either highly enriched in Fe or in Mn, and which are generally depleted in trace elements (Cronan, 1997). Hydrothermal ferromanganese deposits vary widely in form and composition depending on the distance from and the type of vent system. They may occur as thin crusts on exposed rocks, massive pavements, stratabound deposits buried within hydrothermal sediments, or portions of actual vent structures. As hydrothermal fluids propagate farther from vent sites and mix with ambient seawater, the resulting precipitates begin to more closely resemble hydrogenetic crusts (Hein et al., 1997). The hydrothermal character of mixed deposits can be traced for many tens of kilometers from a vent site (Ibid.).

Diagenetic ferromanganese deposits receive their metal supply from sediment pore waters where remobilization due to redox processes occurs. Diagenetic deposits are generally limited to nodules lying on or within sediment. Diagenetic sources can be further broken down into oxic and suboxic types (Dymond et al., 1984), depending on redox conditions within the underlying sediments. Oxic diagenetic accretion depends

upon remobilization of transition metals by diagenetic processes within oxic sediments, whereas suboxic diagenetic accumulation relies upon oxidizing organic carbon using Mn^{4+}, thus mobilizing Mn^{2+} (Ibid.). Oxic diagenetic manganese oxides are enriched in Mn and in other transition elements. Suboxic diagenetic manganese oxides are very enriched in Mn and may be depleted in other transition elements (Ibid.).

It should be stressed that the overwhelming majority of inter-elemental relationships presented in the literature are based on datasets composed of bulk crusts and nodules, from large numbers of samples recovered from regions with specific hydro- and geographic characteristics (e.g. crusts from Central Pacific seamounts, nodules from deep abyssal plains, etc.). Therefore, one must consider the fact that proxies derived from such broad relationships may or may not apply to microscale measurements taken from layers within single crusts or nodules from other environments.

4.2 Mineralogy

Ferromanganese oxyhydroxides generally exist as admixtures of different iron- and manganese-rich mineral phases. Depending on environmental factors such as redox conditions in the water column, Fe and Mn form mixed colloids which, in turn, scavenge other metals from seawater. As a result, there are a number of mineral phases found in manganese nodules and crusts, including: 10Å-manganates (also known as todorokite, Mn-rich), δ-MnO_2 (also known as vernadite, Fe-rich), and X-ray amorphous Fe

oxyhydroxides, plus a number of other nonmetallic phases such as carbonate fluorapatite, barite, and zeolites (Hein et al., 1992; Koschinsky and Halbach, 1995; Lei and Boström, 1995; Koschinsky et al., 1997).

Separate mineral phases do not necessarily occur in distinct bands or zones within a crust, but may be intergrown, complicating mineralogical determinations (Lei and Boström, 1995). Post-depositional changes in crust or nodule mineralogy may occur as a result of diagenesis (Hein et al., 1992; Koschinsky et al., 1997). In addition, mineralogy may change after samples are collected and dried (Lei and Boström, 1995). Whether mineralogy determines elemental composition or vice versa has been the source of some debate. Mineralogical determinations were not included as part of this study.

4.3 Growth rates

Differences in the growth rates of different types of manganese oxyhydroxides can help elucidate the ultimate source of metals to a crust or nodule. Hydrogenetic precipitates generally form slowly, with growth rates ranging from 0.5 - 15 mm/Ma (Hein et al., 1997). Such slow growth promotes enrichment with trace elements, as it allows a longer time for metal oxides at the growth surface to scavenge trace metals from the surrounding seawater. Hein et al. (1997) reports that growth is slowest where the oxygen minimum zone intersects the seafloor, where Mn is most soluble.

Hydrothermal deposits are the fastest-growing form of ferromanganese oxyhydroxides, with growth rates ranging from 20 - 100 mm/Ma for mixed hydrothermal/hydrogenetic crusts to as fast as 10^3 - 10^5 mm/Ma for stratabound deposits (Hein et al., 1997).

Diagenetic deposits generally grow more rapidly than hydrogenetic deposits due to higher fluxes of Mn from sediments than from the water column. Dymond et al. (1984) report faster growth rates for suboxic diagenesis, ranging from 168 - 200 mm/Ma, than for oxic diagenesis, ranging from 12 - 50 mm/Ma. However, growth via suboxic diagenesis tends to be of an episodic nature, following periods of high productivity which result in a pulse of organic carbon flux to the sediments, followed by increased remobilization of reduced Mn (Ibid.).

Growth rates calculated for individual Mendocino samples tend to agree reasonably for individual samples (table III.3), given the limitations of and differences between the techniques used (i.e. comparing empirical versus radioisotopic determinations). ^{10}Be data are of reasonable quality ($\pm$5.5% error), and this radionuclide has a much longer half-life than ^{232}Th, therefore it seems to be the best choice for deriving growth rates.

The growth rates derived for crusts MRF2-3R and MRF6-12R indicate a hydrogenetic origin (table III.3). Their 6.9 and 4.6 mm/Ma growth rates, respectively,

fall well within the range of 0.5-15 mm/Ma range specified by Hein et al. (1997) as typical for hydrogenetic crusts. Deeper within the crust strata, however, the growth rates increase—MRF2-3R's nearly doubles to 14.3 mm/Ma, and MRF6-12R's more than triples to 18.9 mm/Ma. While these values approach or exceed the limit set by Hein et al. (1997) for hydrothermal crusts, they are slower than growth rates reported for many diagenetic (Dymond et al., 1984) or hydrothermal deposits (Hein et al., 1997). The higher growth rates in the deeper strata of these crusts may be due to some degree of hydrothermal influence early in their growth history, possibly from a considerable distance away (there is no appreciable local hydrothermal activity on the MFZ). The Gorda Ridge, to the north of the Mendocino fracture zone, could have served as such a source. Growth rates determined by ^{10}Be techniques project to 5.5 My for MRF2-3R and 2.4 My for MRF6-12R at the base of the crust (initiation of formation). A comparison with magnetic anomalies from the Gorda Plate shows that these crusts were generally to the south of the Gorda Ridge when they began growing (Figure III.9). Since currents near the study area are predominantly south-southeastward flowing (Pillsbury et al., 1982; Figure III.10), the transition to slower growth may have occurred as these deposits propagated westward with the spreading plate, moving out of the range of hydrothermal influence. Such westward propagation also would have moved the samples down a significant productivity gradient from the eastern boundary current towards the gyre, which would also result in reduced growth rates.

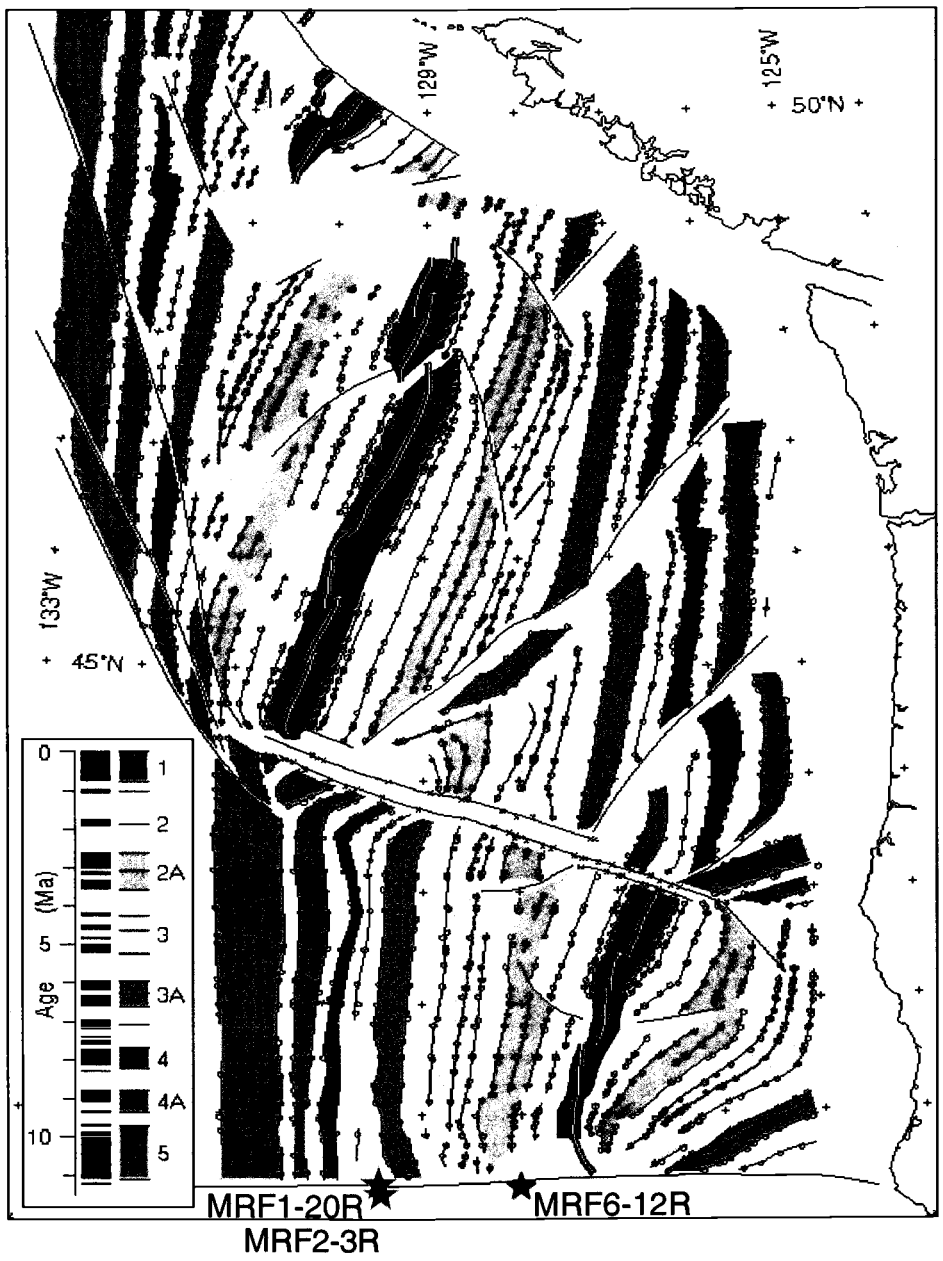

Figure III.9. Magnetic anomaly reconstruction of the region to the north of the MFZ, including the Gorda Ridge and Juan de Fuca spreading centers. Stars indicate manganese nodule and crust sample locations. Map from Wilson, D. S. (1993), courtesy of Ridge Multibeam Syntesis Project WWW page.

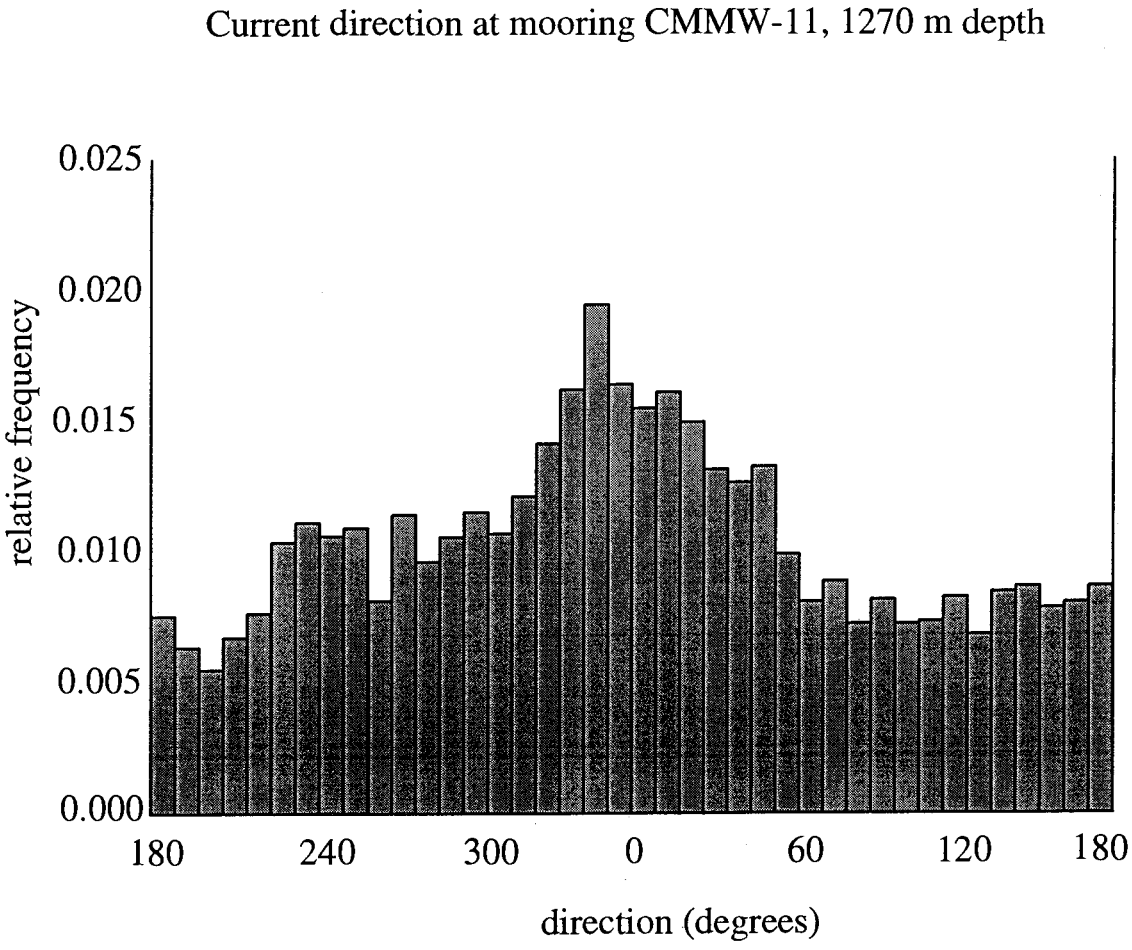

Figure III.10. Current direction at mooring CMMW-11; 39.493°N, 127.685°W, 1270 m depth; from Sept. 22, 1982 - Aug. 16, 1984. Data from http://kepler.oce.orst.edu/jpl/deep/norpac/llwodp_w/llwodp_w.htm

4.4 Major element interrelationships

Bulk compositions for the Mendocino samples are presented in table III.4. Inter-elemental correlation matrices for LA ICP-MS, ICP-AES, and EPMA are presented in Appendix B. Ternary relationships between Fe, Mn, and Co+Ni+Cu were examined (after Bonatti et al., 1971) to illustrate general composition of Mendocino manganese oxides relative to hydrogenetic, hydrothermal, and diagenetic endmembers (see section 4.5.2).

The relationship between Mn and Fe reflects the dominant source of metals to a ferromanganese deposit. Cronan (1997b) reports that seawater supplies Mn and Fe to the hydrogenous endmember in a ratio approximately equal to 1. Hein et al. (1997) present a large dataset of bulk composition of Pacific crusts and nodules in which the hydrogenetic examples exhibit Mn/Fe averaging 1.4, although those near continental margins had lower Mn/Fe ratios ranging from 0.8 – 1.0, these slightly lower values likely due to terrestrial sources of Fe. From the reported values one can conclude that the Mn/Fe ratio averages approximately 1 during hydrogenetic precipitation.

Hydrothermal precipitates display a wide spectrum of Fe and Mn values. Hein et al. (1997) reports Mn/Fe ratios ranging from 4.2×10^{-5} for hydrothermal seamount ironstones to 1000 for hydrothermal stratabound manganese oxide deposits from active arcs.

East Pacific Crusts (Hein et al, 1997)				Pacific seamount crusts (Usui and Someya, 1997)					Pacific marginal seamount crusts (Usui and Someya, 1997)			
				average	maximum	minimum			average	maximum	minimum	
Mn/Fe	0.79											
Mn	16.9	wt%		22.1	45.9	7.20	wt%		16.6	40	6.41	wt%
Fe	21.5	wt%		15.1	36.0	2.88	wt%		18.0	32.2	8.55	wt%
Al	2.1	wt%		1.01	5.30	0.11	wt%		1.82	4.6	0.48	wt%
Ti	0.6	wt%		0.77	2.08	0.04	wt%		1.47	3.84	0.21	wt%
P	0.42	wt%										
Ni	3258	ppm		5403	14400	340	ppm		3277	10000	230	ppm
Cu	756	ppm		1075	5600	50	ppm		847	5382	130	ppm
Co	3118	ppm		6372	14200	300	ppm		2905	10218	131	ppm
Zn	694	ppm		680	1500	294	ppm		606	1480	312	ppm
Mo	382	ppm		455	1530	3	ppm		297	643	80	ppm
Ce	1167	ppm										
V	626	ppm		515	1019	93	ppm		566	1062	284	ppm
Pb	1373	ppm		1777	3200	150	ppm		1643	3510	94	ppm

Table III.4. Comparison of published chemical compositions with those of Mendocino Ridge manganese deposits.

MRF1-20R ("cannonball nodule")					MRF6-12R (crust on cobblestone)					MRF2-3R (massive crust)			
lat.	40.3555 N				lat.	40.3727 N				lat.	40.3288 N		
long.	129.4238 W				long.	128.1375 W				long.	129.5365 W		
depth	1760 m				depth	2053 m				depth	2195 m		
			method					method					method
Mn/Fe	3.0		AES		Mn/Fe	1.0		AES		Mn/Fe	0.62		AES
Mn	34.6	wt%	AES		Mn	18.2	wt%	AES		Mn	12.6	wt%	AES
Fe	11.6	wt%	AES		Fe	17.9	wt%	AES		Fe	20.2	wt%	AES
Al	1.2	wt%	AES		Al	1.7	wt%	AES		Al	2.2	wt%	AES
Ti	0.2803	wt%	LA ICP-MS		Ti	0.3186	wt%	LA ICP-MS		Ti	0.20	wt%	LA ICP-MS
P	0.44	wt%	LA ICP-MS		P	0.4099	wt%	LA ICP-MS		P	0.28	wt%	LA ICP-MS
Ni	13723	ppm	AES		Ni	3586	ppm	AES		Ni	2439	ppm	AES
Cu	501	ppm	AES		Cu	534	ppm	AES		Cu	479	ppm	AES
Co	2961	ppm	AES		Co	2277	ppm	AES		Co	2052	ppm	AES
Zn	1201	ppm	AES		Zn	578	ppm	AES		Zn	544	ppm	AES
Mo	622	ppm	LA ICP-MS		Mo	517	ppm	LA ICP-MS		Mo	264	ppm	LA ICP-MS
Ce	440	ppm	LA ICP-MS		Ce	428	ppm	LA ICP-MS		Ce	274	ppm	LA ICP-MS
V	576	ppm	LA ICP-MS		V	568	ppm	LA ICP-MS		V	503	ppm	LA ICP-MS
Pb	713	ppm	LA ICP-MS		Pb	789	ppm	LA ICP-MS		Pb	509	ppm	LA ICP-MS

Table III.4. (continued) Comparison of published chemical compositions with those of Mendocino Ridge manganese deposits.

Diagenetic precipitates exhibit Mn/Fe ratios greater than 1, as a result of enhanced supply of Mn from redox processes within underlying sediments (Cronan, 1997). Nodules formed on oxic sediments underlain by reducing sediments (i.e. suboxic diagenesis [Dymond et al., 1984]) are very enriched in Mn, often 30 - 40% by weight (Cronan, 1997), with Mn/Fe values ranging from 20 - 70. Oxic diagenesis also results in Mn enrichment, but to a lesser degree--typical Mn concentrations for such a deposit range from 25 - 30% by weight (Cronan, 1997), with Mn/Fe ratios ranging from 5 - 10 (Dymond et al., 1984). Hlawatsch and Suess (1993) report an increasing trend in Mn/Fe ratios in the outer layers (dated from 1880 AD $\pm$ 40 years) of nodules recovered from the Baltic Sea; this trend is suggested to be related to the historic decline in the Baltic Sea's oxygen content brought about by industrialization.

Halbach and Puteanus (1984) note a general decrease in the Mn/Fe ratio with increasing depth in bulk samples from Central Pacific seamounts. The authors reasoned that the Mn/Fe ratio should be the highest immediately beneath the oxygen minimum zone (OMZ), where Mn is much more abundant than Fe.

It is not possible to analyze Mn using LA ICP-MS, as concentrations of this monoisotopic element in manganese oxides are too high for the detector. Thus, ICP-AES was employed for the determination of Mn/Fe ratios in the suite of Mendocino samples.

Crust MRF2-3R's Mn/Fe ratio ranges from 0.47 to 0.77 (Figure III.11), which agrees well with a reported average value of 0.79 for hydrogenetic crusts from the East Pacific (Hein et al., 1997). The Mn/Fe ratio exhibits a maximum at 3 Ma, and a minimum at 0.2 Ma. The minor amount of variation in this ratio suggests that MRF2-3R has accreted via hydrogenous means throughout its growth history. There is a general trend towards decreasing Mn/Fe over time (Figure III.11), with the lowest values in recent times—an intriguing relationship which agrees with Halbach and Puteanus' (1984) observation of decreasing Mn/Fe values with increasing depth, and which might be related to the subsidence of the Mendocino Ridge.

MRF6-12R exhibits Mn/Fe ratio values averaging 1.0, although one subsample at 1.3 Ma exhibits a Mn/Fe ratio of 2 (Figure III.12). This doubling of the average Mn/Fe ratio likely indicates a major shift in the redox conditions at that time. With the exception of the aforementioned interval, the Mn/Fe proxy shows that MRF6-12R has accreted by hydrogenetic mechanisms.

MRF1-20R is anomalous among the suite of samples in that it displays the highest Mn/Fe ratio, reaching a maximum value of approximately 15 at 2.2Ma (Figure III.13). A Mn/Fe ratio of this magnitude implies diagenetic or hydrothermal influence. The elevated Mn/Fe ratio is not sustained, however, as Mn/Fe ranges from 2 –3 from 2Ma to present, suggesting hydrogenous accumulation for this nodule during this period.

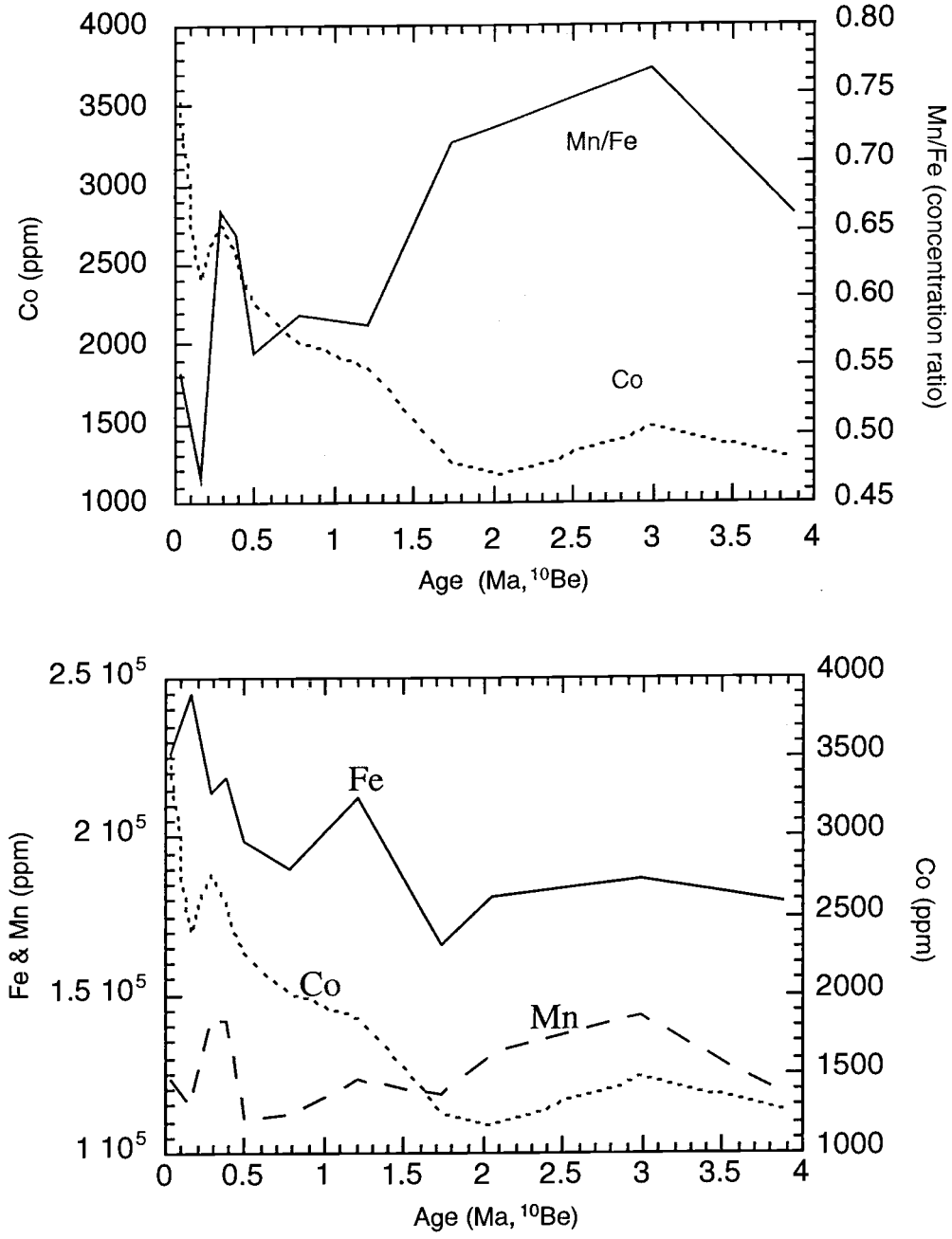

Figure III.11. Crust MRF2-3R age profiles showing relationship between Co, Mn, and Fe concentrations and Mn/Fe ratio. ICP-AES data. Age model integrates inner and outer ^{10}Be growth rates.

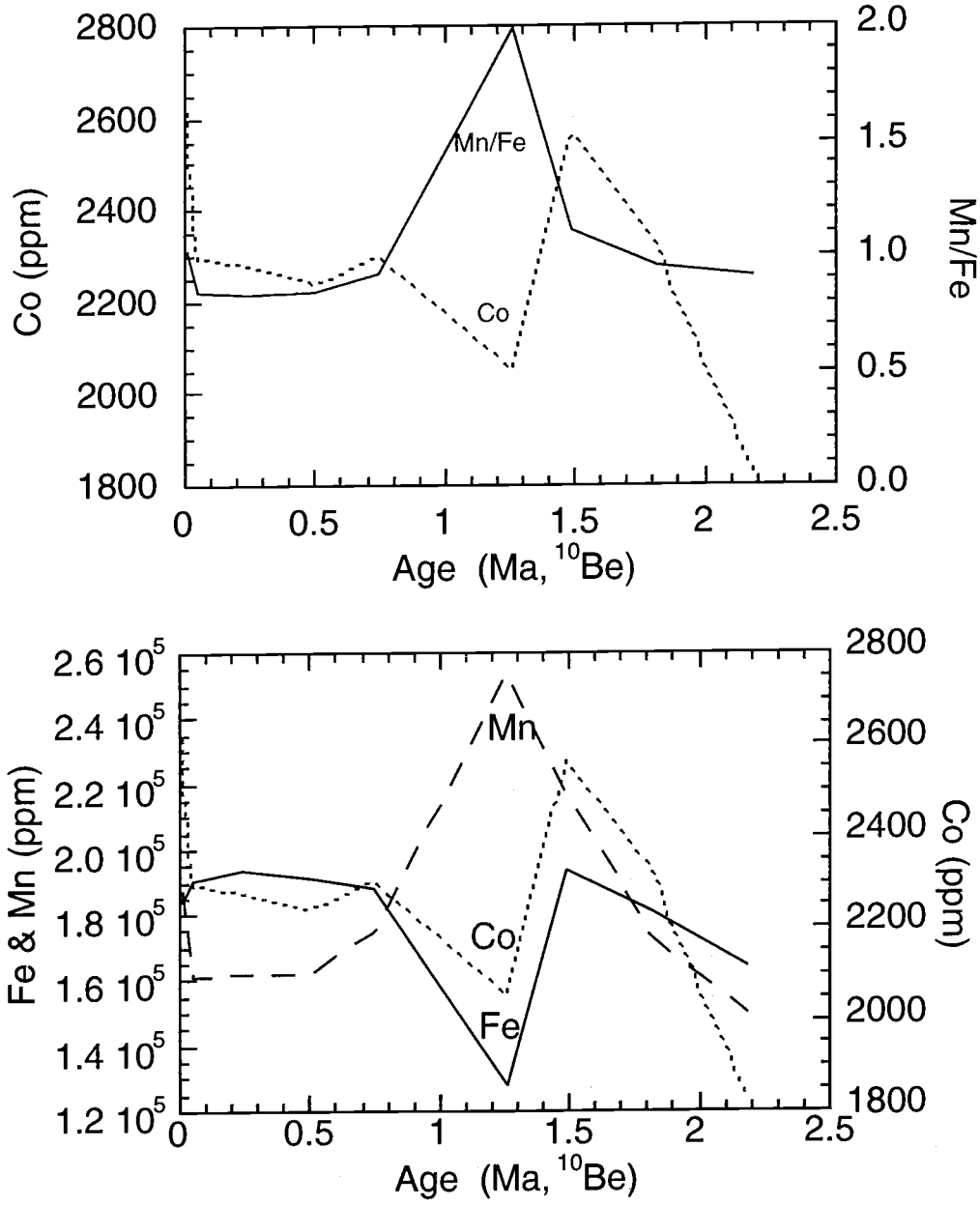

Figure III.12. Crust MRF6-12R age profiles showing relationship between Co, Mn, and Fe concentrations and Mn/Fe ratio. ICP-AES data. Age model integrates inner and outer ^{10}Be growth rates.

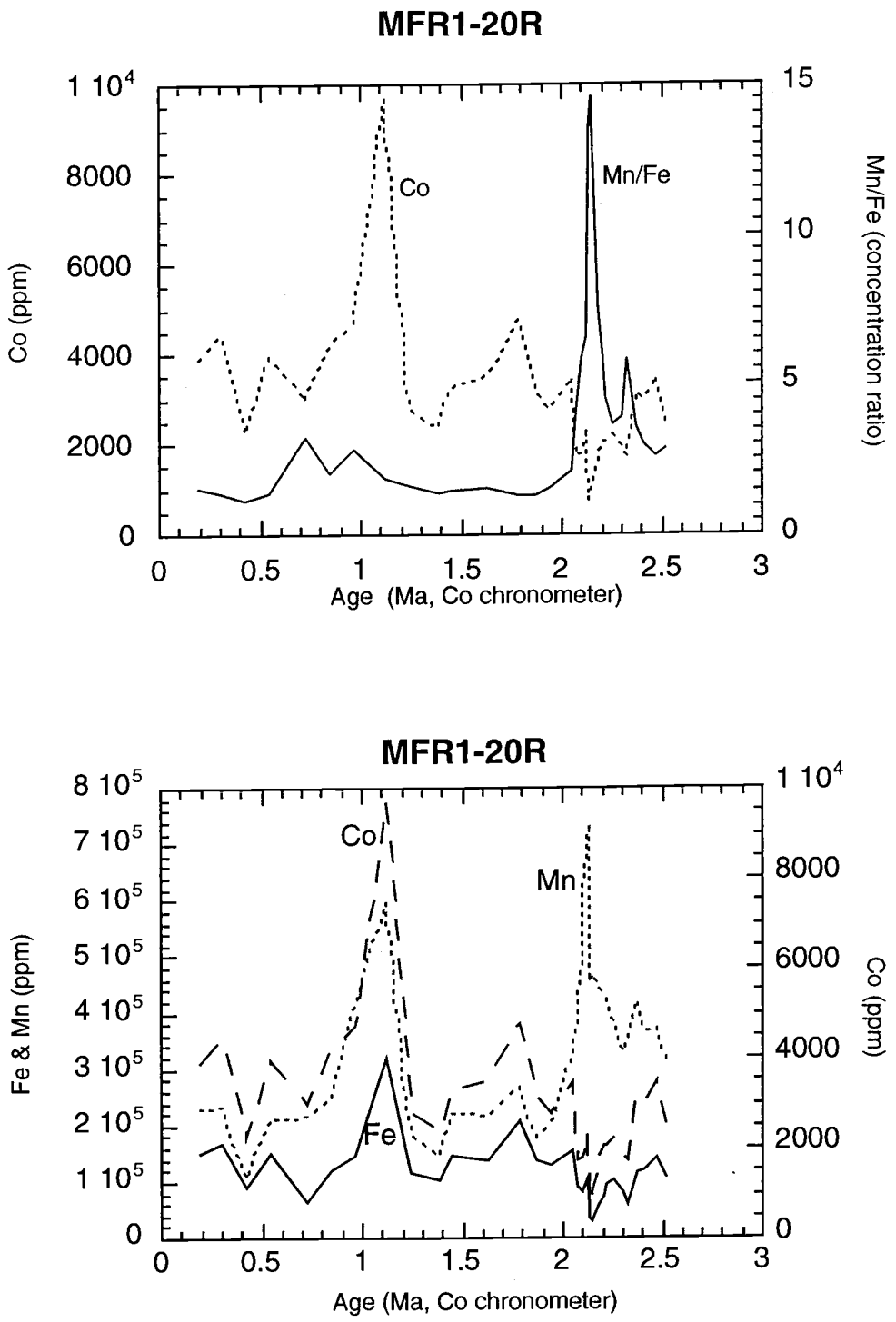

Figure III.13. Nodule MRF1-20R age profiles showing relationship between Co, Mn, and Fe concentrations and Mn/Fe ratio. ICP-AES data.

However, a Mn/Fe value of 2-3 is high relative to the other two samples and may imply some degree of diagenetic or hydrothermal influence.

4.5 Trace element interrelationships

A general characteristic of hydrogenetic precipitates is substantial enrichment in trace metals. Cobalt is often highly enriched, with an average concentration of 1.2% for crusts from the Pacific (Takematsu et al., 1989), although lower concentrations (hundreds of ppm) are commonly reported (Ibid.; Hein, 1997; Cronan, 1977; Usui and Someya, 1997). The majority of research performed on hydrogenetic crusts reports that Co associates with Mn phases. A negative correlation exists between Co and growth rate, also—slower growth rates allow more time for Mn oxides to remain in contact with ambient seawater, scavenging Co from solution (Takematsu et al., 1984). Zn, Ba, Mo, V, Pb, Sr, and Pt are also commonly enriched in hydrogenetic crusts (Hein et al., 1997). In addition, the rare earth elements (REEs) are enriched in deposits with hydrogenetic input (including mixed hydrogenetic/diagenetic types), especially Ce. As a result of preferential enrichment of Ce over its neighboring REEs, hydrogenetic crusts typically have strong positive Ce anomalies (Ibid.).

Hydrothermal deposits are generally depleted in trace elements (Cronan, 1997), but trace metal contents may vary depending on the characteristics and proximity of the vent system. Controlling factors include the amount of leaching of rocks and sediments

by hydrothermal fluids (water/rock ratio), the composition of rocks or sediments leached, the amount of mixing with seawater, the temperature, and the degree of precipitation of sulfides all determine the composition of a hydrothermal deposit (Hein et al., 1997). Hydrothermal manganese deposits generally are enriched in Zn, Mo, Cd, Ni, Cr, and Li, while hydrothermal iron deposits are usually very enriched in Cr, and contain elevated concentrations of As, V, and P scavenged from seawater (Ibid.). REE contents are usually low, and hydrothermal deposits generally display negative Ce anomalies (Ibid.). Enrichment of middle REEs has been reported for hydrothermal deposits from the Indian Ocean (Nath et al., 1997).

Diagenetic ferromanganese deposits display complex trace element distributions, often with drastically different compositions on the top and bottom sides. Nodules influenced by oxic diagenesis generally display enrichments in Ni (1.0 – 1.5%), Cu (1.0 – 1.5%), but are lower in Co (0.1 – 0.25%) when compared to hydrogenetic deposits (Cronan, 1997). There are many reports of positive correlations between Co and Fe for "early diagenetic" (i.e. oxic diagenetic) and mixed nodules recovered from the sediment-water interface or upper sediment layer of ocean basins (Halbach, 1982; Takematsu et al., 1989; Cronan, 1977). In addition, Halbach (1982) reports a negative correlation between Co and Mn in such deposits, in contrast to the positive correlation seen between these two elements in hydrogenetic deposits. Suboxic diagenetic nodules are typically depleted in transition metals besides Mn and Zn.

Bulk compositions of Mendocino crusts MRF2-3R and MRF6-12R agree reasonably well with published average values for Eastern Pacific hydrogenetic crusts (table III.4), yet there are some compositional differences. MRF2-3R is depleted, with respect to published values (Hein et al., 1997), in Ti, P, Ce, and Pb, and slightly depleted in the manganophile elements Ni, Cu, Zn, and Co. MRF6-12R is depleted in Ti, Ce, and Pb, slightly depleted in Al, Cu, Co, and Zn, enriched in Mo, and slightly enriched in Ni. MRF1-20R's major element bulk chemistry varies significantly from published values for hydrogenetic crusts from the region, with substantial Mn enrichment and Fe depletion, yet its values lie within limits for western Pacific hydrogenetic crusts reported by Usui and Someya (1997). Al, Ti, Ce, and Pb are also depleted in MRF1-20R, while Ni, Zn, and Mo are enriched. All of these elements associate with the Mn oxide phase, which is the predominant major element in this nodule. Although MRF1-20R is markedly different from the other two crusts in the Mendocino sample suite, it is within published extrema for hydrogenetic crust values.

4.5.1 *Cobalt*

Although cobalt is considered a valuable metal within ferromanganese crusts and is important in the biological utilization of vitamin B-12, little is known about its distribution in the oceans. Much early work focused on analyzing Co and other trace element in seawater was hampered by contamination (Knauer et al., 1982). Cobalt's

distribution in seawater is generally similar to that of manganese, enriched at the surface and depleted in deep water (Spencer et al., 1970; Klinkhammer and Bender, 1980; Landing and Bruland, 1980; Knauer et al., 1982). Halbach and Puteanus (1984) hypothesized that Co fluxes to shallow and deep water ferromanganese crusts are the same, and that variations in Co content are due to dilution by more abundant Mn and Fe phases. The same authors report that crusts with the highest Co contents come from just beneath the OMZ, suggesting that Co is mobilized along with Mn by redox processes within the OMZ.

Cobalt is highly particle-reactive and is readily scavenged by vernadite (δ-MnO_2), the major manganese mineral in hydrogenetic crusts (Frank et al., 1999). Cobalt, primarily present in seawater as Co^{2+} (Branica et al., 1981), is oxidized to Co^{3+} when scavenged by δ-MnO_2 (Halbach and Puteanus, 1984; Frank et al., 1999). Although there is much controversy over the relation of cobalt to iron and manganese, cobalt is reported to correlate positively with manganese and negatively with iron in vernadite, with the opposite correlations in 10 Å-manganate (Lei and Boström, 1995).

Average bulk Co contents among the group of Mendocino samples are remarkably similar. The average Co concentration of MRF2-3R is 2052 ppm, MRF6-12R is 2277 ppm, and MRF1-20R is 2961 ppm. These values are similar to the 3118 ppm average reported for East Pacific crusts (Hein et al., 1997).

Co concentration profiles through individual samples exhibit marked variation, by as much as a factor of 5 in nodule MRF1-20R. In this sample, Co displays a generally inverse relationship with Mn/Fe, exhibiting a maximum of 0.97% at 1.1Ma (Figure III.13). The correlation of Co with Mn is typical for hydrogenetic deposits, while Co correlates with Fe in diagenetic nodules. A minimum Co concentration of 780 ppm occurs at 2.1 Ma, which coincides with the Mn/Fe maximum in this sample. During the interval from 2.5 to 2.0 a, Co correlates with Fe (Figure III.13), yet from 2.0 Ma to present, Co concentrations mirror those of both Fe and Mn.

Crust MRF2-3R's Co concentration varies by almost a factor of 3 over its growth history. MRF2-3R exhibits a Co maximum of 3500 ppm at the crust surface (Figure III.11), in agreement with other reports that Co concentrations are highest at the surface of slowly accumulating hydrogenetic crusts (Halbach and Puteanus, 1984; McMurtry et al., 1994). The Co minimum is 1200 ppm at 2 Ma. Co concentrations are generally inversely related to Mn/Fe. The Co profile bears most resemblance to the Fe concentration profile, although over the last 0.2 Ma the Fe concentration drops, while the Co and Mn concentrations both increase. This likely indicates that Co is incorporated in both Fe oxyhydroxide and Mn oxide phases, with the balance shifting based on small changes in the ambient redox conditions or relative availability of the two major metals.

Crust MRF6-12R exhibits approximately a factor of 1.5 variation in its Co concentration, the lowest of the suite of Mendocino samples (Figure III.12). There are

two Co maxima, one at 1.5 Ma, and one at the surface (typical of hydrogenetic crusts). Both maxima are approximately 2600 ppm. It is interesting to note that MRF1-20R exhibits a Co maximum at a similar time of 1.1 Ma. Given that MRF6-12R's ages were calculated using 10Be, and MRF1-20R's using Co chronometry, these peaks may be genetically related. However, examination of major element concentrations reveals that Fe and Mn decrease dramatically during this interval in MRF6-12R, while Fe and Mn increase dramatically in MRF1-20R, revealing that two different processes are likely responsible for these concurrent Co peaks.

Inter-elemental correlation matrices (see Appendix B) for LA ICP-MS and ICP-AES data reveal that Co correlates strongly with Fe in all Mendocino samples, with the exception of the high magnification LA ICP-MS analyses of crust MRF2-3R. Co and Mn show no correlation. ICP-AES data for MRF2-3R, however, reveal a strong (r=0.891) correlation between Fe and Co. The lack of correlation (r=0.471) between Fe and Co in the high resolution analysis may be due to fine scale differences in mineralogy. For example, the fine scale resolution afforded by LA ICP-MS may allow the resolution of elemental variations between thin Mn-rich and Fe-rich layers that are impossible to sample individually by manual scraping methods. It is not the result of a poor run, as two different runs of this crust on two different days yield very similar results. The strong positive correlation between Fe and Co is contrary to other reports for hydrogenetic

crusts, which describe no correlation between Co and Fe, and a strong positive correlation between Mn and Co.

4.5.2 *Ternary relationships*

Ternary diagrams of Mendocino samples, adapted from Bonatti et al. (1972) elucidate sources of metal fluxes to these Mn oxides (Figure III.14). All three Mendocino samples lie within the field which describes hydrogenetic crusts, however, all show signs of influence from additional sources. MRF6-12R plots within the hydrogenetic field, yet it lies near the lower limits of this field, implying some degree of hydrothermal influence. MRF2-3R plots mostly within the hydrogenetic field, but some strata plot slightly outside of the hydrogenetic range, immediately adjacent to the field defining hydrothermal oxides. MRF1-20R displays an intriguing relationship: its strata exhibit a linear distribution on the ternary diagram, with the deepest strata showing hydrothermal plus diagenetic influence, and the strata nearer the surface being hydrogenetic. This suggests a progressive change in formation conditions over the growth history of this nodule. Reconstructing plate motion based on magnetic anomalies (Figure III.9) shows that this nodule began formation to the south of the Gorda Ridge. The portion of the ridge to the north of the MFZ is presently heavily covered with

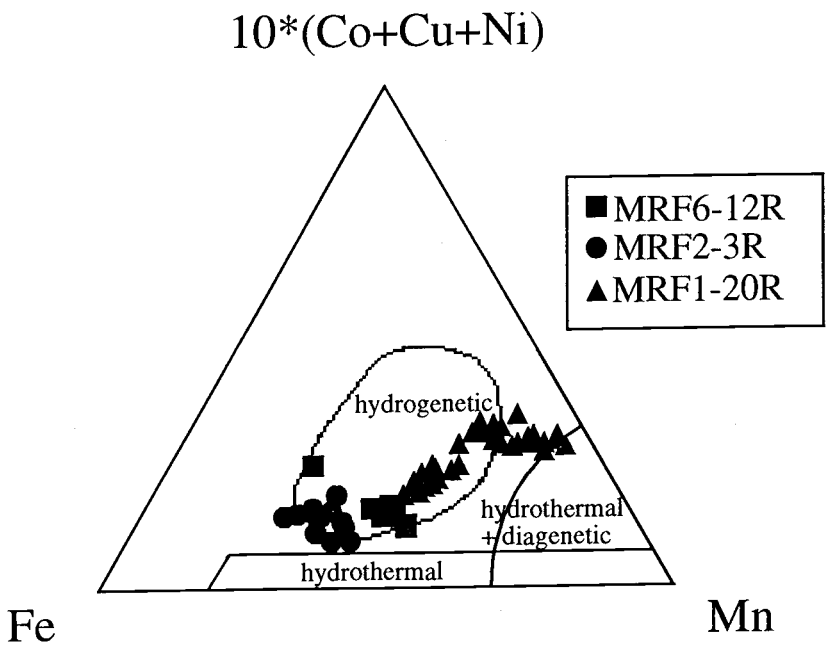

Figure III.14. Ternary diagram (after Bonatti et al., 1972) of Mendocino manganese oxides. Data are from ICP-AES analyses of crust and nodule scrapings. Samples are of hydrogenetic origin, yet with hydrothermal and (for nodule MRF1-20R) diagenetic influence. The trend visible in MRF1-20R from hydrothermal + diagenetic to hydrogenetic occurs over the course of its formation history.

sediment, which may explain the diagenetic signal, yet the basalt substrate at the site from which nodule was recovered is presently free of sediment.

4.5.3 *Rare Earth Elements*

The rare earth elements, also known as the lanthanides, comprise a group of fifteen elements ranging from lanthanum to lutetium. As a group, they are characterized by exceptionally coherent behavior in the natural environment, with the exceptions of cerium and europium, which may behave differently due to changes in their oxidation states. The REEs commonly exist in seawater in the 3^+ oxidation state. Due to the progressive filling of the 4f electron shell, REEs in solution exhibit slightly decreasing ionic radii with increasing atomic number. Seawater, when compared to composite values for North American shales, exhibits a pattern of heavy rare earth element (HREE) enrichment, which is ascribed as a result of electrostatic effects from ionic contraction of 3^+ REEs with increasing atomic number (Piepgras and Jacobsen, 1992). The smaller ionic radii of HREEs lead to stronger complexes which are more stable in seawater (de Baar et al., 1985), but conversely may also lead to stronger surface complexation interactions (Piepgras and Jacobsen, 1992). As a group, REEs exhibit fractional enrichment with depth; that is, at increasing depths, HREEs are substantially enriched

over LREEs (de Baar et al., 1985). This relationship bears potential for the elucidation of paleoenvironments of formation of manganese oxides.

LA ICP-MS analyses acquired in low magnification mode yielded sufficient counts for REE determinations. Concentrations were calculated and normalized to North American Shale Composite (NASC) values (Piper, 1974), and subsequently averaged over discrete intervals. NASC-normalized crust and nodule compositions were also examined with respect to calculated ages for fractionation, redox, and source proxies.

4.5.3.1 *REE Concentrations*

Substantial enrichments of REEs over seawater concentrations have been widely reported for manganese nodules and crusts (De Carlo, 1991). Individually, REEs in seawater generally exhibit increasing concentrations with increasing depth in the ocean (de Baar et al., 1985; Elderfield, 1988; Piepgras and Jacobsen, 1992). The similarity of their distributions to nutrient profiles has been noted, particularly to silicate (Elderfield, 1988). Others have ascribed REE distributions to scavenging by particles and subsequent desorption from these particles during dissolution processes at depth (de Baar et al., 1985; Elderfield, 1998; and Piepgras and Jacobsen, 1992). Biogenic particles, especially those coated with Mn oxides, have been implicated as major contributors in biogeochemical cycling of REEs (de Baar et al., 1985 and Elderfield, 1988).

The fact that REE concentrations and relative enrichments (i.e. HREE/LREE) in seawater change with depth offers the potential of a depth record in ferromanganese oxyhydroxides from the Mendocino Ridge. Since these oxides were likely formed while the ridge was undergoing subsidence, it stands to reason that there should be a record of increasing depth preserved in their REE contents. Changes in oceanic circulation due to the removal of the Mendocino Ridge as a barrier to the southward-flowing California current may also be reflected in changes in the Ce anomaly, as might periods of enhanced hydrothermal influence or high productivity.

REE concentrations in the Mendocino samples are enriched compared to values for many hydrogenetic crusts reported elsewhere in the literature (Baturin, 1987; Nath et al., 1992), but they are within extrema published for western Pacific hydrogenetic crusts (Usui and Someya, 1997). REE concentrations exceed published maxima for western Pacific marginal seamount crusts (Ibid.). As has been reported elsewhere (Nath et al., 1992; Nath et al., 1997; Addy, 1974), these ferromanganese oxyhydroxides exhibit notable middle REE enrichment (Figure III.15). All samples show prominent positive Gd and negative Tb anomalies. Hein et al. (1988) first reported Gd and Tb anomalies in a suite of crusts from the Marshall Islands, noting that these features are characteristic of seawater. Given the trend of increasing seawater concentrations of individual REEs with depth, one would expect REE contents within a crust or nodule to increase towards the sample surface, reflecting formation of successive layers in progressively deeper waters

Figure III.15. Nasc normalized REE concentrations averaged over discrete depth intervals in Mendocino manganese deposits. A) MRF1-20R, B) MRF6-12R, C) MRF2-3R.

Figure III.15.A.

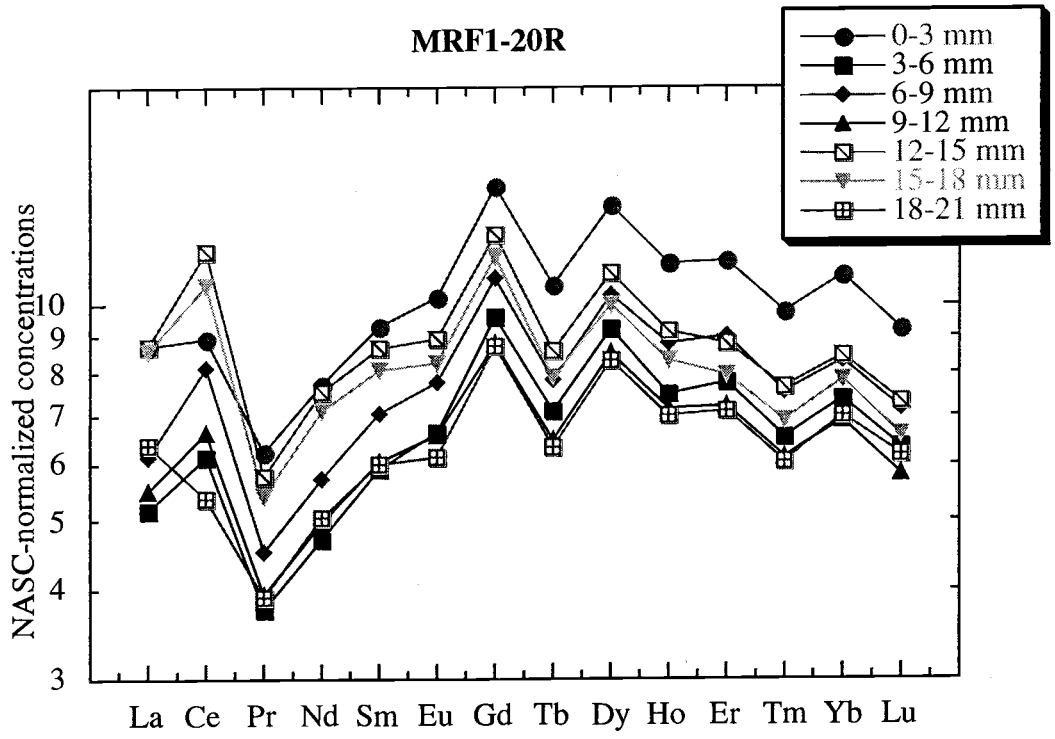

Figure III.15.B.

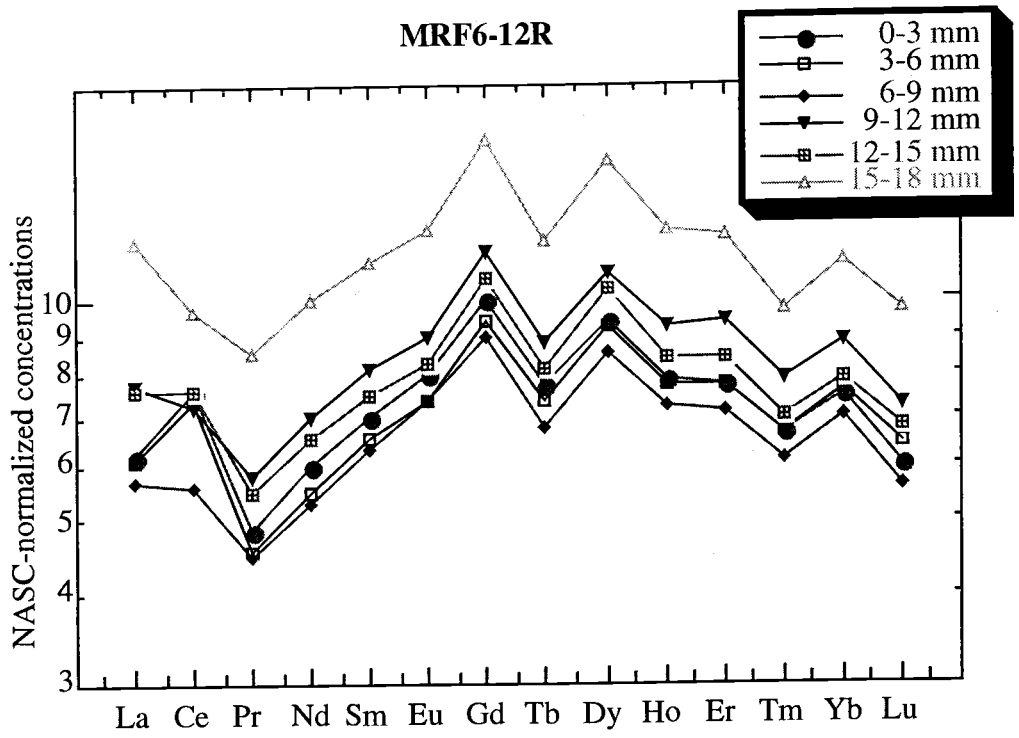

Figure III.15.C.

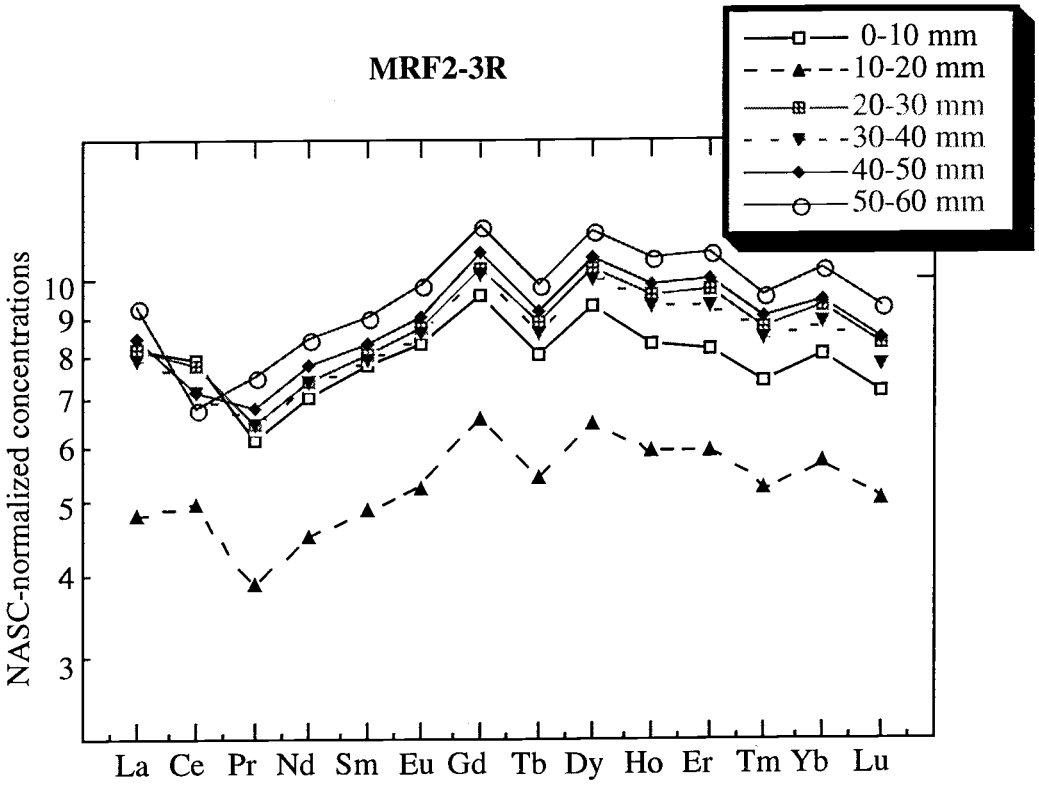

as the Mendocino Ridge subsided. This trend is only found, in a very general sense, in nodule MRF1-20R, in which the innermost layer (18-21 mm deep) exhibits minimum concentrations for many REEs and the outermost layer (0-3 mm) exhibits maximum concentrations for all REEs except La and Ce (Figure III.15A). The REE contents of the interposed layers, however, do not exhibit a similarly ordered distribution. Crusts MRF6-12R and MRF2-3R, with the exception of a few anomalous layers, show generally the opposite trend, exhibiting higher REE concentrations with increasing layer depth (Figures III.15 B and C).

4.5.3.2 *Fractionation*

In light of the trend of HREE enrichment/LREE depletion with increasing depth in seawater, one would expect nodules and crusts from the Mendocino Ridge to exhibit fractionation with HREEs favored near the surface layers and LREEs favored at depth. To examine fractionation relationships in the water column, data from Piepgras and Jacobsen (1992), were used to compare total REE and LREE/HREE proxies for north Pacific seawater. As the REE data presented are incomplete (several elements were not analyzed), it is not possible to compare all of the proxies used in the discussion of Mendocino manganese deposits that follows (specifically HREE/LREE, where HREE= Σ[Tb through Yb] and LREE = Σ[La + Pr through Gd]). Total REEs increase dramatically with depth (Figure III.16). Although there are gaps in the Lu data, La/Lu

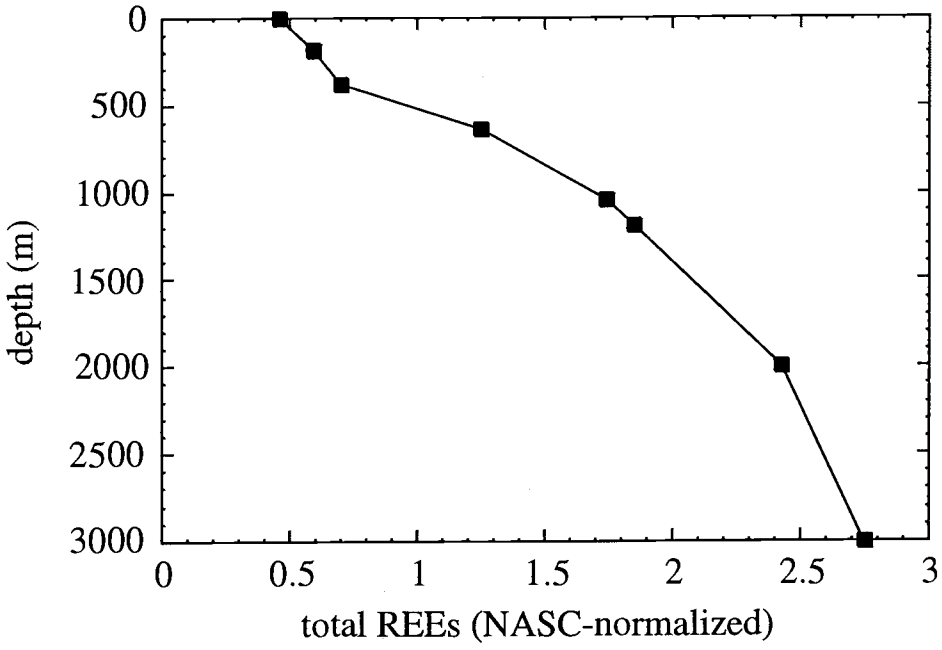

Figure III.16. Total NASC-normalized REEs versus depth in north Pacific seawater (data from Piepgras and Jacobsen, 1992). Sum REEs = La+Ce+Nd+Sm+Eu+Gd+Dy+Er+Yb (Lu data are not complete, and were not included).

exhibits a general decrease (albeit small in magnitude) between the depth of the OMZ (~800 m) and 2000 m (Figure III.17 A). La/Yb exhibits a similar trend, with a maximum at the depth of the OMZ, followed by a decline to 2000 m (Figure III.17 B). Yb/Sm, an index of HREE versus middle mass REE fractionation, exhibits a steady increase (i.e. increasing HREE enrichment) from the surface water until 1200 m (Figure III.18 A). La/Sm, an index of HREE versus middle mass REE fractionation, exhibits a steady increase from the surface to 1200 m depth (Figure III.18 B), which does not indicate enrichment of heavier, although middle mass, REEs relative to LREE with increasing water depth. It stands to reason that such trends in REE fractionation in the water column, although not of enormous magnitude, should be recorded in hydrogenetically precipitated crusts and nodules.

Nodule MRF1-20R exhibits these trends in a general sense. A plot of HREE(=Tb through Yb)/LREE(=La + Pr through Gd) versus age shows a relative increase in HREE from 4.3 Ma to 1.8 Ma (Figure III.16 A). However, there is a shift towards LREE from 1.8 Ma to present, and a shift from HREE rich to LREE rich from 5.8 Ma to 4.3 Ma. La/Lu, an alternate index of light/heavy REE enrichment, shows a general decrease (i.e. increased Lu) from about 4.5 Ma to present (Figure III.19 B). Sm/Yb (middle/heavy) exhibits a general increase from 4.5 Ma to present, corroborating the La/Lu trend (Figure III.19 C). La/Sm exhibits a slight decrease over the course of the nodule's growth

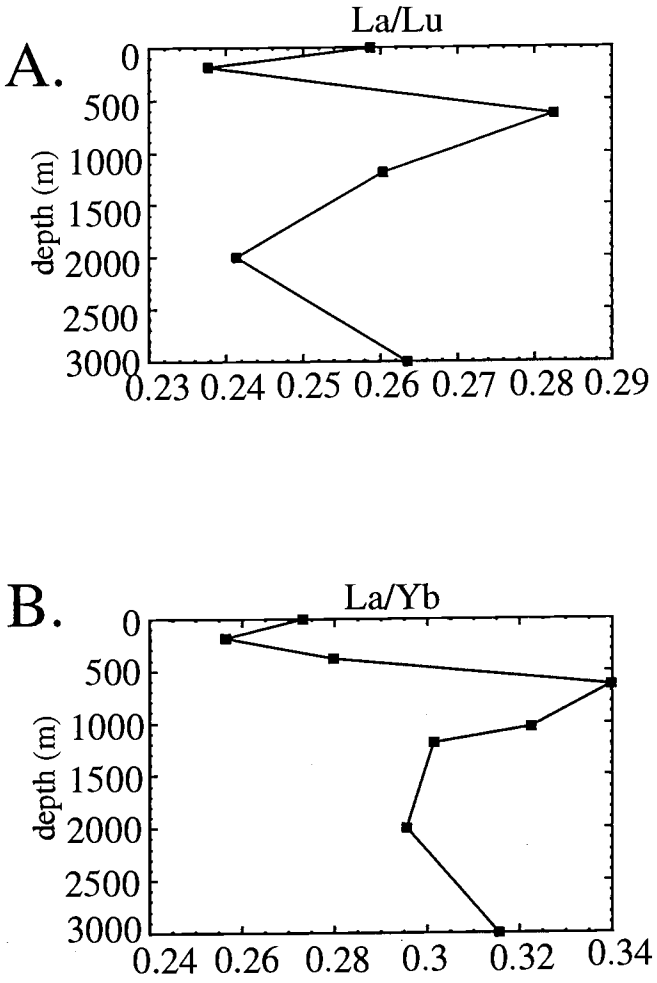

Figure III.17. REE fractionation proxies in north Pacific seawater (data from Piepgras and Jacobsen, 1992). A general trend exists of HREE enrichment relative to LREE with depth between the oxygen minimum zone (~800m) and 2000m, as evidenced by decreasing La/Lu and La/Yb ratios over this interval.

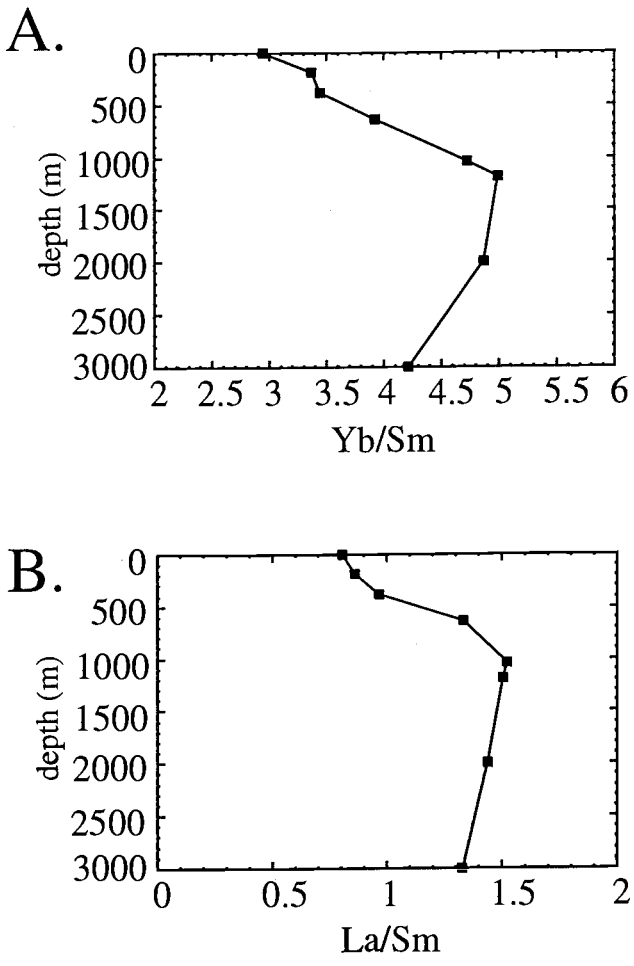

Figure III.18. REE fractionation proxies in north Pacific seawater (data from Piepgras and Jacobsen, 1992). Yb/Sm increases from the surface to 1200m depth, indicating progressive HREE enrichment between these depths. La/Sm increases in the upper 1000m of the water column, which does not uphold reports of HREE/LREE enrichment with increasing depth.

Figure III.19. REE fractionation indexes versus age, Mendocino nodule MRF1-20R. A) Heavy/light REEs, B) La/Lu, C) La/Sm and Yb/Sm, and D) total REEs (ppm).

Figure III.19.A.

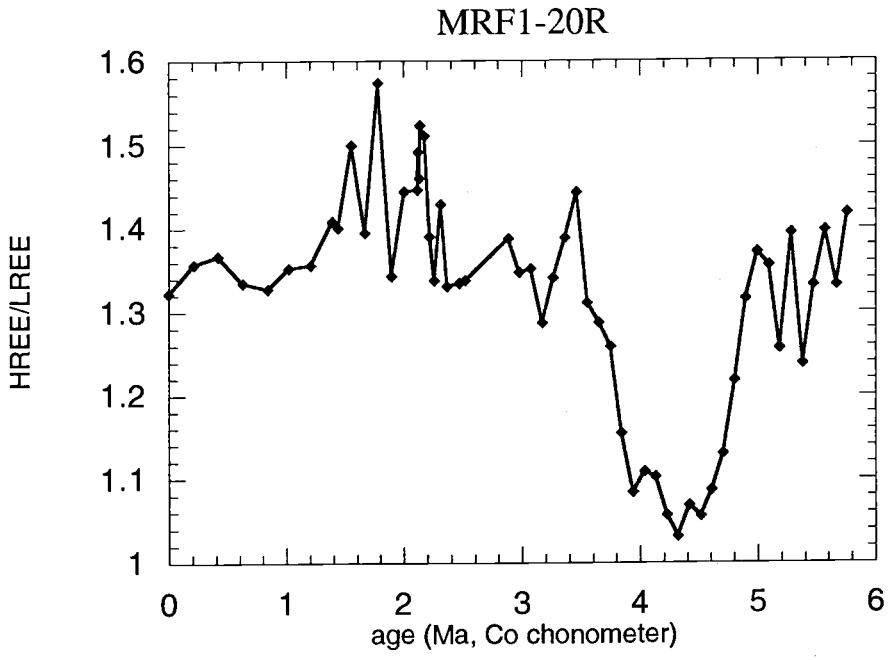

Figure III.19.B.

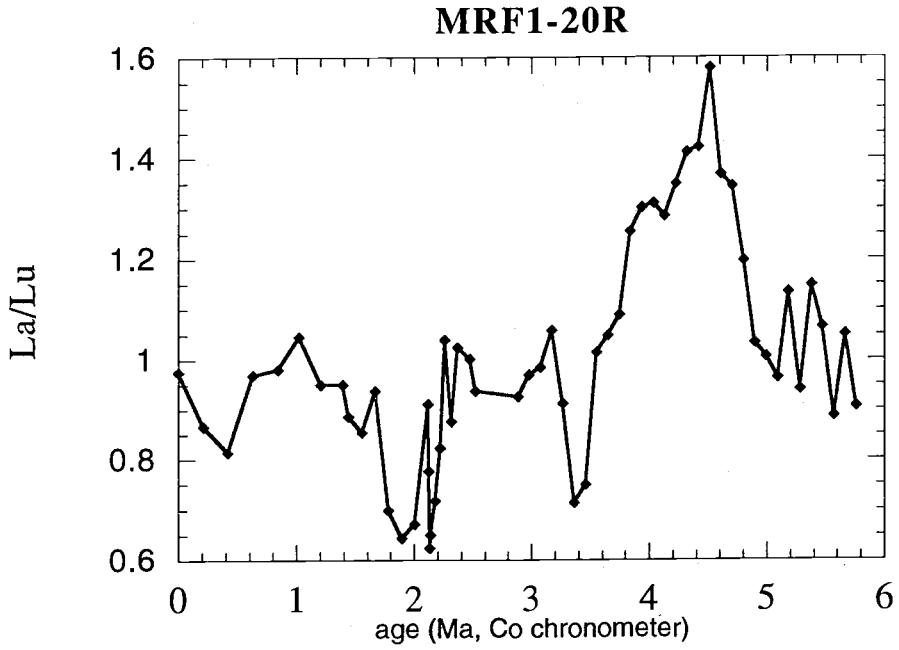

Figure III.19.C.

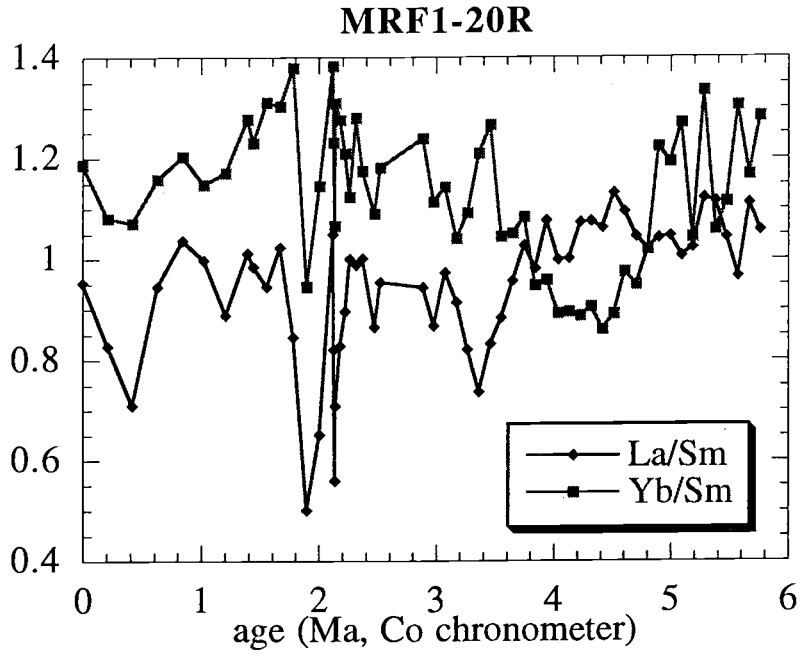

Figure III.19.D.

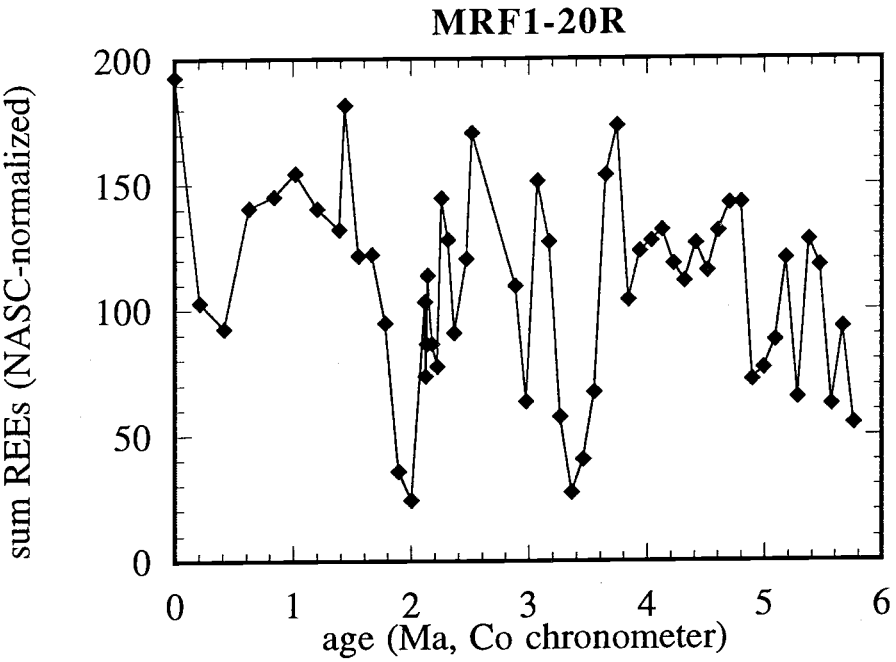

history, opposite to the increase with depth seen in the water column in Figure III.18 A. Total REE concentration oscillates during the growth history of MRF1-20R, but there is a general increasing trend towards the surface of the sample, with maximum total REEs occurring at the nodule's surface (Figure III.19 D). Crusts MRF6-12R and MRF2-3R do not uphold this trend, however. MRF6-12R shows a maximum HREE enrichment at approximately 1.1 Ma, with considerably less HREE fractionation at the sample surface and nearer the nucleus (Figure III.20 A). La/Lu generally decreases from approximately 1.8 Ma to around 1 Ma, after which it increases slightly (Figure III.20 B). La/Sm shows a generally decreasing trend throughout the growth history of the crust, indicating progressive middle REE enrichment (Figure III.20 C). Total REEs in MRF6-12R are highest near the substrate (Figure III.20 D), gradually degreasing towards the crust surface—the opposite of the trend exhibited by MRF1-20R.

MRF2-3R, the thickest crust analyzed, has the most complex REE profile of all of the samples. Much of this complexity is due to the fact that the crust had to be cut into three different sections to fit inside the LA ICP-MS sample holder. The three sections were then analyzed on different days, during which the ICP-MS detector had different sensitivities. This resulted in different instrumental responses, which in turn affected calculations. The junction between the first and second sections of MRF2-3R is plainly

Figure III.20. REE fractionation indexes versus age, Mendocino crust MRF6-12R. A) Heavy/light REEs, B) La/Lu, C) La/Sm and Yb/Sm, and D) total REEs (NASC-normalized).

Figure III.20.A.

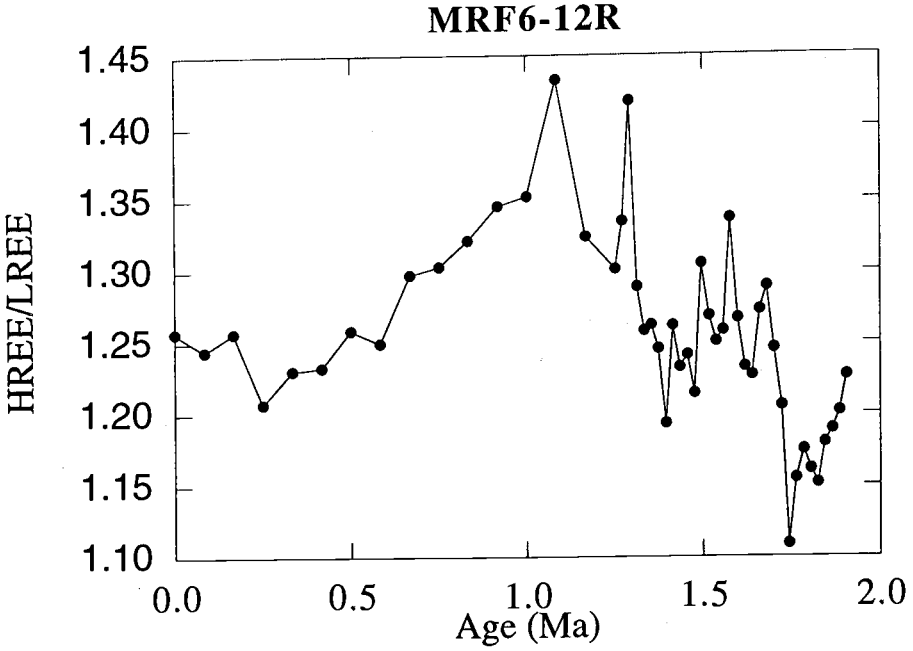

Figure III.20.B.

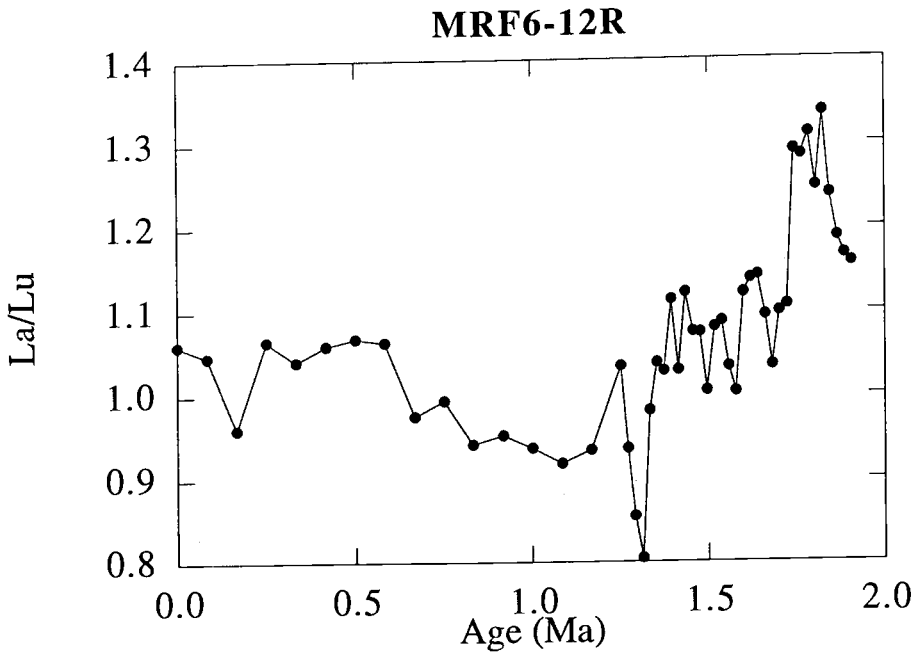

Figure III.20.C.

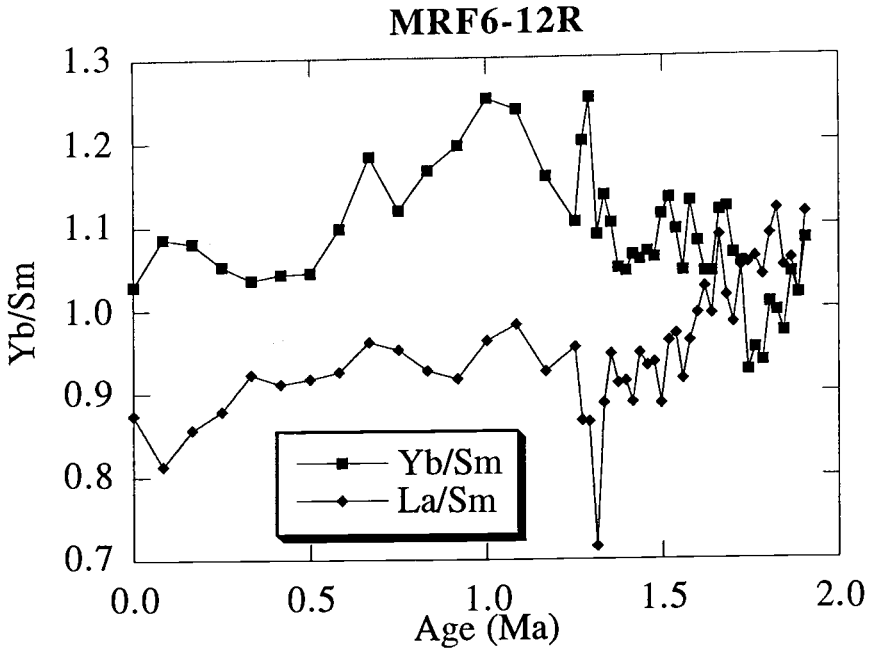

Figure III.20.D.

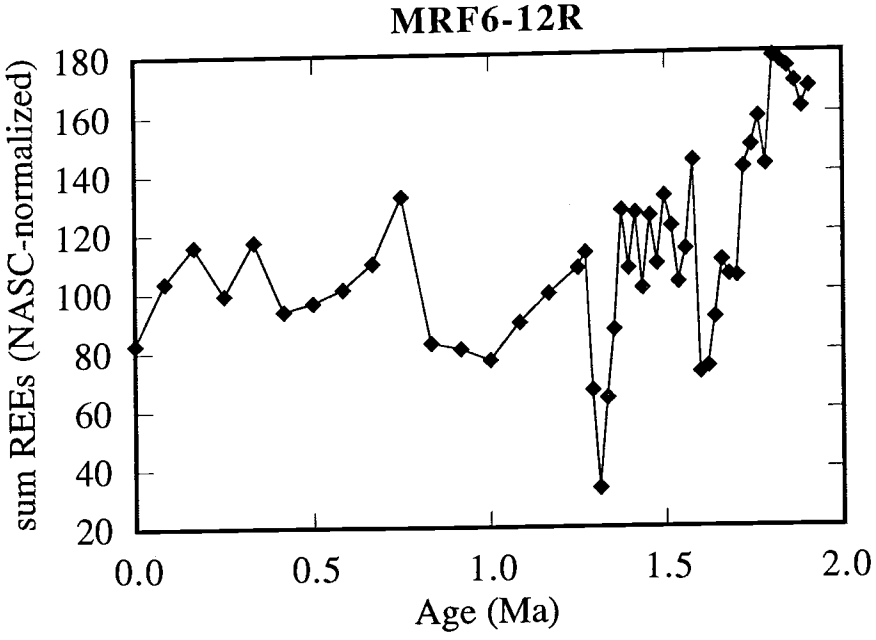

visible in the HREE/LREE plot at 2.8 Ma. Considering only the outermost section of crust, there is less HREE enrichment as one approaches the surface of the crust, as evidenced by the HREE/LREE, La/Lu, and Yb/Sm plots (Figure III.21 A-C). Total REEs increase toward the crust surface over this interval, as well (Figure III.21 D).

4.5.3.3 *Ce and Eu anomalies*

Another useful paleoenvironmental proxy from REEs is the cerium anomaly, which is widely accepted as a record of the degree of oxia in a manganese oxyhydroxide's environment of formation. Cerium, an exception to the generally coherent behavior of the REEs as a group, is largely controlled by oxidation/reduction chemistry in seawater. In seawater Ce is preferentially oxidized from its trivalent oxidation state to Ce^{4+}, which is an insoluble ion removed from solution by precipitation as an oxide. This removal results in a strong negative cerium anomaly, relative to neighboring La and Pr, in oxic seawater. Oxidation of Ce^{4+} occurs readily on the surfaces of Mn oxides, resulting in strong positive cerium anomalies are common in manganese nodules and crusts (German and Elderfield, 1990; de Baar et al., 1985). Some researchers have reported negative Ce anomalies in deep-sea nodules that have been diagenetically influenced, and in hydrothermal manganese oxides (Nath et al., 1997). The Ce anomaly is defined by $Ce^* = \log[3*Pr/(2*La+Nd)]$, with all REE concentrations normalized to North American Shale Composite (NASC) values. Ce* values greater than

Figure III.21. REE fractionation indexes versus age, Mendocino crust MRF2-3R. A) Heavy/light REEs, B) La/Lu, C) La/Sm and Yb/Sm, and D) total REEs (NASC-normalized).

Figure III.21.A.

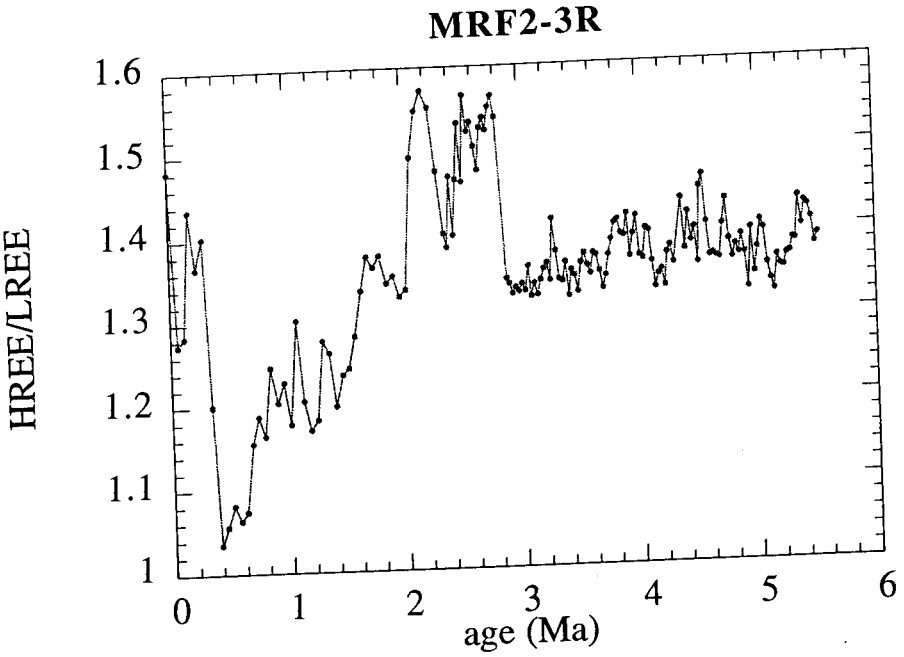

Figure III.21.B.

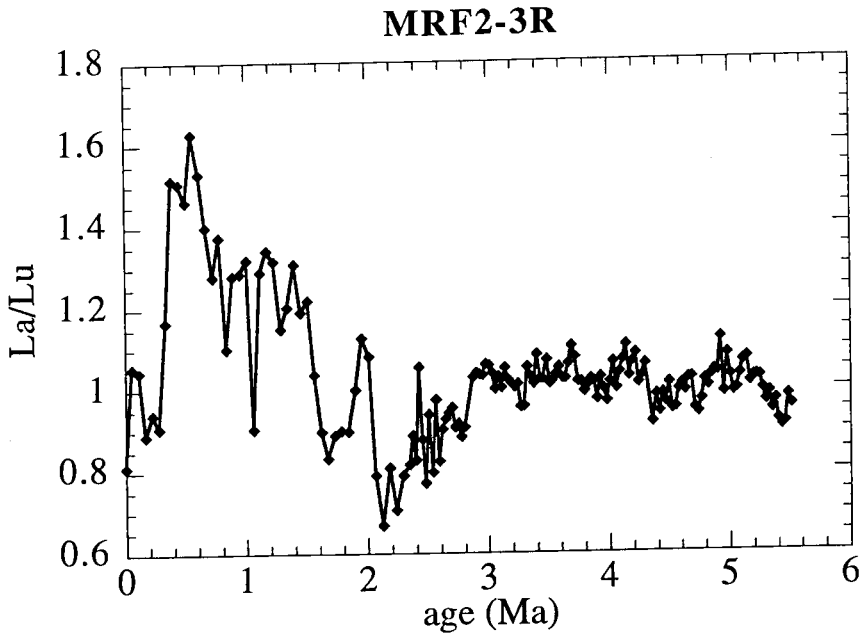

Figure III.21.C.

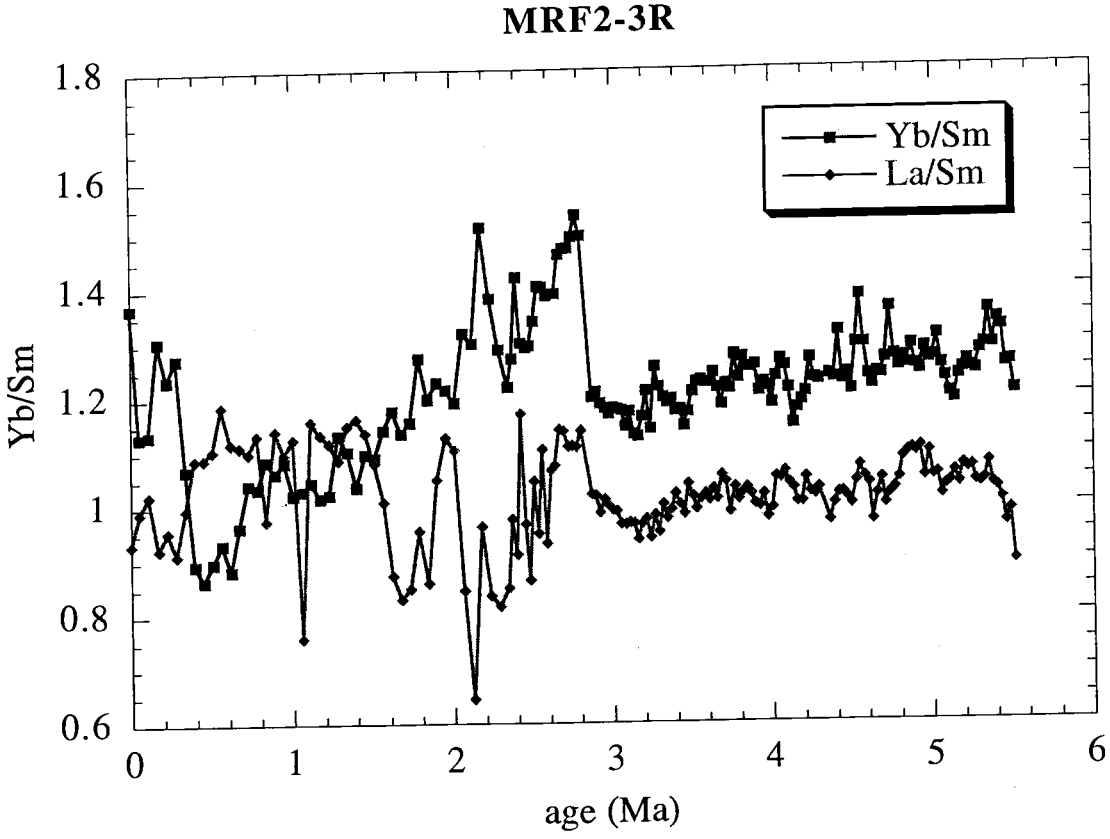

Figure III.21.D.

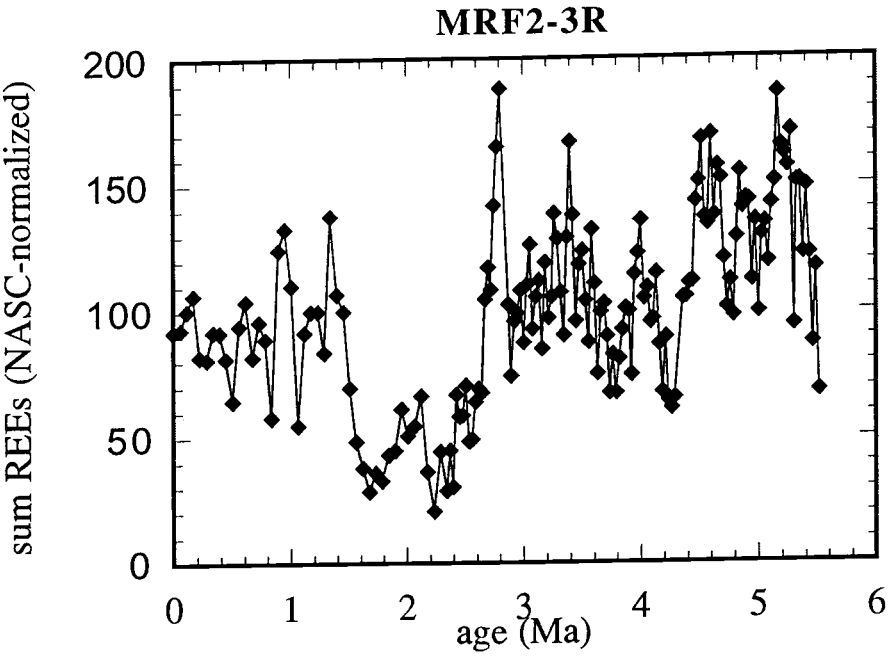

0 indicate formation under oxic conditions, while Ce* values less than 0 indicate formation in suboxic environments.

Europium also demonstrates non-group variability due to changes in oxidation state. Europium is reduced in acidic, high-pressure environments to a divalent oxidation state. Eu^{2+} has a larger ionic radius than its neighboring trivalent REEs, and therefore behaves anomalously. Strong positive Eu anomalies (Eu*) have been reported in hydrothermal fluids and some igneous deposits (de Baar et al., 1985 and Elderfield, 1988). Additionally, Klinkhammer et al. (1994) report strong Eu anomalies in hydrothermal particulate samples collected near vent outflows on the Mid Atlantic Ridge. There has been little mention in the literature of Eu anomalies in hydrothermal manganese oxides, however, and it is likely that the Eu* signature will be undistinguishable in manganese oxides other than those which are highly hydrothermal.

With the redox-sensitive behavior of Ce and Eu in mind, a number of studies have pursued the hypothesis that REE distributions within geological materials can be used to infer paleoredox conditions during their formation history (De Carlo, 1990; Nath et al., 1992; and Addy, 1979). While the Ce anomaly is certainly a sensitive proxy for anoxic and suboxic environments, German and Elderfield (1990) determined that the Ce anomaly does not serve as an instantaneous recorder of water column conditions directly over a crust or nodule, rather it serves as an integrated record of the redox conditions of

the water mass(es) which a crust or nodule has encountered, especially in the case of hydrogenetic deposits. The distribution of REEs within ferromanganese oxide deposits has been demonstrated to be mineralogically sensitive (De Carlo, 1991; Nath et al., 1992; German and Elderfield, 1990), with REEs commonly partitioning onto iron- and phosphate-rich phases, likely due to scavenging. While a number of researchers have reported direct correlation of the Ce anomaly with Fe content (German and Elderfield, 1990; Baturin, 1987), De Carlo (1990) reports correlation between the Ce anomaly and Mn content, yet an association of trivalent REEs with Fe in a Central Pacific crust. This implies that variations in the Ce anomaly may be due to mineralogically-induced differences in trivalent REE content as well as to changes in redox conditions, and therefore he urges caution in interpreting Ce anomaly variations.

Ce anomalies were calculated for each sample and plotted versus age. Both crust samples reflect formation in progressively more oxic conditions early in their growth history. That is, the Ce anomaly is most negative near the substrate, with progressively more positive values as growth proceeds. This may indicate that the crusts initially formed in an area of hydrothermal activity, with the gradual increase in Ce anomaly due to a decrease in hydrothermal influence over time, or it may be a record of the movement of these samples through the O_2 minimum layer and into more oxic waters beneath. MRF2-3R initially exhibits a Ce anomaly value of –0.2, which quickly drops to a minimum value of –0.5 after its first 0.2 Ma of growth (Figure III.22A). These Ce*

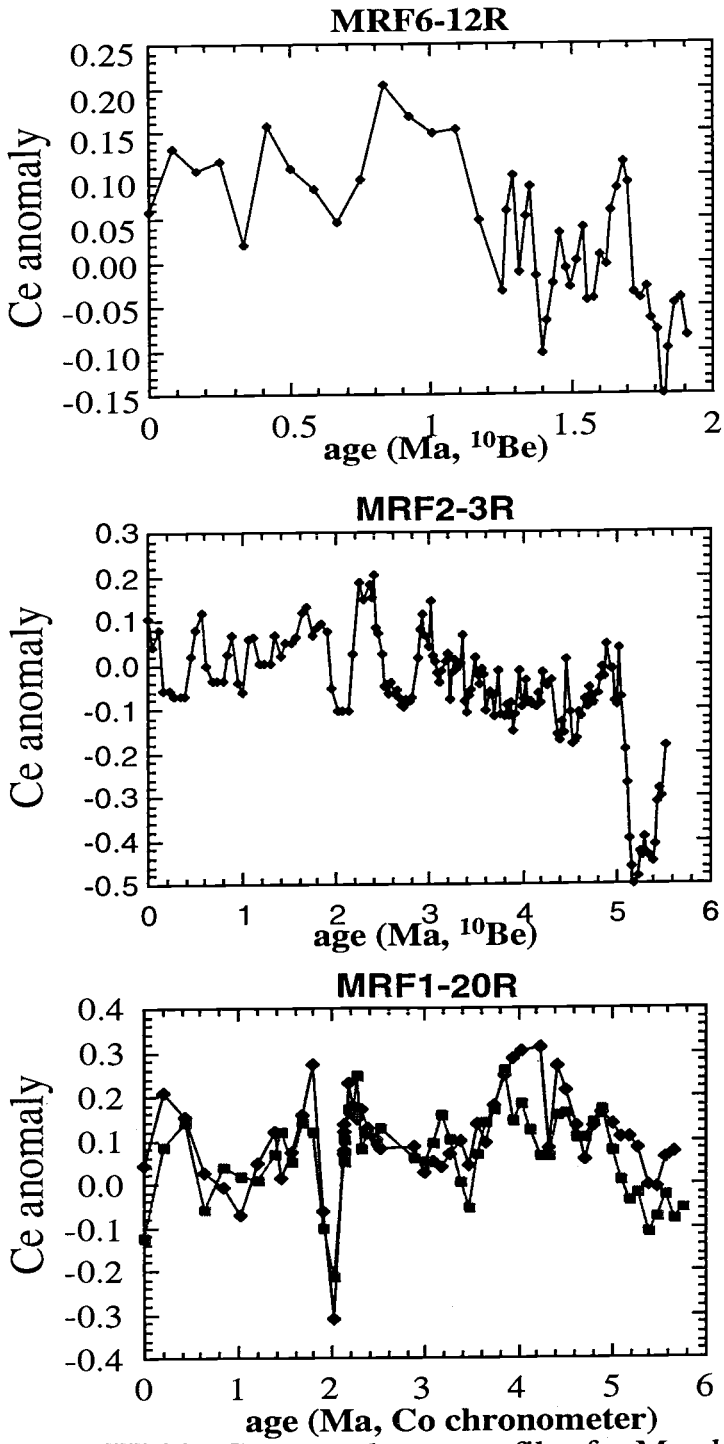

Figure III.22. Ce anomaly age profiles for Mendocino ferromanganese deposits. Values > 0 indicate formation in oxic conditions. A) MRF2-3R, B) MRF6-12R, C) MRF1-20R (two different runs). LA ICP-MS data.

values are comparable to values reported by Nath et al. (1997) for hydrothermal crusts from the Indian Ocean, which range from –0.277 to –0.411. Over the next 0.1 Ma the Ce anomaly value shifts abruptly to near 0, then climbs gradually to a maximum of 0.2 at approximately 2.2 Ma, and from 2 Ma to present Ce* oscillates between 0.1 and –0.1. MRF6-12R has a similar history, in that Ce* is lowest near the nucleus, with a minimum value of –0.15 at 1.6 Ma (Figure III.22 B). The maximum Ce* value occurs at approximately 1.7 Ma, but MRF6-12R does not exhibit any negative Ce* values in the past 1 Ma. Nodule MRF1-20R (during two separate LA ICP-MS runs) shows a gradual increase in Ce* over roughly the first 1.5 Ma of growth, with a prominent Ce* peak of 2.5 - 3.0 centered around 4 Ma (Figure III.22 C). The period around 2 Ma is complex, with a pronounced minimum value of –0.3 at 2.0 Ma, which sharply rises to approximately 0.2 at 1.8 Ma, followed by a general decrease toward the surface of the nodule. The complex history of this nodule suggests that it may have been turned over several times during its growth, if it is indeed diagenetically-influenced, or that it may have experienced more episodic hydrothermal influence than the other samples.

REE data portrayed in Figure III.15 also exhibit a general trend in the Ce anomaly—crusts MRF2-3R and MRF6-12R both show generally decreasing Ce anomalies with depth in the crusts, possibly indicating a gradual increase in oxia during

the course of their formation, possibly indicating subsidence below the O_2 minimum zone or waning hydrothermal influence.

5. Conclusions

Ferromanganese oxyhydroxide deposits from the Mendocino Ridge were analyzed for a variety of geochemical characteristics, including growth rates and trace and major elemental contents and distributions, and a number of proxies derived from these traits were investigated. In general, it appears that the Mendocino Ridge manganese deposits are of primarily hydrogenetic origin. Growth rates are slow (<20mm/Ma), suggesting formation primarily by hydrogenetic precipitation, except for those portions that grew faster than 15 mm/Ma (Hein et al., 1997, cite this value as the upper limit for hydrogentic growth). Periods of slightly faster growth suggest contribution of dissolved metals from hydrothermal or diagenetic sources, or perhaps periods of elevated productivity. Trace and major element concentrations and interrelationships also suggest a primarily hydrogenetic origin for the Mendocino manganese deposits, although some degree of hydrothermal influence is suggested by multiple proxies in every sample. In all cases, this hydrothermal influence occurs predominantly in the deeper portions of the deposits, suggesting more active hydrothermalism in this region in the past than is currently observed. The westward propagation of the Mendocino Fracture Zone relative to the Gorda Ridge may have

played a role in the record of hydrothermal influence in these samples. The Gorda Ridge was in much closer proximity 5-6 million years ago, and it is quite likely that hydrothermally influenced water advected southward from the Gorda Ridge to the MFZ, supplying elevated concentrations of Mn to Mendocino manganese deposits. The OMZ, however, plays a major role in supplying dissolved Mn, and its dynamics in this region undoubtedly changed drastically during the subsidence of the Mendocino Ridge, as did the proximity of the samples to this hydrographic feature. It is difficult to distinguish between hydrothermal and OMZ metal sources in these samples because the hydrothermal influence is so far removed that the hydrothermal signal is overwhelmed by the dominant hydrogenetic source. Similarities between redox processes occurring in the water column and in surficial sediments make it difficult to distinguish between metal enrichments in nodules and crusts from OMZ and diagenetic sources. The "cannonball" nodule, MRF1-20R, displays characteristics of diagenetic accumulation (although not of intense diagenetic flux), but it was recovered in an area devoid of sediment. Perhaps the remobilization of metals in the water column from OMZ-associated redox processes is actually the cause of the "diagenetic" signal in this nodule.

REE distributions in the water column offer a suite of promising proxies for elucidating the depth of formation of ferromanganese oxyhydroxides. Unfortunately, water column data are very sparse due to difficulty in sampling for and analyzing REEs in seawater. Some general trends in REE distribution common to both seawater and

ferromanganese deposits were noted, however, especially in the case of the "cannonball" nodule, which demonstrates increased total REEs & relative HREE enrichment over the course of its formation and the subsidence of the Mendocino Ridge. Given more water column REE data from nearby waters, it might be possible to construct a depth-history model based on REE fractionation for ferromanganese oxyhydroxides.

IV. CONCLUSIONS

Laser Ablation Inductively-Coupled Mass Spectrometry (LA ICP-MS) is a powerful tool for the chemical analysis of solid samples over fine spatial scales. LA ICP-MS lends itself particularly well to geochemical investigations of mineral phases which form in changing environmental conditions, and this technique was successfully employed for examining ferromanganese deposits from the Mendocino Fracture Zone.

Analysis of a suite of ferromanganese crusts from the Mendocino Ridge revealed that a number of environmental factors have changed substantially during the interval over which these mineral phases accumulated. Changes in growth rates and composition revealed differences in the amount of dissolved metals available to support crust growth, suggesting 1) changes in the extent and proximity of hydrothermal activity on the nearby Escanaba Trough and Gorda Ridge, 2) changes in depth due to subsidence of the Mendocino Ridge, and 3) changes in water column chemistry (i.e. oxygen minimum zone) due to subsidence. When combined with chronometric analyses, these results reveal that the marine environment surrounding the Mendocino Ridge is very dynamic over geological timescales, and that dramatic shifts in ambient conditions have occurred here in the past. The fact that environmental signals do not occur simultaneously in all samples suggests that ferromanganese crusts function as recorders of conditions in their

immediate surroundings, and that water column conditions along the Mendocino Ridge are not homogeneous.

This study would have benefited from mineralogical determinations, which would provide more insight into the redox chemistry of the waters surrounding these crusts. Also, more comprehensive water column chemistry data (especially trace metals and rare Earth elements) from the study area would be helpful for comparison with the most recent crust layers.

A potentially exciting avenue for future work is the use of laser ablation in conjunction with a high-resolution mass spectrometer capable of performing precise isotopic determinations and resolving elements that are below detection limits using conventional ICP-MS (i.e. Re and Os). Such an instrument would also allow acquisition of data over the smallest spatial scale (i.e. smaller spot sizes) that the laser is capable of achieving; the amount of material delivered to the mass spectrometer would be sufficient to resolve all elements of interest.

BIBLIOGRAPHY

Addy, S. K., 1979. Rare earth element patterns in manganese nodules and micronodules from northwest Atlantic. Geochim. Cosmochim. Acta. 43:1105-1115.

Anderson, R. F., Lao, Y., Broecker, W. S., Trumbore, S. E., Hofman, H. J., and Wolfli, W. 1990. Boundary scavenging in the Pacific Ocean; a comparison of ^{10}Be and ^{231}Pa. EPSL. 96:287-304.

Baker, E. T., Massoth, G. J., Collier, R. W., Trefry, J. H., Kadko, D., Nelsen, T. A., Rona, P. A., and Lupton, J. E. 1987. Evidence for high-temperature hydrothermal venting on the Gorda Ridge, northeast Pacific Ocean. Deep-Sea Research. 8:1461-1476.

Barry, J.P., Greene, H.G., Orange, D.L., Baxter, C.H., Robison, B.H., Kochevar, R.E., Nybakken, J.W., Reed, D.L., and McHugh, C.M. 1996. Biologic and Geologic Characteristics of Cold Seeps in Monterey Bay, California. Deep-Sea Research. 43:1739-1762.

Baturin, G. N. 1987. The geochemistry of manganese nodules in the ocean. Reidel, Dodrecht. 342 pp.

Bau, M., Koshcinsky, A., Dulski, P., and Hein, J. R. 1996. Comparison between the partitioning behaviors of yttrium, rare earth elements, and titanium between hydrogenetic ferromanganese crusts and seawater. Geochim. Cosmochim. Acta. 60:1709-1725.

von Blanckenburg, F., Belshaw, N. S., and O'Nions, R. K. 1996a. Separation of ^{9}Be and cosmogenic ^{10}Be from environmental materials and SIMS isotope dilution analysis. Chemical Geology. 129:93-99.

von Blanckenburg, F., O'Nions, R. K., Belshaw, N. S., Gibb, A., and Hein, J. R. 1996b. Global distribution of beryllium isotopes in deep ocean water as derived from Fe-Mn crusts. EPSL. 141:213-226.

Bonatti, E., Kraemer, T., and Rydell, H. 1972. Classification and genesis of submarine iron-manganese deposits. *In*: Horn, D. R., [ed.], Papers from a conference on ferromanganese deposits on the ocean floor. Arden House, New York. pp. 149-166.

Branica, M., Degobbis, D., Cosovic, B., and Bilinski, H. Inorganic cobalt species in seawater. Rapports et Proces-verbaux des Reunions. 27:111-117.

Carriker, M. R., Swann, C. P., and Ewart, J. W. 1982. An exploratory study with the proton microprobe of the ontogenetic distribution of 16 elements in the shell of living oysters (*Crassostrea virginica*). Marine Biology. 69:235-246.

Christensen, J. N., Halliday, A. N., Godfrey, L. V., Hein, J. R., and Rea, D. K. 1997. Climate and ocean dynamics and the lead isotopic records in Pacific ferromanganese crusts. Science. 277:913-918.

Cronan, D. S. 1977. Deep-sea nodules: Distribution and geochemistry. *In:* Glasby, G. P. Marine manganese deposits. Elsevier, New York. pp. 11-44.

Cronan, D. S. 1997. Some controls on the geochemical variability of manganese nodules with particular reference to the tropical South Pacific. *In:* Nicholson, K., Hein, J. R., and Buhn, B., [eds.], Manganese Mineralization: Geochemistry and Mineralogy of Terrestrial and Marine Deposits. Geological Society, London. pp.139-151.

Crowley, T. J. 1996. Pliocene climates: The nature of the problem. Marine micropaleontology. 27:3-12.

Dalrymple, G. B., and Lanphere, M. A. 1969. Potassium-argon dating: Principles, techniques, and applications to geochronology. Freeman, San Francisco. 258 pp.

Darke, S. A., and Tyson, J. F. 1993. Interaction of laser radiation with solid materials and its significance to analytical spectrometry. J. Anal. At. Spectrom. 8:145-209.

Davies, J. F.; Prevec, S. A.; Whitehead, R. E.; and Jackson, S. E. 1998. Variations in REE and Sr-isotope chemistry of carbonate gangue, Castellanos Zn-Pb deposit, Cuba. Chemical Geology. 144, 99-119.

De Baar, H. J. W., Bacon, M. P., and Brewer, P. G. 1985. Rare earth elements in the Pacific and Atlantic Oceans. Geochim. Cosmochim. Acta. 49:1943-1959.

De Carlo, E. H. 1991. Paleoceanographic implications of rare earth element variability within a Fe-Mn crust from the central Pacific Ocean. Marine Geology. 98: 449-467.

Denoyer, E.R., Fredeen, K. J., and Hager, J. W. 1991. Laser solid sampling for inductively coupled plasma mass spectrometry. Anal. Chem. 63:445A-457A.

Domack, C. R. 1986. Reconstruction of the California Current at 5, 8, and 10 million years b.p. using radiolarian indicators. *In*: Casey, R. and Barron, J., [eds.], Field Trip Guidebook—Pacific section, Society of Economic Paleontologists and Mineralogists, v. 45. Society of Economic Paleontologists and Mineralogists, Pacific section, Los Angeles. pp. 39-54

Duncan, R. A.; Fisk, M. R.; Carey, A. G.; Lund, D.; Douglas, L.; Wilson, D. S.; Krause, D.; Stewart, R.; and Fox, C. G. 1994. Origin and emergence of the Mendocino Ridge. Eos. 71:475.

Dymond, J., Lyle, M., Finney, B., Piper, D. Z., Murphy, K., Conard, R., and Pisias, N. 1984. Ferromanganese nodules from MANOP sites H, S, and R—Control of mineralogical and chemical composition by multiple accretionary processes. Geochim. Cosmochim. Acta. 48:931-949.

Eisenhauer, A., Gogen, K., Pernicka, E., and Mangini, A. 1992. Climatic influences o the growth rates of Mn crusts during the Late Quaternary. EPSL. 109:25-36.

Elderfield, H. 1988. The oceanic chemistry of the rare-earth elements. Phil. Trans. R. Soc. Lond. 325:105-126.

Falkner, K. K., Klinkhammer, G. P., Ungerer, C. A., and Christie, D. M. 1995. Inductively coupled mass spectrometry in geochemistry. Annu. Rev. Earth Planet. Sci. 23:409-449.

Faure, G. 1986. Principles of isotope geology. New York, Wiley & Sons. pp. 405 – 428.

Feng, R. 1994. In situ trace element determination of carbonates by Laser Probe inductively coupled plasma mass spectrometry using non matrix matched standardization. Geochim. Cosmochim. Acta 58:1615-1623.

Fisk, M. R., Duncan, R. A., Fox, C. G., and Wittier, J. B. 1992. Emergence and Petrology of the Mendocino Ridge. Marine Geophysical Researches. 15:283-296.

Fisk, M. R., and Howard, K. J. 1990. Geology and Geophysics of Gorda Ridge. *In*: McMurray, G. R., [ed.], Gorda Ridge: A seafloor spreading center in the United States' exclusive economic zone. New York, Springer-Verlag, pp. 3-20.

Flanagan, F. J. and Gottfried, D. 1980. USGS Rock Standards, III: Manganese-nodule reference samples USGS-Nod-A-1 and USGS-Nod-P-1. United States Geological Survey Professional Paper 1155. United States Government Printing Office, Washington, DC. 39 pp.

Frank, M., O'Nions, R.K., Hein, J. R., and Banakar, V. K. 1999. 60 Myr records of major elements and Pb-Nd isotopes from hydrogenous ferromanganese crusts: Reconstruction of seawater paleochemistry. Geochim. Cosmochim. Acta. 63:1689-1708.

Gray, A. L. 1985. Solid sampling for inductively coupled plasma mass spectroscopy. Anal. Chem. 63:551-556.

Garbe-Schonberg, C. D.; and McMurty, G. M. 1994. In-situ micro-analysis of platinum and rare earths in ferromanganese crusts by laser ablation-ICP-MS (LAICPMS). Fresenius J. Anal. Chem. 350:264-271.

German, C. R., and Elderfield, H. 1990. Application of the Ce anomaly as a paleoredox indicator: the ground rules. Paleoceanography. 5:823-833.

Hager, J. W. 1989. Relative elemental responses for laser ablation inductively coupled mass spectrometry. Anal. Chem. 61:1243-1248.

Halbach, P., Giovanoli, R., and von Bostel, D. 1982. Geochemical processes controlling the relationship between Co, Mn, and Fe in early diagenetic deep-sea nodules. Earth and Planetary Science Letters. 60: 226-236.

Halbach, P., and Puteanus, D. 1984. The influence of the carbonate dissolution depth on the growth and composition of Co-rich ferromanganese crusts from Central Pacific seamount areas. Earth Planet. Sci. Lett. 68:73-87.

Halbach, P., Segl, M., Puteanus, D., and Mangini, A. 1983. Co-fluxes and growth rates in ferromanganese deposits from central Pacific seamount areas. Nature. 304:716-719.

Hart, S. and Blusztajn, J. 1998. Clams as recorders of ocean ridge volcanism and hydrothermal vent field activity. Science. 280:883-886.

Hein, J. R., Bohrson, W. A., and Schulz, M. S. 1992. Variations in the fine-scale composition of a central Pacific ferromanganese crust: paleoceanographic implications. Paleoceanography. 7:63-77.

Hein, J.R., Koschinsky, A., Halbach, P., Manheim, F. T., Bau, M., Kang, J., and Lubick, N. 1997. Iron and manganese oxide mineralization in the Pacific. *In:* Nicholson, K., Hein, J. R., and Buhn, B., [eds.], Manganese Mineralization: Geochemistry and Mineralogy of Terrestrial and Marine Deposits. Geological Society, London. pp.123-138.

Hein, J. R., Schulz, M. S., and Gein, L. M. 1992. Central Pacific cobalt-rich ferromanganese crusts: historical perspective and regional variability. *In:* Keating, B. H., and Bolton, B. R. [eds.], Geology and offshore mineral resources of the central Pacific basin, Circum-Pacific Council for Energy and Mineral Resources Earth Science Series, V. 14, New York, Springer-Verlag. pp. 261-283.

Hein, J. R., Schwab, W. C., and Davis, A. S. 1988. Cobalt- and platinum-rich ferromanganese crusts and associated substrate rocks from the Marshall Islands. Marine Geology. 78:255-283.

Hlawatsch, S., and Suess, E. 1993. Trace element patterns in ferromanganese concretions from the western Baltic Sea: Indicator for environmental change. EOS. 74:363.

Huh, C.-A., and Ku. ,T.-L. 1990. Distribution of thorium 232 in manganese nodules and crusts: Paleoceanographic implications. Paleoceanography. 5:187-195.

Huh, C.-A., Moore, W. S., and Kadko, D. C. 1989. Oceanic ^{232}Th: A reconnaissance and implications of global distribution from manganese nodules. Geochim. Cosmochim. Acta. 53:1357-1366.

Imai, H. 1992. Microprobe analysis of geological materials by laser ablation inductively coupled plasma mass spectrometry. Anal. Chim. Acta. 269:263-268.

Jarvis, K. E. and Williams, J. G. 1993. Laser ablation inductively coupled mass spectrometry (LA-ICP-MS): a rapid technique for the direct, quantitative determination of major, trace, and rare-earth elements in geological samples. Chem. Geol., 106:251-262.

Johnson, K. S.; Coale, K. H., Berelson, W. M., and Gordon, R. M. 1995. On the formation of the manganese maximum in the oxygen minimum. Geochim. Cosmochim. Acta. 8:1291-1299.

Keigwin, L. D. 1987. Toward a high-resolution chronology for latest Miocene paleoceanographic events. Paleoceanography. 2:639-660.

Kennett, J. P. 1982. Marine Geology. New Jersey, Prentice-Hall. 813 pp.

Klinkhammer, G. P., German, C. R., Elderfield, H., Greaves, M. J., and Mitra, A. 1994. Rare earth elements in hydrothermal fluids and plume particulates by inductively coupled plasma mass spectrometry. Marine Chemistry. 45:179-186.

Knauer, G. A., Martin, J. H., and Gordon, R. M. 1982. Cobalt in Northeast Pacific waters. Nature. 297:49-51.

Koschinsky, A. and Halbach, P. 1995. Sequential leaching of marine ferromanganese precipitates: Genetic implications. Geochim. Cosmochim. Acta. 59:5113-5132.

Koschinsky, A., Stascheit, A., Bau, M., and Halbach, P. 1997. Effects of phosphatization on the geochemical and mineralogical composition of marine ferromanganese crusts. Geochim. Cosmochim. Acta. 61:4079-4094.

Krause, D. C., Menard, H. W., and Smith, S. M. 1964. Topography and lithology of the Mendocino Ridge. J. Mar. Res. 22:236-249.

Landing, W.M. and Bruland, K. W. 1980. Manganese in the North Pacific. EPSL. 49:45-56.

Lao, Y., Anderson, R. F., and Broecker, W. S. 1992. Boundary scavenging and deep-sea sediment dating: constraints from excess ^{230}Th and ^{231}Pa. Paleoceanography. 7:783-798.

Lei, G. and Boström, K. 1995. Mineralogical control on transition metal distributions in marine manganese nodules. Marine Geology. 123:253-261.

Manheim, F. T. and Lane-Bostwick, C. M. 1988. Cobalt in ferromanganese crusts as a monitor of hydrothermal discharge on the pacific sea floor. Nature. 335:59-62.

Martin, J. H., Knauer, G. A., and Broenkow, W. W. 1985. VERTEX: the lateral transport of manganese in the northeast Pacific. Deep-Sea Res. 32:1405-1427.

McMurtry, G. M., VonderHaar, D. L., Eisenhauer, A., Mahoney, J. J., and Yeh, H.-W. 1994. Cenozoic accumulation history of a Pacific ferromanganese crust. EPSL. 125:105-118.

Menard, H. W. 1964 Marine Geology of the Pacific. McGraw-Hill, New York, 271 pp.

Moenke-Blankenburg, L. 1989. Laser Microanalysis. Wiley, New York, NY, 288 pp.

Murphy, K. and Dymond, J. 1984. Rare earth element fluxes and geochemical budget in the eastern Equatorial Pacific. Nature. 307:444-447.

Nath, B. N., Balaram, V., Sudhakar, M., and Pluger, W. L. 1992. Rare earth element geochemistry of ferromanganese deposits from the Indian Ocean. Marine Chemistry. 38:185-208.

Nath, B. N., Pluger, W. L., and Roelandts, I. 1997. Geochemical constraints on the hydrothermal origin of ferromanganese encrustations from the Rodriguez Triple Junction, Indian Ocean. *In:* Nicholson, K., Hein, J. R., and Buhn, B., [eds.], Manganese Mineralization: Geochemistry and Mineralogy of Terrestrial and Marine Deposits. Geological Society, London. pp.199-211.

Naydu, Y. R., 1965. Petrology of submarine volcanics and sediments in the vicinity of the Mendocino Fracture Zone. Progress in Oceanography. 3:207-220.

Perkins, W.T., Fuge, R., Pearce, N.J.G. 1991. Quantitative analysis of trace elements in carbonates using laser ablation inductively coupled mass spectrometry. J. Anal. At. Spectrosc., 6: 445-449.

Piepgras, D. J., and Jacobsen, S. B. 1992. The behavior of rare earth elements in seawater: Precise determination of variations in the North Pacific water column. Geochim. Cosmochim. Acta. 56:1851-1862.

Pillsbury, R. D. et al. 1982. Data report for current meters in Mooring CMMW-4, 1981; Pacific study area W-N. Sandia National Lab. Report OSU-14. 65 pp.

Piper, D. Z. 1974. Rare Earth elements in the sedimentary cycle: A summary. Chemical Geology. 14:285-304.

Pisias, N. G., Mayer, L. A., and Mix, A. C. 1995. Paleoceanography of the Eastern Equatorial Pacific during the Neogene: Synthesis of leg 138 drilling results. *In*: Pisias, N. G., Mayer, L. A., Janecek, T. R., Palmer-Julson, A., and van Andel, T. H., [eds.], Proceedings of the Ocean Drilling Program, scientific results, Vol. 138. Ocean Drilling Program, College Station, TX. pp. 5-21.

Redmond, G., Batel, A., Rocques-Carmes, C., Wehbi, D., Abell, I., and Seroussi, G. 1990. Scanning mechanical microscopy of laser ablated volumes related to inductively coupled plasma mass spectrometry: a new technique for the determination of trace and ultra-trace elements in silicates. Geochim. Cosmochim. Acta. 57:475-482.

Romine, K. 1985. Radiolarian biogeography and paleoceanography at the North Pacific at 8 Ma. . *In*: Kennett, J. P., [ed.], The Miocene ocean: paleoceanography and biogeography. Geological Society of America memoir 163. pp. 237-272.

Sancetta, C., Lyle, M., and Heusser, L. 1992. Late-Glacial to Holocene changes in winds, upwelling, and seasonal production of the Northern California Current system. Quaternary Research. 38:359-370.

Sharma, P., Church, T. M., and Bernat, M. 1989. Use of cosmogenic ^{10}Be and ^{26}Al in phillipsite for the dating of marine sediments in the South Pacific Ocean. Chemical Geology. 73:279-288.

Sharma, P., Klein, J., Middleton, R., and Church, T. M. 1987. ^{26}Al and ^{10}Be in authigenic marine minerals. Nuclear Instruments and Methods in Physics Research. B29:335-340.

Spencer, D. W., Robertson, D. E., Turekian, K. K., and Folsom, T. R. 1970. Trace element calibrations and profiles at the Geosecs test station in the Northeast Pacific Ocean. JGR. 75:7688-7696.

Stecher, H. A., Krantz, D. E., Lord, C. J. III, Luther, G. W. III, and Bock, K. W. 1996. Profiles of strontium and barium in *Mercenaria mercenaria* and *Spisula solidissima* shells. Geochim. Cosmochim. Acta. 18:3445-3456.

Takematsu, N., Sato, Y., and Okabe, S. 1984. The formation of todorokite and birnessite in seawater pumped from underground. Geochim. Cosmochim. Acta. 48:1099-1106.

Takematsu, N., Sato, Y., and Okabe, S. 1989. Factors controlling the chemical composition of marine manganese nodules and crusts: a review and synthesis. Marine Chemistry. 26:41-56.

Tera, F., Brown, L., Morris, J., Sacks, I. S., Klein, J., and Middleton, R. 1986. Sediment incorporation in island-arc magmas: Inferences from ^{10}Be. Geochim. Cosmochim. Acta. 50:535–550.

Usui, A., and Someya, M. 1997. Distribution and composition of marine hydrogenetic and hydrothermal manganese deposits in the northwest Pacific. *In:* Nicholson, K., Hein, J. R., and Buhn, B., [eds.], Manganese Mineralization: Geochemistry and Mineralogy of Terrestrial and Marine Deposits. Geological Society, London. pp. 177-198.

Williams, J. G. and Jarvis, K. E. 1993. Preliminary assessment of laser ablation inductively coupled plasma mass spectrometry for quantitative multi-element determination in silicates. J. Anal. At. Spectrom. 8:25-34.

Wilson, D.S. 1993. Confidence intervals for motion and deformation of the Juan de Fuca plate. Journal of Geophysical Research. 98:16053-16071.

Woodruff, F. 1985. Changes in Miocene deep-sea benthic foraminiferal distribution in the Pacific Ocean: Relationship to paleoceanography. *In*: Kennett, J. P., [ed.], The Miocene ocean: paleoceanography and biogeography. Geological Society of America memoir 163. pp. 131-176.

APPENDICES

Appendix A. LA ICP-MS data processing

Table A 1. Blank subtracted data are presented, with ten individual samples bracketed by three replicates of a pressed pellet standard.

Table A 2. Response correction is performed on blank subtracted data using the following formula:

$$RF = CPS/(conc*\%abund/100)$$

where RF = response factor (cps/ppm), conc = concentration (ppm) of a given element in Nod A-1, and %abund = percent abundance of the isotope analyzed. Response factors were averaged for each triplicate set of standards, and then RF values were interpolated for sample acquisitions between each set of standards.

Table A 3. Concentrations (ppm) are calculated from LA ICP-MS data using the following formula:

$$conc = cps/(RF*\%abund/100)$$

where conc = concentration (ppm) of the element of interest, cps is blank-subtracted data (counts*second^{-1}), RF = response factor (cps/ppm), and %abund = percent abundance of the isotope analyzed.

blank-subtracted data (cps)		Co	La	Ce	Pr	Nd	Sm	Eu	Gd	Tb
	mass	58.93	138.91	139.91	140.91	145.91	146.91	150.92	156.92	158.93
971029 MRF6-12R Nod A-1 1 1		3301174	498136	6008604	184621	141350	25786	23148	24018	27430
971029 MRF6-12R Nod A-1 2 1		3832014	469457	5591648	163215	115784	21475	20406	23240	28106
971029 MRF6-12R Nod A-1 3 1		3083553	552859	5304045	192163	141344	23937	23250	26035	32840
971029 MRF6-12R #1 1		1350993	849216	3888833	321301	258558	47183	44703	46524	54598
971029 MRF6-12R #2 1		1711467	979584	5329313	402206	324854	58884	57607	59572	70698
971029 MRF6-12R #3 1		1596769	1091497	5547844	442177	377776	62698	63949	67778	76887
971029 MRF6-12R #4 1		1933742	981821	4868379	398227	316068	55297	54627	60109	69997
971029 MRF6-12R #5 1		1908463	1223274	4687573	477607	380749	66048	61534	70035	80530
971029 MRF6-12R #6 1		1583946	933319	4817969	368356	297769	51345	49114	54623	63269
971029 MRF6-12R #7 1		1518043	969634	4366051	378553	310435	53334	51142	54333	63965
971029 MRF6-12R #8 1		1565554	1038165	4221844	389373	312331	56958	56135	57561	68035
971029 MRF6-12R #9 1		1727778	1104503	4019755	409117	340893	58690	59563	64190	74154
971029 MRF6-12R #10 1		2200319	1313092	5222555	498491	406659	70924	68528	77230	87709
971029 MRF6-12R Nod a-1 #4 1		2485877	497751	4760063	179462	128108	23667	24587	25640	30178
971029 MRF6-12R Nod a-1 #5 1		1478452	380025	2498970	155718	117329	20241	20277	20351	24715
971029 MRF6-12R Nod a-1 #6 1		2728440	543072	5000238	204521	164769	27481	25201	28573	33610
971029 MRF6-12R #11 1		1464057	796889	4106700	300955	247390	44381	42511	46563	54802
971029 MRF6-12R #12 1		1236740	766690	3812393	285305	240947	43028	42785	45779	54874
971029 MRF6-12R #13 1		1240509	760382	3652166	289603	218364	40510	40304	44085	50955
971029 MRF6-12R #14 1		1965336	893857	4530211	334650	264887	46544	43970	46795	59460
971029 MRF6-12R #15 1		1451718	1005117	4226495	382725	311679	55365	53613	57445	69565
971029 MRF6-12R #16 1		1688280	1130466	4066514	426630	350573	60201	57579	65527	77420
971029 MRF6-12R #17 1		2013649	1099609	5103510	433327	354438	64310	61936	66351	74772
971029 MRF6-12R #18 1		1580399	618999	3260457	242724	199307	36152	36173	37750	45717
971029 MRF6-12R #19 1		1233808	291438	1266576	129473	104323	20521	20446	20636	24117
971029 MRF6-12R #20 1		2771038	650187	3245943	248036	209004	36810	38493	38422	44334
971029 MRF6-12R nod a-1 #7 1		2620440	479668	6426822	173297	137321	23183	22583	24195	27401
971029 MRF6-12R nod a-1 #8 1		2987593	560554	6490770	196131	146970	25765	25419	29329	34572
971029 MRF6-12R nod a-1 #9 1		2395060	480014	6009205	180099	144087	24903	23574	25217	32659

Table A.1. Blank-subtracted LA ICP-MS data, low magnification mode.

blank-subtracted data (cps)		Dy	Ho	Er	Tm	Yb	Lu	Th	U
	mass	161.93	164.93	165.93	168.93	173.94	174.94	232.04	238.05
971029 MRF6-12R Nod A-1 1 1		48936	37278	39486	18662	37535	17920	138239	79696
971029 MRF6-12R Nod A-1 2 1		47838	35081	36186	17072	39336	19084	164422	70623
971029 MRF6-12R Nod A-1 3 1		54308	42157	42992	20088	41836	20390	168540	87943
971029 MRF6-12R #1 1		91854	65182	63913	29950	58151	26332	195428	80770
971029 MRF6-12R #2 1		110873	81400	77045	36348	76584	30823	322988	124846
971029 MRF6-12R #3 1		126414	94314	87597	40221	81147	37536	221632	145950
971029 MRF6-12R #4 1		107095	77181	70450	33222	69743	30489	347208	134080
971029 MRF6-12R #5 1		131131	92949	85049	40576	81967	38963	319200	143494
971029 MRF6-12R #6 1		99736	73661	68229	32137	64176	29243	270129	133618
971029 MRF6-12R #7 1		104537	79424	73020	33987	66747	30204	206263	133193
971029 MRF6-12R #8 1		109554	78459	75308	35192	74912	32551	162924	128490
971029 MRF6-12R #9 1		120474	88021	83197	39131	83206	37834	124241	135952
971029 MRF6-12R #10 1		145134	109424	102809	46796	95108	44252	169281	197958
971029 MRF6-12R Nod a-1 #4 1		50590	37541	40157	18778	45335	20638	166849	78120
971029 MRF6-12R Nod a-1 #5 1		43522	34833	34221	15539	30863	13747	86023	49743
971029 MRF6-12R Nod a-1 #6 1		55812	46246	46057	22270	42876	20460	145290	90124
971029 MRF6-12R #11 1		87254	66291	60148	30505	62327	28611	137315	127348
971029 MRF6-12R #12 1		87059	66938	64012	29034	62267	27451	200547	130012
971029 MRF6-12R #13 1		86677	61293	62771	27221	61685	27882	233284	116051
971029 MRF6-12R #14 1		105311	74956	75219	34689	70489	33683	237495	135216
971029 MRF6-12R #15 1		114819	81842	79165	37245	78777	37490	245175	130507
971029 MRF6-12R #16 1		128352	94668	87030	41559	81978	38379	244076	147449
971029 MRF6-12R #17 1		132018	95354	93892	45630	95676	41538	147975	159512
971029 MRF6-12R #18 1		76977	58971	57883	27816	56343	25779	124364	110902
971029 MRF6-12R #19 1		40150	27441	26841	12704	27945	12987	24736	42013
971029 MRF6-12R #20 1		72596	54143	52523	24643	52516	23917	110418	102231
971029 MRF6-12R nod a-1 #7 1		49718	38214	39767	19883	39276	19779	173319	89095
971029 MRF6-12R nod a-1 #8 1		58748	43507	46622	22145	48796	24401	232435	93208
971029 MRF6-12R nod a-1 #9 1		53641	43689	42748	20759	41633	19348	168127	92367

Table A.1 (continued). Blank-subtracted LA ICP-MS data, low magnification mode.

(units = cps/ppm)		Co	La	Ce	Pr	Nd	Sm	Eu	Gd	Tb	Dy	Ho	Er	Tm
	mass	59	139	140	141	146	147	151	157	159	162	165	166	169
971029 MRF6-12R Nod A-1 1 1		1061	4070	10186	8260	8694	7904	9141	5769	6858	8201	7411	7835	8522
971029 MRF6-12R Nod A-1 2 1		1232	3836	9480	7303	7122	6582	8059	5583	7026	8017	6974	7180	7795
971029 MRF6-12R Nod A-1 3 1		991	4517	8992	8598	8694	7337	9182	6254	8210	9101	8381	8530	9173
971029 MRF6-12R #1 1		1061	4116	9314	8053	8192	7276	8833	5878	7366	8434	7614	7859	8507
971029 MRF6-12R #2 1		1026	4092	9075	8053	8214	7278	8872	5887	7367	8428	7638	7869	8518
971029 MRF6-12R #3 1		992	4067	8837	8052	8236	7280	8911	5897	7368	8422	7663	7880	8528
971029 MRF6-12R #4 1		958	4042	8598	8052	8258	7282	8950	5906	7369	8416	7688	7891	8539
971029 MRF6-12R #5 1		923	4018	8359	8052	8279	7283	8989	5915	7370	8410	7713	7901	8549
971029 MRF6-12R #6 1		889	3993	8121	8051	8301	7285	9028	5924	7370	8405	7737	7912	8560
971029 MRF6-12R #7 1		855	3968	7882	8051	8323	7287	9067	5934	7371	8399	7762	7923	8571
971029 MRF6-12R #8 1		820	3944	7644	8050	8345	7289	9106	5943	7372	8393	7787	7933	8581
971029 MRF6-12R #9 1		786	3919	7405	8050	8367	7290	9145	5952	7373	8387	7811	7944	8592
971029 MRF6-12R #10 1		752	3894	7166	8050	8389	7292	9184	5961	7374	8381	7836	7955	8602
971029 MRF6-12R Nod a-1 #4 1		799	4067	8070	8030	7880	7254	9710	6159	7545	8478	7463	7968	8574
971029 MRF6-12R Nod a-1 #5 1		475	3105	4236	6967	7217	6204	8008	4889	6179	7294	6925	6790	7095
971029 MRF6-12R Nod a-1 #6 1		877	4437	8477	9151	10135	8423	9952	6864	8403	9353	9194	9138	10169
971029 MRF6-12R #11 1		730	3894	7270	8063	8445	7317	9241	6001	7422	8437	7902	8018	8699
971029 MRF6-12R #12 1		743	3919	7613	8076	8478	7340	9259	6031	7468	8499	7943	8070	8784
971029 MRF6-12R #13 1		756	3944	7955	8089	8512	7362	9277	6062	7515	8561	7984	8122	8870
971029 MRF6-12R #14 1		768	3968	8298	8103	8546	7385	9295	6092	7561	8623	8024	8175	8956
971029 MRF6-12R #15 1		781	3993	8640	8116	8580	7408	9314	6123	7607	8684	8065	8227	9042
971029 MRF6-12R #16 1		794	4017	8983	8129	8614	7431	9332	6153	7654	8746	8106	8279	9128
971029 MRF6-12R #17 1		807	4042	9325	8142	8648	7454	9350	6183	7700	8808	8147	8332	9213
971029 MRF6-12R #18 1		819	4067	9668	8156	8682	7477	9368	6214	7747	8870	8188	8384	9299
971029 MRF6-12R #19 1		832	4091	10010	8169	8715	7500	9386	6244	7793	8932	8229	8436	9385
971029 MRF6-12R #20 1		845	4116	10353	8182	8749	7523	9404	6275	7840	8994	8270	8488	9471
971029 MRF6-12R nod a-1 #7 1		843	3919	10895	7754	8447	7106	8918	5812	6850	8332	7597	7890	9079
971029 MRF6-12R nod a-1 #8 1		961	4580	11004	8775	9040	7897	10038	7045	8643	9845	8649	9250	10112
971029 MRF6-12R nod a-1 #9 1		770	3922	10187	8058	8863	7633	9310	6058	8165	8990	8686	8482	9479

Table A.2. LA ICP-MS interpolated instrumental response correction.

(units = cps/ppm)		Yb	Lu	Th	U
	mass	174	175	232	238
971029 MRF6-12R Nod A-1 1 1		8283	8774	5120	13380
971029 MRF6-12R Nod A-1 2 1		8681	9344	6090	11856
971029 MRF6-12R Nod A-1 3 1		9232	9984	6242	14764
971029 MRF6-12R #1 1		8734	9330	5735	13230
971029 MRF6-12R #2 1		8737	9292	5653	13127
971029 MRF6-12R #3 1		8739	9254	5571	13024
971029 MRF6-12R #4 1		8742	9216	5489	12921
971029 MRF6-12R #5 1		8744	9178	5407	12818
971029 MRF6-12R #6 1		8747	9140	5325	12715
971029 MRF6-12R #7 1		8749	9103	5243	12611
971029 MRF6-12R #8 1		8752	9065	5162	12508
971029 MRF6-12R #9 1		8754	9027	5080	12405
971029 MRF6-12R #10 1		8756	8989	4998	12302
971029 MRF6-12R Nod a-1 #4 1		10004	10105	6180	13115
971029 MRF6-12R Nod a-1 #5 1		6811	6731	3186	8351
971029 MRF6-12R Nod a-1 #6 1		9462	10018	5381	15130
971029 MRF6-12R #11 1		8830	9080	5113	12487
971029 MRF6-12R #12 1		8901	9209	5310	12776
971029 MRF6-12R #13 1		8972	9338	5507	13064
971029 MRF6-12R #14 1		9043	9467	5704	13352
971029 MRF6-12R #15 1		9114	9596	5902	13641
971029 MRF6-12R #16 1		9185	9724	6099	13929
971029 MRF6-12R #17 1		9257	9853	6296	14217
971029 MRF6-12R #18 1		9328	9982	6493	14506
971029 MRF6-12R #19 1		9399	10111	6691	14794
971029 MRF6-12R #20 1		9470	10240	6888	15083
971029 MRF6-12R nod a-1 #7 1		8667	9685	6419	14958
971029 MRF6-12R nod a-1 #8 1		10768	11947	8609	15648
971029 MRF6-12R nod a-1 #9 1		9187	9473	6227	15507

Table A.2 (continued). LA ICP-MS interpolated instrumental response correction.

CONCENTRATION DATA (ppm)		Co	La	Ce	Pr	Nd	Sm	Eu	Gd	Tb	Dy	Ho
	mass	59	139	140	141	146	147	151	157	159	162	165
	%abund.	100.00	99.91	88.48	100.00	17.19	15.00	47.80	15.65	100.00	25.50	100.00
971029 MRF6-12R Nod A-1 1 1		3110	123	667	22	95	22	5	27	4	23	5
971029 MRF6-12R Nod A-1 2 1		3110	123	667	22	95	22	5	27	4	23	5
971029 MRF6-12R Nod A-1 3 1		3110	123	667	22	95	22	5	27	4	23	5
971029 MRF6-12R #1 1		1274	206	472	40	184	43	11	51	7	43	9
971029 MRF6-12R #2 1		1667	240	664	50	230	54	14	65	10	52	11
971029 MRF6-12R #3 1		1610	269	710	55	267	57	15	73	10	59	12
971029 MRF6-12R #4 1		2019	243	640	49	223	51	13	65	9	50	10
971029 MRF6-12R #5 1		2067	305	634	59	268	60	14	76	11	61	12
971029 MRF6-12R #6 1		1782	234	671	46	209	47	11	59	9	47	10
971029 MRF6-12R #7 1		1776	245	626	47	217	49	12	59	9	49	10
971029 MRF6-12R #8 1		1908	263	624	48	218	52	13	62	9	51	10
971029 MRF6-12R #9 1		2198	282	614	51	237	54	14	69	10	56	11
971029 MRF6-12R #10 1		2927	337	824	62	282	65	16	83	12	68	14
971029 MRF6-12R Nod a-1 #4 1		3110	123	667	22	95	22	5	27	4	23	5
971029 MRF6-12R Nod a-1 #5 1		3110	123	667	22	95	22	5	27	4	23	5
971029 MRF6-12R Nod a-1 #6 1		3110	123	667	22	95	22	5	27	4	23	5
971029 MRF6-12R #11 1		2005	205	638	37	170	40	10	50	7	41	8
971029 MRF6-12R #12 1		1665	196	566	35	165	39	10	48	7	40	8
971029 MRF6-12R #13 1		1642	193	519	36	149	37	9	46	7	40	8
971029 MRF6-12R #14 1		2558	225	617	41	180	42	10	49	8	48	9
971029 MRF6-12R #15 1		1858	252	553	47	211	50	12	60	9	52	10
971029 MRF6-12R #16 1		2126	282	512	52	237	54	13	68	10	58	12
971029 MRF6-12R #17 1		2496	272	619	53	238	58	14	69	10	59	12
971029 MRF6-12R #18 1		1929	152	381	30	134	32	8	39	6	34	7
971029 MRF6-12R #19 1		1483	71	143	16	70	18	5	21	3	18	3
971029 MRF6-12R #20 1		3279	158	354	30	139	33	9	39	6	32	7
971029 MRF6-12R nod a-1 #7 1		3110	123	667	22	95	22	5	27	4	23	5
971029 MRF6-12R nod a-1 #8 1		3110	123	667	22	95	22	5	27	4	23	5
971029 MRF6-12R nod a-1 #9 1		3110	123	667	22	95	22	5	27	4	23	5

Table A.3. LA ICP-MS concentration calculations.

CONCENTRATION DATA (ppm)		Er	Tm	Yb	Lu	Th	U
	mass	166	169	174	175	232	238
	%abund.	33.60	100.00	31.80	97.41	100.00	99.27
971029 MRF6-12R Nod A-1 1 1		15	2	14	2	27	6
971029 MRF6-12R Nod A-1 2 1		15	2	14	2	27	6
971029 MRF6-12R Nod A-1 3 1		15	2	14	2	27	6
971029 MRF6-12R #1 1		24	4	21	3	34	6
971029 MRF6-12R #2 1		29	4	28	3	57	10
971029 MRF6-12R #3 1		33	5	29	4	40	11
971029 MRF6-12R #4 1		27	4	25	3	63	10
971029 MRF6-12R #5 1		32	5	29	4	59	11
971029 MRF6-12R #6 1		26	4	23	3	51	11
971029 MRF6-12R #7 1		27	4	24	3	39	11
971029 MRF6-12R #8 1		28	4	27	4	32	10
971029 MRF6-12R #9 1		31	5	30	4	24	11
971029 MRF6-12R #10 1		38	5	34	5	34	16
971029 MRF6-12R Nod a-1 #4 1		15	2	14	2	27	6
971029 MRF6-12R Nod a-1 #5 1		15	2	14	2	27	6
971029 MRF6-12R Nod a-1 #6 1		15	2	14	2	27	6
971029 MRF6-12R #11 1		22	4	22	3	27	10
971029 MRF6-12R #12 1		24	3	22	3	38	10
971029 MRF6-12R #13 1		23	3	22	3	42	9
971029 MRF6-12R #14 1		27	4	25	4	42	10
971029 MRF6-12R #15 1		29	4	27	4	42	10
971029 MRF6-12R #16 1		31	5	28	4	40	11
971029 MRF6-12R #17 1		34	5	33	4	24	11
971029 MRF6-12R #18 1		21	3	19	3	19	8
971029 MRF6-12R #19 1		9	1	9	1	4	3
971029 MRF6-12R #20 1		18	3	17	2	16	7
971029 MRF6-12R nod a-1 #7 1		15	2	14	2	27	6
971029 MRF6-12R nod a-1 #8 1		15	2	14	2	27	6
971029 MRF6-12R nod a-1 #9 1		15	2	14	2	27	6

Table A.3 (continued). LA ICP-MS concentration calculations.

Appendix B. Inter-elemental correlation coefficients

Inter-elemental correlation coefficients were calculated for LA ICP-MS, ICP-AES, and EPMA data using the least squares method. Sample size (n) is listed on each table.

ICP-AES (n=32, R values)							
	Ce	Ni	Fe	Mn	Zn	Cu	Co
Al	0.704	0.616	0.805	0.670	0.263	0.575	0.806
Ce		-0.597	0.875	-0.479	-0.740	-0.635	0.899
Ni			-0.535	0.963	0.926	0.983	-0.507
Fe				-0.348	-0.713	-0.580	0.971
Mn					0.944	0.973	-0.266
Zn						0.957	-0.691
Cu							-0.528

Table B.1. Inter-elemental correlation coefficients for nodule MRF1-20R. ICP-AES data.

hi mag LAICPMS (n= 184, R values)														
	Ti	V	Fe	Co	Ni	Cu	Zn	As	Mo	La	Ce	Pb	Th	U
P	0.786	0.691	0.766	0.709	-0.607	-0.628	-0.611	0.837	-0.484	0.841	0.748	0.818	0.684	0.801
Ti		0.907	0.932	0.958	-0.539	-0.640	-0.766	0.954	0.207	0.973	0.980	0.982	0.851	0.952
V			0.865	0.886	0.367	0.226	-0.479	0.875	0.716	0.868	0.867	0.879	0.720	0.901
Fe				0.860	-0.575	-0.655	-0.749	0.936	0.141	0.941	0.923	0.920	0.825	0.896
Co					-0.472	-0.597	-0.777	0.904	0.321	0.898	0.938	0.935	0.748	0.894
Ni						0.963	0.711	-0.643	0.849	-0.619	-0.532	-0.566	-0.561	-0.530
Cu							0.872	-0.669	0.875	-0.701	-0.650	-0.649	-0.650	-0.546
Zn								-0.709	0.746	-0.777	-0.802	-0.769	-0.725	-0.620
As									0.134	0.963	0.921	0.951	0.775	0.963
Mo										-0.274	-0.200	-0.158	-0.500	0.307
La											0.959	0.964	0.873	0.960
Ce												0.972	0.907	0.920
Pb													0.834	0.947
Th														0.815

Table B.2. Inter-elemental correlation matrix for MRF1-20R. High magnification LA ICP-MS data.

ICP-AES (n=11, R values)							
	Ce	Ni	Fe	Mn	Zn	Cu	Co
Al	-0.214	0.182	-0.691	-0.550	-0.686	0.363	-0.628
Ce		0.612	0.804	-0.167	0.361	-0.480	0.891
Ni			0.724	0.489	0.888	0.668	0.764
Fe				0.247	0.823	0.292	0.891
Mn					0.733	0.708	0.279
Zn						0.710	0.722
Cu							-0.514
EPMA (n=257)							
	Fe	Ti	Al				
Mn	0.329	0.378	0.588				
Fe		0.872	0.624				
Ti			0.650				

Table B.3. Inter-elemental correlation matrices for MRF2-3R, ICP-AES and EPMA data.

hi mag LAICPMS (n= 678, R values)																	
	Ti	V	Fe	Co	Ni	Cu	Zn	Mo	La	Ce	Pr	Nd	Lu	W	Pb	Th	U
P	0.877	0.854	0.891	0.561	0.409	0.344	0.386	0.633	0.866	0.844	0.871	0.861	0.696	0.358	0.863	0.746	0.829
Ti		0.893	0.912	0.681	0.118	0.449	0.464	0.725	0.889	0.873	0.897	0.892	0.743	0.453	0.856	0.838	0.840
V			0.947	0.476	0.367	0.442	0.669	0.780	0.837	0.827	0.851	0.840	0.728	0.653	0.869	0.637	0.876
Fe				0.470	-0.251	0.190	0.486	0.638	0.864	0.845	0.870	0.873	0.728	0.423	0.887	0.705	0.876
Co					0.473	0.723	0.382	0.663	0.632	0.643	0.669	0.645	0.533	0.335	0.475	0.811	0.434
Ni						0.871	0.879	0.681	-0.456	-0.493	-0.405	-0.443	-0.348	0.820	-0.285	-0.313	-0.263
Cu							0.762	0.670	-0.303	-0.361	-0.141	-0.253	-0.230	0.695	-0.122	0.440	-0.202
Zn								0.792	0.341	0.307	0.373	0.322	0.330	0.883	0.540	-0.071	0.486
Mo									0.727	0.712	0.725	0.705	0.625	0.813	0.753	0.589	0.691
La										0.970	0.978	0.975	0.815	0.437	0.906	0.822	0.855
Ce											0.954	0.954	0.797	0.399	0.899	0.818	0.823
Pr												0.967	0.808	0.446	0.884	0.838	0.845
Nd													0.806	0.405	0.878	0.833	0.843
Lu														0.392	0.727	0.675	0.722
W															0.536	-0.089	0.499
Pb																0.692	0.842
Th																	0.650

Table B.4. Inter-elemental correlation matrix for MRF2-3R, high magnification LA ICP-MS data.

ICP-AES (n=9, R values)						
	Ni	Fe	Mn	Zn	Cu	Co
Al	0.686	0.666	0.567	0.679	0.716	-0.607
Ni		-0.926	0.962	0.994	0.958	-0.437
Fe			-0.792	-0.917	-0.927	0.766
Mn				0.962	0.867	0.394
Zn					0.925	-0.387
Cu						-0.616

Table B.5. Inter-elemental correlation matrix for MRF6-12R, ICP-AES data.

hi mag LAICPMS (n= 363, R values)																	
	Ti	V	Fe	Co	Ni	Cu	Zn	Mo	La	Ce	Pr	Nd	Lu	W	Pb	Th	U
P	0.764	0.806	0.817	0.700	0.354	-0.295	0.214	0.587	0.817	0.812	0.846	0.837	0.811	0.476	0.737	0.785	0.825
Ti		0.846	0.908	0.908	-0.247	0.126	0.358	0.692	0.929	0.932	0.910	0.919	0.887	0.610	0.901	0.712	0.792
V			0.837	0.885	0.541	0.574	0.677	0.867	0.841	0.893	0.871	0.878	0.888	0.825	0.796	0.752	0.917
Fe				0.742	-0.436	-0.311	0.197	0.631	0.909	0.906	0.901	0.905	0.873	0.501	0.915	0.712	0.802
Co					0.647	0.702	0.719	0.888	0.802	0.861	0.800	0.815	0.814	0.884	0.760	0.653	0.796
Ni						0.977	0.965	0.738	-0.462	0.161	-0.437	-0.411	-0.305	0.879	-0.324	-0.412	0.114
Cu							0.978	0.745	-0.352	0.195	-0.342	-0.307	-0.221	0.897	0.164	0.437	0.158
Zn								0.786	-0.138	0.378	0.045	0.718	0.753	0.863	0.798	0.544	0.747
Mo									0.686	0.778	0.794	0.711	0.754	0.930	0.682	0.506	0.756
La										0.936	0.986	0.987	0.947	0.576	0.893	0.790	0.849
Ce											0.933	0.939	0.909	0.661	0.887	0.817	0.869
Pr												0.989	0.954	0.812	0.856	0.811	0.891
Nd													0.957	0.604	0.873	0.812	0.892
Lu														0.640	0.837	0.801	0.904
W															0.579	0.370	0.665
Pb																0.556	0.711
Th																	0.835

Table B.6. Inter-elemental correlation matrix for MRF6-12R, high magnificationn LA ICP-MS data.